UNIVERSITY OF SOUTHAMPTON

A Theoretical Study of Relativistic Jets and Accretion Processes

Omar Jamil
Submitted for the degree of Doctor of Philosophy
SCHOOL OF PHYSICS AND ASTRONOMY
SCHOOL OF ENGINEERING SCIENCE
FACULTY OF ENGINEERING, SCIENCE AND MATHEMATICS

February 23, 2010

UNIVERSITY OF SOUTHAMPTON

ABSTRACT

FACULTY OF ENGINEERING, SCIENCE AND MATHEMATICS

SCHOOL OF PHYSICS AND ASTRONOMY
SCHOOL OF ENGINEERING SCIENCE

Doctor of Philosophy

A Theoretical Study of Relativistic Jets and Accretion Processes

by Omar Jamil

The following work explores different aspects of the disc:jet connection in X-ray binaries. There is a detailed description of a new jet model (*i*Shocks) that is used, firstly, to address the re-energization problem in the conical jet geometries. The adiabatic energy losses suffered by conical jets are successfully countered to reproduce the canonical flat/inverted synchrotron spectrum associated with compact radio jets.

The *i*Shocks model uses discrete packets of plasma, or shells, to simulate a jet. The shell collisions give rise to the shocks that are used to re-energize the emitting electrons. Multiple internal shocks, all along the jet, are shown to be necessary to achieve sufficient re-acceleration. The flat/inverted spectrum (ranging from the infra-red to the radio) is successfully reproduced and the high frequency break for such a spectrum is shown to be correlated with the jet power: $\nu_b \sim L_W^{0.6}$. While the flat-spectrum synchrotron flux is also correlated with the jet power via: $F_\nu \sim L_W^{1.4}$. Both these correlations are in agreement with the previous analytical predictions.

The model is also used to explore the massive ejections scenario in the source GRS 1915+105. Various *i*Shocks set-ups are used to model the data that display the flaring behaviour observed in different frequencies (IR-mm-radio).

The X-ray binary timing properties are also investigated with the aide of the *i*Shocks model. In particular, the optical/X-ray correlations are the focus of the present study. These correlations have been observed to show some interesting behaviours, such as: the optical lagging the X-rays, and the optical emission showing awareness of the X-ray emission in the form of pre-cognition dips. A number of these correlations are successfully reproduced by translating the simulated X-ray light curves into the jet parameters used as the input for the *i*Shocks model.

In addition to relativistic jets, a study of the electron-positron pair processes is also included in the present work. The electron-positron pair annihilation is implemented in an existing Comptonization code (simulating the corona) to explore the possibility of masking an annihilation line from the X-ray binary sources. The results show that radiative processes such as inverse Compton scattering and bremsstrahlung radiation, in addition to thermal line broadening, can be very effective in making the e^-/e^+ annihilation line indistinguishable from the rest of the high energy spectrum.

DECLARATION

I, Omar Jamil, hereby declare that the thesis entitled *A Theoretical Study of Relativistic Jets and Accretion Processes* and the work presented in the thesis are both my own, and have been generated by me as the result of my own original research. I confirm that:

- this work was done wholly or mainly while in candidature for a research degree at this University;
- where any part of this thesis has previously been submitted for a degree or any other qualification at this University or any other institution, this has been clearly stated;
- where I have consulted the published work of others, this is always clearly attributed;
- where I have quoted from the work of others, the source is always given. With the exception of such quotations, this thesis is entirely my own work;
- I have acknowledged all main sources of help;
- where the thesis is based on work done by myself jointly with others, I have made clear exactly what was done by others and what I have contributed myself;
- parts of this work have been published as:

  Jamil, O., Fender, R., Kaiser, C., *iShocks: X-ray binary jets with an internal shocks model*, Mon. Not. R. Astron. Soc., 2009 in press.

  Jamil, O., Fender, R., Kaiser, C., *Internal shocks model for Microquasar Jets*, Proceedings of the VII Microquasar Workshop: Microquasars and Beyond. September 1-5, 2008, Foca, Izmir, Turkey., p.26

  Jamil, O., Rogers, K., Kaiser, C., Collins, R., *Modelling Electron/Positron distributions in the HEART code*, Proceedings of the VI Microquasar Workshop: Microquasars and Beyond. September 18-22, 2006, Como, Italy., p.79.1.

  Rogers, K., Jamil, O., Kaiser, C., Collins, R., *The HEART (High Energy Astrophysical Radiative Transfer) code: modelling X-ray binaries and AGN*, Proceedings of the VI Microquasar Workshop: Microquasars and Beyond. September 18-22, 2006, Como, Italy., p.91.1.

Signed: _____

Date: _____

ACKNOWLEDGEMENTS

At last, I am here. Writing the acknowledgements; this must mean I have finished writing up. However, I would not have reached this stage without the help and the support of the following people.

The first and foremost I would like to thank Rob Fender, my supervisor. I am extremely grateful to him for adopting this phd-orphan and giving him a good home! Rob's enthusiasm, knowledge, and insight have taught me more than I can list here. I owe him much.

I would also like to thank Christian Kaiser for giving me this opportunity in the first place and teaching me the way of the theorist. A special thank you also goes to Phil Uttley for the time and the effort he has put into developing various aspects of this work. A thank you to Tony Bird for taking the time to read one of the chapters and providing very insightful comments. I am also very grateful to Tom Maccarone for knowing everything about everything! I have learnt a lot from discussing an array of topics with Tom, in addition to getting a better handle on the American culture: whether it is the finer points of ice hockey or the joys of American cuisine.

I've made many friends whilst doing my time here. A big thank you to: Chris and Dan for a providing me great many distractions; Clément (a.k.a.the Frenchman) for the discussions and shaving a few years off my life by introducing me to Tartiflette and Raclette; Katrine Rogers for the support and friendship; Simone Scaringi for always being happy to take money off me under the guise of a poker game. Thanks to the sociable nature of the people here it is difficult to mention everyone, but just to name a few of the members, past and present (with the nicknames that I can remember, or made up): Tony "Rocky" Wilkinson (thanks for sharing some great tracks), Mark "with a surname like that..." Peacock, Sebastian "boris" Jester, Ed Pope, Elmar "mo" Körding, Retha "marge" Pretorius, Dave "nad" Russell, Elmé Breedt, Vannessa "nessie" McBride, Vito "the don" Sguera, and my very friendly office-mates. Plus, a thank you to Tom Frost and Cara Neal (fellow ex-members of the *Lane*) for the tea breaks, the enlightening conversations, and the kittens.

I would also like to mention a couple of friends outside of the astronomy mafia. Sudan: we started at the same time and it seems we shall finish at the same time too. I'm glad we could share the stories and experiences, even though you made that little mistake of doing particle physics. And Stu: following in the footsteps of Einstein; first the physics degree, then the patent office and now the research in mud.

I must also mention my family. I feel blessed to have parents like mine. I can never repay their hard work and sacrifices to give me the opportunities they never had. My eternal love and gratitude goes out to them. Also, Faisal and Aamir: not just my brothers, but my friends.

Finally, I would like to thank Lisa. You have opened my eyes to more things than I could have imagined and have always been there for me. I look forward to continuing this journey with you.

Omar – October 2009

All my life I've had one dream, to achieve my many goals.

HOMER J. SIMPSON

For my parents

CONTENTS

LIST OF TABLES

LIST OF FIGURES

Nature is a temple in which living columns sometimes emit confused words. Man approaches it through forests of symbols, which observe him with familiar glances.

CHARLES BAUDELAIRE (1821 – 1867)

They who dream by day are cognizant of many things which escape those who dream only by night.

EDGAR ALLAN POE (1809 – 1849)

It is not titles that honor men, but men that honor titles.

NICCOLÒ MACHIAVELLI (1469 – 1527)

1 Introduction

The following chapter describes some of the key features that provide the background for the relativistic jets model and the electron-positron pair processes work presented later. These two topics on first sight may appear to be distinct in many respects, but they are simply an endeavour in gaining a better overall understanding of the astronomical systems such as the X-ray binaries and the active galactic nuclei.

1.1 Compact objects

The following work, plus a major part of the field of astrophysics in general, is interested in what are referred to as the *compact objects*. This is a general term that encompasses quite different astronomical objects: White Dwarfs, Neutron Stars, and Black Holes. These are the densest [1] objects in the universe and their interaction with other objects/matter (in addition to studying the object itself) are some of the most active areas of research today. The compact object's interaction with other matter, through accretion, can release a considerable fraction of the matter's rest mass energy (discussed later). This energy release, when in the form of radiation, can make these systems very bright in a variety of wavelengths. Therefore studying these systems is an indirect way to the compact objects.

These compact objects can also exist in stable binary configurations. If the second object in a binary system is a star, and depending on the geometry of the system, the compact object can accrete matter from the star. The X-ray binaries, described below, are a subset of this group of

[1] here, the traditional concept of density is applied to the white dwarfs and the neutron stars only. The black hole density is more arbitrary: this can either be volume-averaged density of the event horizon, or the hitherto unknown density of a singularity.

objects and the main focus of the present study. The primary aim here is to better understand the X-ray binary systems that are harbouring a black hole.

1.1.1 Black Holes

The gravitational force is constantly acting to collapse any massive body onto itself, making it denser in the process. In most objects the gravitational force is opposed by some other physical mechanism, be it the thermal pressure or the particle degeneracy. However, if a star is sufficiently massive (and dense), its gravity can overcome all the other forces, and collapse it to a singularity — a black hole (BH) is born. Although very exotic, black holes are quite simple objects and can be described entirely by their masses, spins and charges. Any charge that might build up would be neutralized by the accretion of oppositely charged matter, leaving us with just the mass and the spin to describe any astrophysical black hole.

The singularity, presumed to lie at the heart of a black hole, is concealed by the *event horizon*. Once past the event horizon, nothing can escape. That is, no information can be passed from inside the event horizon to the outside universe. There is an innermost stable circular orbit (ISCO) outside of the black hole where matter, if it has angular momentum, can remain free of the black hole's pull; beyond this point the matter will plunge towards the BH. This concept can be better understood by looking at the motion a body in a strong gravitational field [2]:

$$\frac{1}{c^2}\left(\frac{\mathrm{dr}}{\mathrm{ds}}\right)^2 + V^2(r) = E^2 \,, \tag{1.1}$$

where s is the proper time and is related to the co-ordinate time t via:

$$\frac{\mathrm{d}t}{\mathrm{d}s} = E(1-2GM/rc^2)^{-1} \,. \tag{1.2}$$

The effective potential is given by:

$$V^2(r) = (1-2GM/rc^2)(1+h^2/c^2r^2) \,, \tag{1.3}$$

where r denotes the radial position of the particle in orbit around a mass M and h is the relativistic angular momentum per unit mass of the orbiting particle. We can see that as

$$r \to \frac{2GM}{c^2} \,, \tag{1.4}$$

equations 1.1 and 1.3 start to break down. The radius given in equation 1.4 is where the event horizon lies and is referred to as the Schwarzschild radius r_S (or two gravitational radii $2r_g$). As noted earlier, circular orbits ($\mathrm{d}r/\mathrm{d}s = 0$) are possible: these occur at radii such that $\partial V/\partial r = 0$. The stable circular orbits are therefore possible at:

$$r = \frac{GM}{2c^2}\left[H^2 + (H^4 - 12H^2)^{\frac{1}{2}}\right] \,, \tag{1.5}$$

[2] a gravitaional field is considered strong if $GM/rc^2 \sim 1$, implying $GMm/r \sim mc^2$ for a body of mass m.

where $H = c^2h/GM$, if $h \geq 2(3)^{1/2}GM/c^2$ (Frank *et al.*, 2002)[3]. It should be noted that even if the matter has finite angular momentum, it would still fall-in once past the minimum of all the possible circular orbits (ISCO); for a non-spinning black hole (*Schwarzschild* BH) this is given by $3r_S$, whilst for a prograde orbit around a maximally rotating black hole this (and the event horizon) are reduced to $0.5r_S$. The innermost stable orbit therefore represents the point of maximum feasible energy extraction.

The matter is able stay in orbit around a black hole, as long as it possesses sufficient angular momentum ($h \geq 2(3)^{1/2}GM/c^2$). Accumulation of matter in various orbits around an accreting object is the basis of an accretion disc; angular momentum is transported outwards in an accretion disc (due to viscous interactions), causing the matter to occupy progressively lower orbits until it reaches the ISCO. During this process of in-fall and viscous interactions, gravitational potential energy is extracted, and converted into kinetic and thermal energy. The position of the last stable orbit also has an impact on the amount of energy liberated from the in-falling matter. The smaller the ISCO (for example spinning black hole), the higher is the energy liberated. By the time matter reaches ISCO, a significant proportion of its binding energy can be radiated away: $0.057mc^2$ if around a Schwarzschild black hole, and $0.42mc^2$ if in a prograde orbit around a maximally spinning black hole.

1.2 X-ray binaries

An X-ray binary (XRB) system comprises a donor star and an accreting compact object. As the matter is accreted onto the compact object, X-rays are emitted. The emission properties of these systems are determined by various factors, such as: the nature of the compact object i.e. a black hole or a neutron star, the accretion flow mechanism, and the magnetic field strength (in the case of neutron stars). Accreting white dwarfs form a class of objects known as the *cataclysmic variables*.

If the donor star in an X-ray binary system is low-mass ($\lesssim$1 $M_\odot$) then the system is referred to as a Low Mass X-ray Binary (LMXB). On the other hand, if the donor star is high-mass ($\gtrsim$10 $M_\odot$), then the system is classified as a High Mass X-ray Binary (HMXB). As one might expect, there is another class that encompasses the intermediate masses ($\lesssim$10 $M_\odot$ and $\gtrsim$1 $M_\odot$): the Intermediate Mass X-ray Binary (IMXB). Apart from the mass of the donor star, these systems can also differ in the way the compact object accretes. Generally, in LMXBs the low mass donor star fills the Roche Lobe (figure 1.1) and the main mode of accretion is via the accretion disc. Also if the low mass donor star is main sequence or sub-giant star then it has a weak stellar wind. The donor stars in the HMXBs have strong stellar winds and do not fill their Roche Lobes (there are some exceptions: HMXBs with small orbital periods show evidence of Roche lobe overflow, for example, SMC X-1 and Cen X-3). The strong stellar winds mean that the HMXBs compact objects can have high accretion rates. The angular momentum carried in the wind results in an accretion disc forming around the compact object, unless the matter is

[3]this the minimum angular momentum required to stay in orbit greater than the innermost stable circular orbit

captured by other means (e.g. strong magnetic fields). The accretion disc also forms in LMXB systems; figure 1.2 shows an impression of such a system. In fact, it is these very discs that give rise to the X-ray emission that has defined these systems in the first place.

The different accretion mechanisms also have an impact on the observed population of X-ray binaries: most of the X-ray binaries are either HMXBs or LMXBs, with very few being IMXBs. The donor star in the IMXBs is not massive enough to generate strong stellar winds for creating a strong X-ray source. The IMXB systems can evolve and go through a Roche lobe overflow stage. However, this stage can be very short for the IMXBs. Therefore there is a natural selection effect against the IMXB detection.

The nature of the compact object can further categorize the X-ray binaries. The X-ray spectral properties of systems with black holes can also be found in neutron star systems e.g. soft spectra, fast variability, high-energy power-law spectrum, which can make distinguishing the neutron stars from the black holes quite difficult. An X-ray binary system is generally considered to be a BHC if the compact object exhibits mass greater than $3M_{\odot}$; no stable neutron stars are believed to exist with $M > 3M_{\odot}$. The neutron star systems can also offer distinguishing features: these include the presence of coherent pulsations (pulsars), and type I X-ray bursts (thermonuclear ignition on the surface of the neutron star). There are numerous other more subtle effects that are present in the X-ray spectra that can also help distinguish different types of LMXBs (see Lewin *et al.*, 1997 for many detailed reviews)

The following work focuses mainly on the LMXB sources harbouring black hole candidates. The artist's impression seen in figure 1.2 encapsulates the believed geometry of such systems: the Roche lobe filling donor star providing matter to the accreting black hole via an accretion disc, with an intermittent relativistic jet (discussed later). The picture, however, does not show the "corona", because there is still a lot of contention as to the true nature and geometry of this region (discussed later and in chapter 5).

1.2.1 Accretion and Ejection

Both the accretion and the ejection from the X-ray binaries (or AGN) can take a variety of forms. The presence of an accretion disc and a relativistic jet is a well established picture for an accreting compact object.

A large body of theoretical work exists on the nature of accretion discs. The simplest treatment of an accretion disc assumes the disc converts the gravitational potential energy into kinetic and thermal energy via the viscous stresses. Also, it is geometrically thin, but optically thick (many other variations on the geometry exist, however). The viscous dissipation rate per unit disc face area of such a disc is given by (Frank *et al.*, 2002):

$$D(r) = \frac{3GM\dot{M}}{8\pi r^3}\left[1 - \left(\frac{r_S}{r}\right)^{1/2}\right] . \tag{1.6}$$

Using this relation, we can also work out the disc luminosity between radii r_1 and r_2. This is

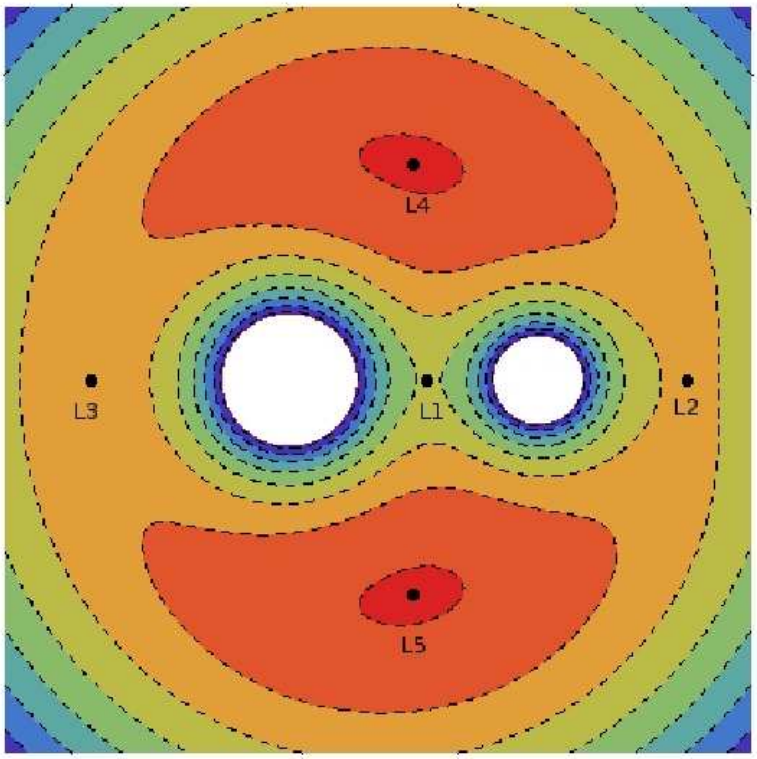

Figure 1.1: An illustration of the Lagrangian, designated with 'L', points (where various forces are in balance) in a binary system. The equipotential curves that meet at the L1 point encapsulate the *Roche Lobes*.

given by:

$$L(r_1,r_2) = \frac{3GM\dot{M}}{2}\left\{\frac{1}{r_1}\left[1-\frac{2}{3}\left(\frac{r_S}{r_1}\right)^{1/2}\right]-\frac{1}{r_2}\left[1-\frac{2}{3}\left(\frac{r_S}{r_2}\right)^{1/2}\right]\right\}, \tag{1.7}$$

and when $r_1 = r_s$ and $r_2 \to \infty$, we obtain the total disc luminosity:

$$L_{disc} = \frac{GM\dot{M}}{2r_S} = \frac{1}{2}L_{accretion}\ . \tag{1.8}$$

The disc temperature can also be calculated by combining the dissipation rate relation given in 1.6 with the black-body flux:

$$\sigma T^4 = D(r)\ , \tag{1.9}$$

where σ is the Stefan-Boltzmann constant. Using the $r_s = 2GM/c^2$ relation and assuming $r >> r_S$, the temperature of the disc can be expresses as:

$$T(r) = \left[\frac{3c^6}{64\pi\sigma G^2}\right]^{\frac{1}{4}} \dot{M}^{\frac{1}{4}} M^{-\frac{1}{2}} \left(\frac{r}{r_S}\right)^{-\frac{3}{4}}\ . \tag{1.10}$$

This is an important relation as it shows how the accretion rate, as well as the black hole mass,

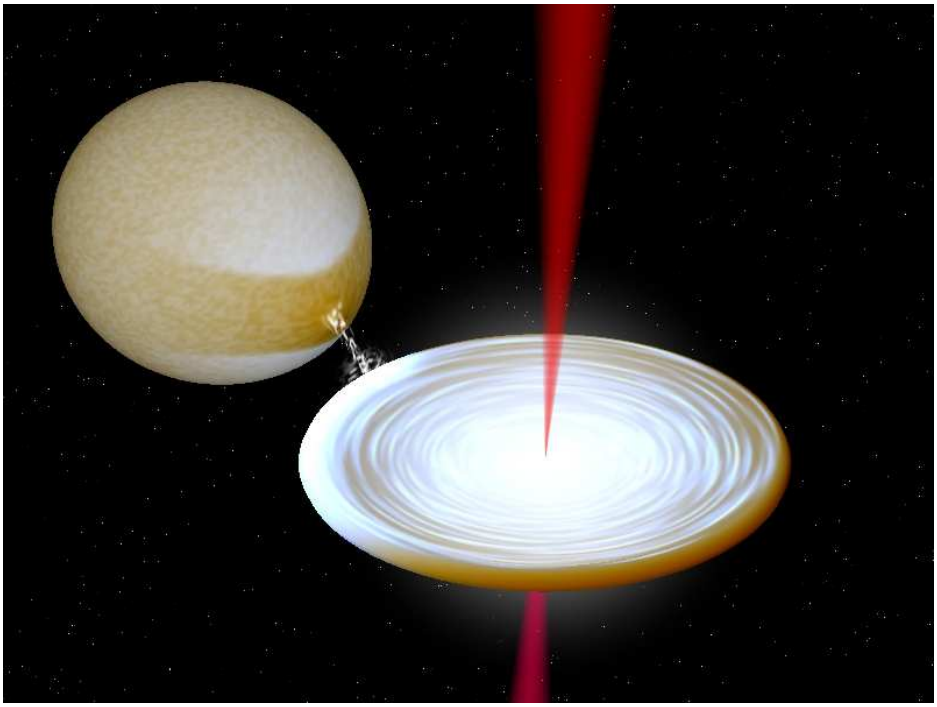

Figure 1.2: An impression of a Low Mass X-ray Binary system (LMXB). The donor star fills the Roche Lobe and feeds the compact the object via an accretion disc. The jets emanating from the compact object region are also shown. The image was generated using the BinSims software by Hynes (2002).

affect the disc temperature. It also shows how an accretion disc around a super-massive black hole is cooler than one around a stellar-mass black hole. That is, the dissipation per unit area for stellar mass black hole is higher than that of a super-massive black hole.

Although the viscous stress is at the heart of the energy dissipation in an accretion disc, its exact nature is still not fully understood. However, Magnetic Rotational Instability (MRI), which couples differentially rotating disc components, has proved a good candidate for the origin of the viscous stress (Balbus and Hawley, 1991; Hawley and Balbus, 1991; Balbus and Hawley, 1998).

The Shakura and Sunyaev (1973) solution for an accretion disc in a black hole binary system remains one of the most successful and used disc models. The Shakura-Sunyaev disc is generally modelled as a geometrically thin disc that converts the gravitational potential energy into heat via the viscous stresses. They characterize the efficiency of the transfer of angular momentum outwards (by the viscous stresses), through what is referred to as the α-parameter. More recent observational and theoretical works have shown that the accretion discs cannot be the idealized picture of the Shakura-Sunyaev disc. A number of groups are carrying out the general relativistic magneto-hydrodynamical (GRMHD) simulations to obtain a better physical understanding of the accretion discs (see Frank *et al.*, 2002 for a detailed physical analysis of the accretion processes). Not only are the accretion discs are better modelled now, but also their relationship with the ejection processes is becoming increasingly clearer.

The ejections or the outflows from the black hole systems can take a variety of forms (e.g. winds), with relativistic jets as one of the most energetic of these outflows. The jets from AGN sources have been observed since the beginning of the 20^{th} century (Curtis, 1918). The later radio observations showed that the spectra of such sources could be fitted with optically thin synchrotron spectrum. Such a spectrum has a power-law form ($S_\nu \propto \nu^{-\alpha}$, where α is the spectral index) and can be used to calculate the power-law (p)index of the underlying electron energy distribution that would give rise to such a spectrum: $\alpha = (p-1)/2$. Various other radio observations also gave rise to the label of *compact radio* sources and the associated flat/inverted spectrum was subsequently explained with the aid of a synchrotron jet model (Blandford and Königl, 1979).

Even with a long standing understanding of the relationship between accretion and ejection (jets), it was only relatively recently that the systematic studies on this connection have been carried out. The *disc:jet* connection, as it is now commonly called, appears to be getting stronger with every new endeavour in this field. In many ways this systematic study has been kick started by a better understanding of the X-ray binary jets. The discovery of jets in the X-ray binary sources SS 433 (Fabian and Rees, 1979) and Cygnus X-3 (Geldzahler *et al.*, 1983), and the apparent super-luminal motions in the outflows from the source GRS1915+105 (Mirabel and Rodríguez, 1994; Fender *et al.*, 1999), showed that highly relativistic jets emanate from the black hole X-ray binaries — similarly to the AGN jets; many more examples exist now of the jets from the BHXBs. As for the disc:jet connection, it is further strengthened by the BHXB spectral spectral states studies (see section 1.2.2) and the scaling relations encompassing the stellar-mass and the super-massive black holes (see section 1.3).

Although jets are ubiquitous in accreting sources, their launch and formation mechanisms have not been fully understood. The Blandford and Payne (1982) model is one of the earliest to suggest how a jet may be formed via the large-scale poloidal magnetic field lines threading the accretion disc: the magnetic field lines are wrapped around (as they considered to be frozen in plasma), and the matter from the disc plane (for example, electrons travelling along the magnetic field lines) is centrifugally propelled outwards due to the disc rotation. More recent simulations have ruled out this particular mechanism (Fragile, 2008). The Blandford and Znajek (1977) model, on the other hand, showed how it is possible to launch a jet by extracting energy, electromagnetically, from a spinning black hole. This analytical model has been extended into a GRMHD simulations, showing a jet formation using only a weak dipole magnetic field in the form of the poloidal loops contained within the disc (McKinney and Blandford, 2009).

Some recent work by Ohsuga *et al.* (2009) has made great progress in showing how the disc:jet picture looks in different states. Although they have been unable to model in detail the different black hole binary states, their work has once again shown the close-knit nature of the accretion and ejection mechanisms.

The BHXB picture gets a little more complicated when, in addition to the disc and the jet, one considers the "corona" — so far only a theoretical construct to explain the observations better. Just like the disc:jet models, there are numerous models for the corona that address

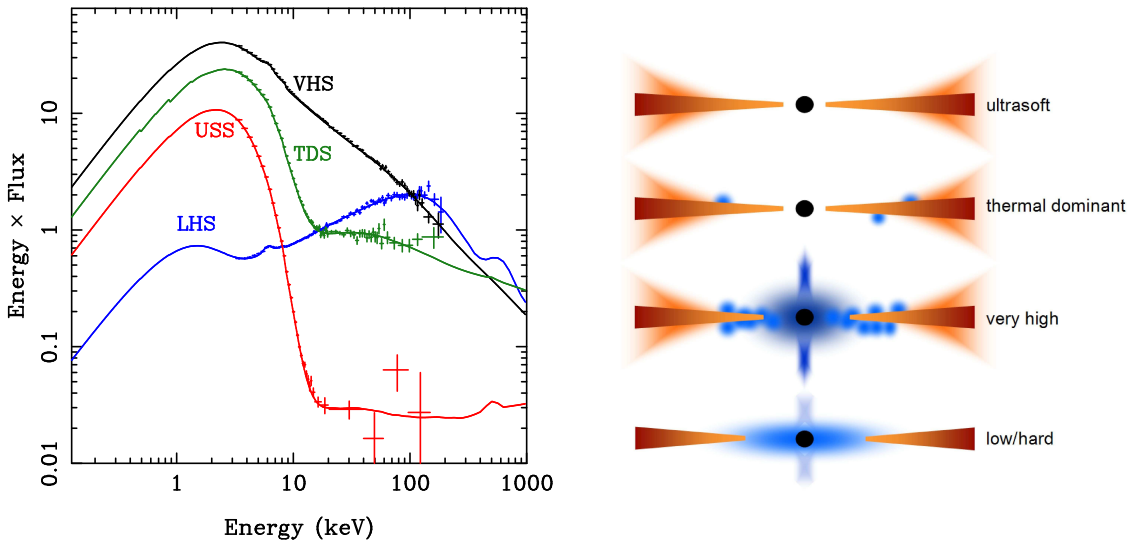

Figure 1.3: A selection of GRO J1655-40 states from the 2005 outburst. VHS: very high state; TDS: thermal dominant state; USS: ultra-soft state; LHS: low hard state. The right panel shows that assumed associate geometry for the different states. The image is from Done *et al.* (2007).

various issues. Regardless of the geometry, the corona is generally considered to contain the high energy electrons/positrons that scatter the soft X-ray photons from the disc to much higher energies by the inverse Compton process. The necessity for such a region can be better understood by looking at the BHXB spectral states.

1.2.2 BHXB spectral states

The black hole X-ray binaries appear to exist in varying states of being. Their *state* classification has traditionally been based on the multi-wavelength spectra, as well as the X-ray power spectra (see McClintock and Remillard, 2006 for a detailed review). The spectral energy distribution (SED) of an X-ray binary can vary depending on the state. Figure 1.3 shows (left panel) a compilation the source GRO J1655-40 data exhibiting the typical SEDs for the various states. The panel on the right renders the believed geometry changes that give rise to the states. The SED changes are also accompanied by the changes in the timing properties. Some of the state classifications and the associated spectral and timing behaviours are discussed below:

Quiescent State: Not shown in figure 1.3, but generally a low mass black hole X-ray binary will spend most of its life in the quiescent states: so named due to the extremely faint X-ray spectrum. The spectrum in such a state is also characterized by its power-law appearance.

Low Hard State (LHS): This state tends to be at lower luminosity than the high soft state and the spectrum can be modelled with a power-law function. Extensive work has been done, and now a well accepted picture exists on the link between the hard state and the presence of a compact radio jet. This link forms the basis of the disc:jet connection. Figure 1.4 shows the

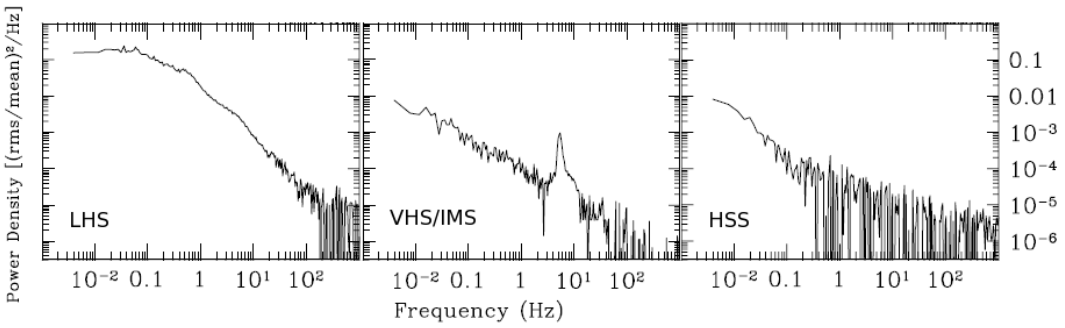

Figure 1.4: The source GX 339-4 power spectrum density in different spectral states. The images was compiled from McClintock and Remillard (2006).

power-spectra for GX 339-4 in various states. The LHS power-spectrum is typically flat topped band-limited noise (BLN), as shown in the far left panel of figure 1.4. The characteristic ν_b, or break frequency, can also be seen at $\sim$0.1 Hz. The strong Comptonization component of the SED is assumed to originate from the corona. The presence of the Comptonizing corona, plus the recessed disc (as the disc component is weak in the SED), are shown in the right panel of figure 1.3.

Very High/Intermediate State (VHS/IMS): The very high or the intermediate states are seen in transitions (when a source is moving between the hard and the soft state). These states are normally associate with a steeper spectrum than the Low State, and exhibit quasi-periodic oscillations (QPOs) in the X-ray power-spectra. These QPOs are typically in the range of 3-12 Hz. The power spectrum in figure 1.4 shows these QPOs. The SED for this state shows a strong disc component, and the presence of a Comptonization region (figure 1.3).

High Soft State (HSS/TDS): This is the thermal dominant state. The X-ray spectrum can generally be modelled with a thermal and a high energy power-law component. Fitting the strong disc component leads to the conclusions that the disc extends all the way to the ISCO. The weak power-law component suggests the presence of a partial corona. The jet is believed to be quenched when in this state. The power-spectrum in this case exhibits a weak power law noise with a smaller, compared to LHS, characteristic ν_b.

Ultrasoft State (USS): This state is quite similar to the thermal dominant state, except the power-law component in the SED is now completely missing. This therefore does not change the disc geometry (still near or at ISCO), but the Comptonizing corona is believed to have disappeared. Figure 1.3 shows the SED and the associated geometry for such a state.

The above classification, however, should be viewed as a snapshot of many source behaviours. In other words, an X-ray binary can exhibit very different properties whilst moving through the mentioned states fairly quickly. This kind of movement track is illustrated in figure 1.5. The figure illustrates how a given source can transition from one state to another along a *permitted* path. A large number of X-ray binary sources have been observed (see Fender *et al.*, 2009 for a large number of source exhibiting similar behaviour) to give rise to a similar track

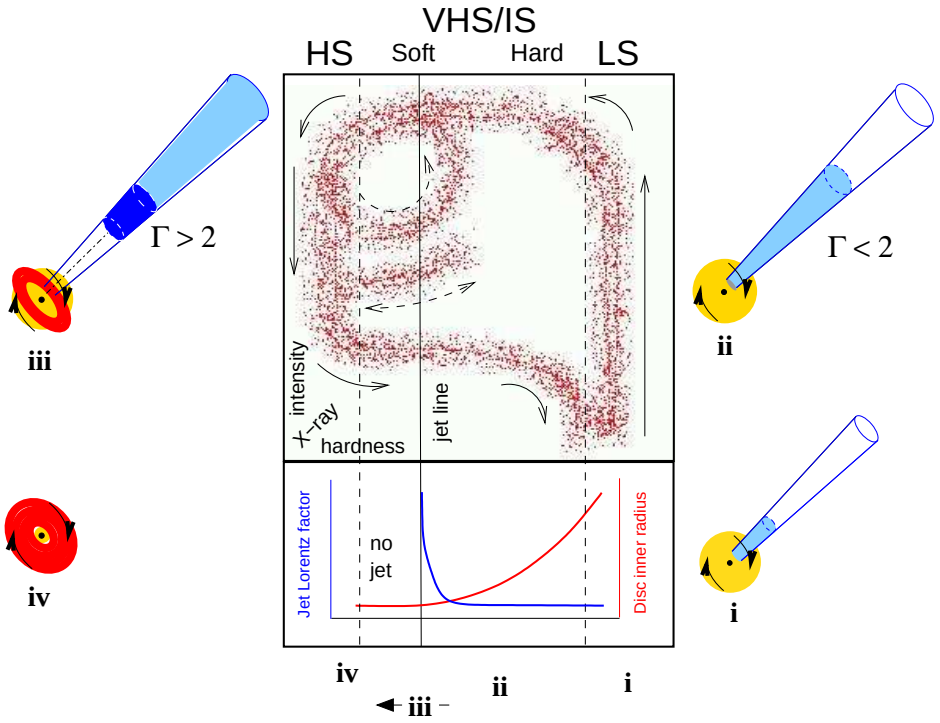

Figure 1.5: A Hardness-Intensity Diagram (HID) showing the unification of various X-ray binary states and the associated disc:jet behaviour. Γ represents the jet Lorentz factor. (i) and (ii) would be associated with the Low Hard state, the source would increase in Luminosity when moving from (i) to (ii). The horizontal transition to the High Soft state (iii) is associated with flaring(massive ejection events) and the cessation (crossing the jet-line) of the steady jet. The source can then transition back to the low state via (iv); no jet is believed to exist when in state (iv). Crossing the jet-line again on the route back from (iv) to the LS has been associated with radio outburst (ejection events). The arrows the indicate the only path the sources take. The image is from Fender *et al.* (2004).

when transitioning from one state to another. Interestingly, all these sources only take the path indicated by the arrows in figure 1.5, giving rise to the suggestion that any given source *knows* its state history. Such figures are referred to as Hardness-Intensity Diagrams (HID), because it plots the X-ray hardness[4] vs. the intensity (count rate).

The hardness-intensity diagram portrays a unified picture of all the different spectral states, plus indicate the role played by the jet. A steady jet ($\Gamma < 2$) is present in the hard state. Some models have been presented that do away with the corona in this state and suggest the base of the jet for the disc photon up-scattering (Falcke and Markoff, 2000; Markoff *et al.*, 2001). The source spectral evolution can be traced by moving along the HID. The source transitions to the soft state via the very high state. Highly relativistic jets ($\Gamma > 2$) are associated with the very high state before the source crosses the "jet line". The jet is believed to be quenched after this point and the transition is made to the soft state. The very high state also shows some very interesting timing properties that are not observed in any other state. These timing properties

[4]the *hardness* measurement can be arbitrary, but is generally defined as the measure of how dominant the power law component is over the blackbody, for example, the ratio: (6.3-10.5 keV count rate)/(3.8-6.3 keV count rate).

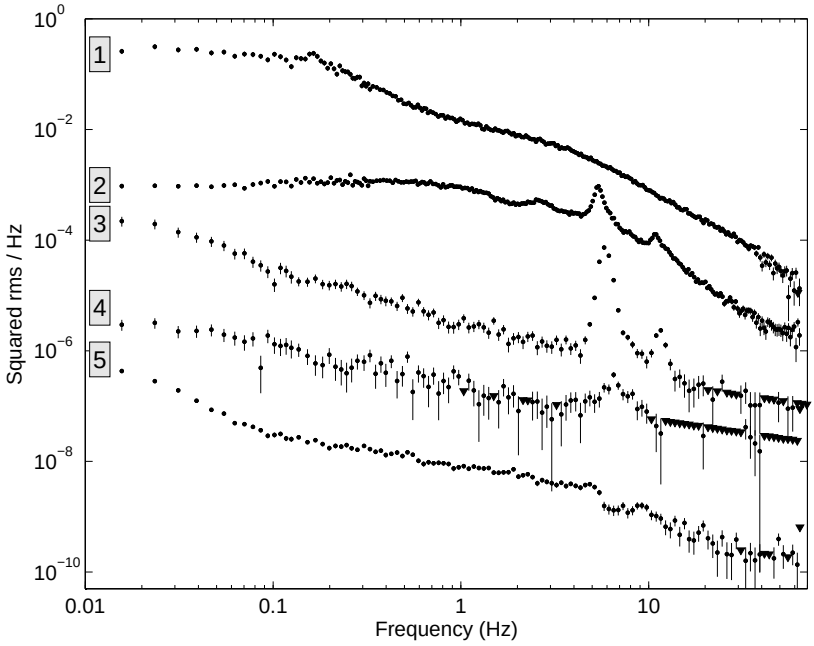

Figure 1.6: The classification of PDSs based on certain characteristics. 1: associated with the hard state (right hand side of the HID; 2: typical of intermediate states (horizontal branch of the HID); 3: also in intermediate hardness, but a narrower range than PDS-2; 4: found in even lower hardness than PDS-3; 5: associated with the soft state (far left of the HID). See text for more details. The image is from Belloni (2009).

and their possible link with the jets are explored in the next section.

1.2.3 BHXB Timing Properties

It was mentioned briefly in the previous section how the timing properties of the black hole X-ray binaries change with the state. Figure 1.4 illustrated how the power-spectrum differs, in GX 339-4, depending on the source state. In fact these properties are so prevalent that the power-spectra can be classified, and the source states, according to the presence (or the absence) of certain characteristics. This PDS classification is demonstrated in figure 1.6. The classification, corresponding to the labels in figure 1.6, is described below (Belloni, 2009).

1. PDS-1 corresponds to the hard state (right hand vertical branch of HID). The PDS can typically be fitted with a small number of broad Lorentzians components, and an occasional low frequency QPO peak. The characteristic frequencies of the components increase with the source flux

2. PDS-2 type is generally observed at intermediate hardness (the horizontal branches of HID). It is modelled with multiple Lorentzians, including the QPO peaks. The QPO centroid frequencies vary between $\sim$0.01 and $\sim$20 Hz. All the Lorentzian components, including the QPOs, vary together and are strongly correlated with the hardness: the

softer spectra correspond to the higher frequencies and lower integrated rms (root mean squared) variability. Also, only a specific type of QPO, a "type-C" (see Casella *et al.*, 2005 for low frequency QPO types), is observed in this type of PDS. A weaker band limited noise component is also present.

3. PDS-3 is found over a small range in hardness where the hardness is intermediate. It is characterized by the presence of a "type-B" QPOs. The BLN component is replaced by a steeper power law component. The QPOs show a harmonic structure similar to type-C QPOs (peak at 1/2 the frequency of the main peak is observed). The QPO frequency range is also limited to 1-6 Hz.

4. This is observed at even lower hardness than PDS-3. A "type-A" QPO is associated with this PDS type. This type of QPO is much broader and weaker than others, and restricted to a very narrow range of 6-8 Hz.

5. This PDS corresponds to the soft state of the black hole X-ray binaries (far left of HID). PDS 5 is characterized by a weak steep component with an occasional weak QPOs at frequencies $>$10 Hz.

Although the above classification is quite comprehensive it does not cover all the different types of PDS. Variations in the PDS shapes have been observed especially in the *flaring* states. As the source transitions from the hard state to the soft state, it can go through flaring (associated with radio-band flares). The flares observed in these states can be related to the highly relativistic massive ejection events (Fender and Pooley, 2000).

The massive ejection events, radio flares, have been observed in a number of sources (see Fender *et al.*, 2009 for examples). A radio flare generally signals the *end* of the steady-state jet and the source makes a transition to the soft state (crossing the jet line along the top horizontal branch of HIDs). Some interesting correlations have been found when one looks at the hardness-rms diagrams (HRD). The hardness-rms diagrams typically show a monotonic decrease in the rms variability as the spectrum gets softer. A particular area of this diagram, referred to as the "zone", indicates a dramatic change in the X-ray timing properties. This change is in the form of a sharp decrease in the rms variability. The findings by Fender *et al.* (2009) hint at a correlation between the radio flare and the X-ray timing displaying the zone-characteristics; however, no clear causal connection could be found. This demonstrates that the X-ray timing properties are intimately linked with the jet behaviour, but require further investigation to clarify, even more, the disc:jet connection.

1.3 Scaling up for the AGN

As mentioned earlier, black holes are relatively simple objects that can be described by a handful of their properties. With this in mind, one would expect that the black holes would behave the same way, no matter what size they are; this should include any systems that harbour black

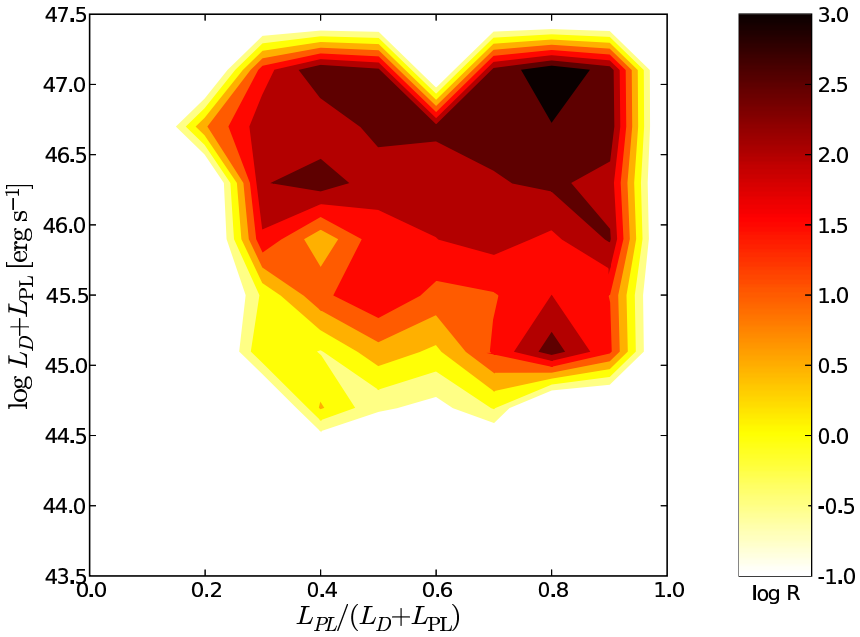

Figure 1.7: The Disc-Fraction Luminosity Diagram (DFLD) for a 4963 SDSS quasars with ROSAT detections. The far left of the x-axis corresponds to "all disc", while the far right corresponds to the "all power-law". *R* is the radio-loudness parameter. The figure is taken from Körding *et al.* (2006b).

holes (i.e. BHXB and AGN). If a super-massive black hole at the heart of a galactic centre starts to accrete, and consequently radiate, an active galactic nucleus is born (AGN). Then the question is whether the kind of relationship presented in figure 1.5 also exists for the AGN.

Of course, the main problem with observing such a behaviour in AGN is the time-scales on which changes are seen; an AGN cannot be observed to transition from one state to another. Population studies, however, can indicate how the AGN might evolve. Körding *et al.* (2006b) show how it is possible to construct an analogous (to HID) relationship for the AGN.

A Disc-fraction Luminosity Diagram (DFLD) is constructed which compares total luminosity, $L_D + L_{PL}$, with the power-law fraction, $L_{PL}/(L_D + L_{PL})$, where D and PL signify the disc and the power-law respectively. Körding *et al.* (2006b) demonstrate that when a DFLD is constructed for a simulated X-ray binary population, the same behaviour is observed.

The stellar-mass:super-massive black hole scaling also works remarkably well when one looks at the *fundamental plane of black hole activity* (Merloni *et al.*, 2003). The fundamental plane links the radio luminosity with the black hole mass and the X-ray luminosity via

$$L_{Radio} \propto L_X^{0.6} M^{0.8}. \tag{1.11}$$

The radio luminosity acts as a tracer for the enormous jet power. It would therefore be more useful to demonstrate the fundamental plane with the jet power itself, rather than use a faint

tracer like the radio luminosity. The later refinements of the plane (Falcke *et al.*, 2004; Körding *et al.*, 2006a, 2007; Gültekin *et al.*, 2009) do just that and show the same relation as the original fundamental plane, but with the jet power and the mass accretion rate replacing the radio luminosity; the accretion rate is an indicator of the rate at which the jet is being "fed" and scales linearly with the jet power.

The scaling up also applies to the variability. McHardy *et al.* (2006) have shown that the break frequency scales (ν_b) with the black hole mass and the accretion rate. This and all the other such relations re-iterate the relatively simple nature of the black holes and how they all behave the same — no matter the size.

1.4 Modelling the Jet and the Corona

In the following work I present a new internal shocks model (*i*Shocks) that is used to model X-ray binary jets. Although I have focused primarily on the X-ray binary scales during the development and the testing of this model, its structure is such that it is scale independent, making it easily adaptable to model AGN jets. The reader shall find the disc:jet environment the general theme of the present work, with the hope of extending our comprehension of these systems.

Chapter 2 describes the *i*Shocks model, and demonstrates some of its capabilities. Chapter 3 focuses on application of the model and showing how a solution to the long standing flat/inverted spectrum (with adiabatic energy losses) problem has been found. Chapter 3 also shows the application of *i*Shocks to the repeated giant ejections from the source GRS 1915+105.

Chapter 4 explores the X-ray/optical correlations in black hole X-ray binaries. Once again, the *i*Shocks model is applied to this scenario with the aid of translating the X-ray variability into jet parameters and studying the resultant "X-ray"/optical correlations.

Chapter 5 is a slight digression from the *jet theme* of the other chapters: I have implemented pair (electron-positron) annihilation in the high energy radiative transfer model (HEART). The lepton pair annihilation is modelled in a corona, in addition to other radiative processes (Compton scattering, bremsstrahlung), to study the presence (or lack) of the 511 keV line in X-ray binaries. This type of study gives us great clues to the conditions present in these coronae, and ultimately in the X-ray binary systems.

2

An Internal Shocks Model

The details of our internal shocks model (*i*Shocks), developed for simulating relativistic jets, are outlined in the following chapter. The first part describes some of the other jet models and any of associated drawbacks. The rest of the chapter is concerned with our model and how it improves upon the existing picture. The general focus of the following work shall remain on X-ray binary jets.

2.1 Previous models

With an array of relativistic jet models available, it is important to understand the underlying assumptions and any drawbacks these models may have. Due to the inherent complexity of the systems being modelled, AGN and X-ray binaries can only be simulated by having some simplifying assumptions. For this reason, different models have their niches and no model is able to explain all of the sources' behaviours.

A *flat spectrum* is one of the identifying features of a compact radio source; "flat" refers to the shape of the spectrum ($\alpha \sim 0$ if the spectrum $S_\nu \propto \nu^{-\alpha}$). This flat spectrum is generally considered to be as a result of self-absorbed synchrotron radiation from a conical relativistic jet. However, previous models have had to make a number of key assumptions in order to reproduce these observations.

One of the most successful and influential jet models was introduced by Roger Blandford and Arieh Königl in 1979 (Blandford and Königl, 1979). Their model showed how it is possible to obtain a flat spectrum via the self asbsorbed synchrotron radiation originating from a relativistic jet. The flat spectrum results from the super-position of many self absorbed syn-

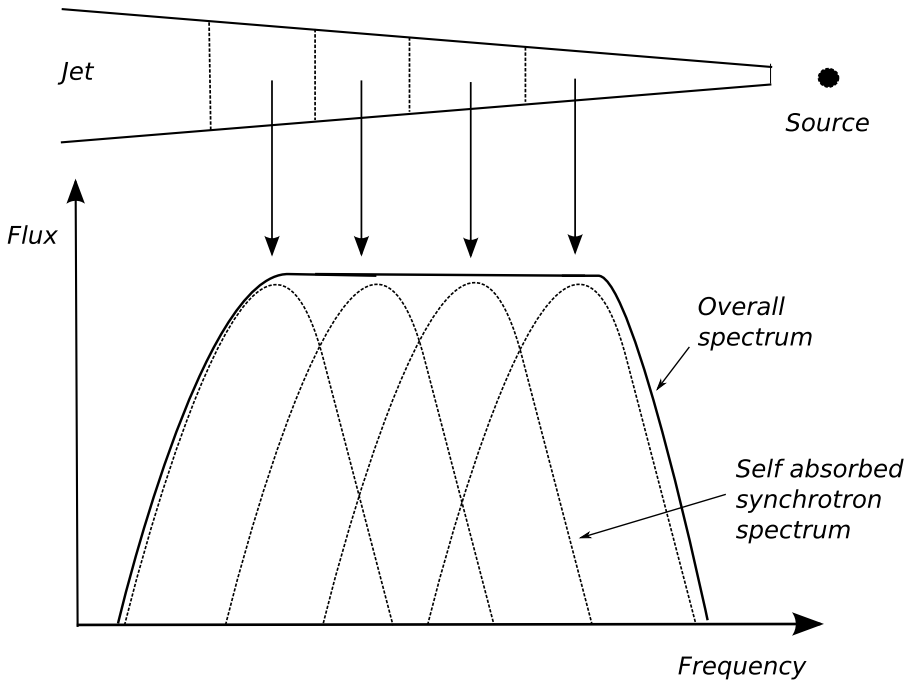

Figure 2.1: An illustration of how a flat spectrum can be achieved via the superposition of individual self absorbed synchroton spectra.

chrotron spectra from different parts of the jet. The higher frequencies are emitted from the inner parts of the jet, while the lower frequencies originate from the outer parts of the jet. This is illustrated in figure 2.1. The figure shows how the individual synchrotron peaks are shifted to lower frequencies as we move along the jet. (The details of synchrotron emission are discussed in section 2.3.5.) The synchrotron peak frequency is influenced heavily by the volume of the emitting region: a larger volume means a lower peak frequency. However, this is where the Blandford and Königl (1979) model also has a drawback: the adiabatic energy losses, due to increase in the volume, are neglected. The authors assume a constant re-acceleration all along the jet. In other words, a constant replenishment of any energy losses suffered by the emitting electrons.

Alan Marscher introduced another jet model (Marscher, 1980). The jet geometry in his model includes a "nozzle" region which leads to a conical part of the jet. In the nozzle the emitting electrons go through a single acceleration episode to a power-law energy distribution. These electrons subsequently give rise to the synchrotron spectrum. The model also take the adiabatic energy losses into account. Unfortunately, this model is unable to reproduce a flat spectrum because a single acceleration episode does not appear to be sufficient. Falcke and Biermann (1995) present a more complicated model that has a similar geometry. Their model is applied mainly to quasars [although microquasar application has also been explored by Markoff *et al.* (2001)], with the jets also contributing to the X-ray emission. The focus of Falcke and Biermann (1995) and Markoff *et al.* (2001) models is on the higher energy emission, and no real effort is made to reproduce a flat spectrum ranging from the radio frequencies up to the

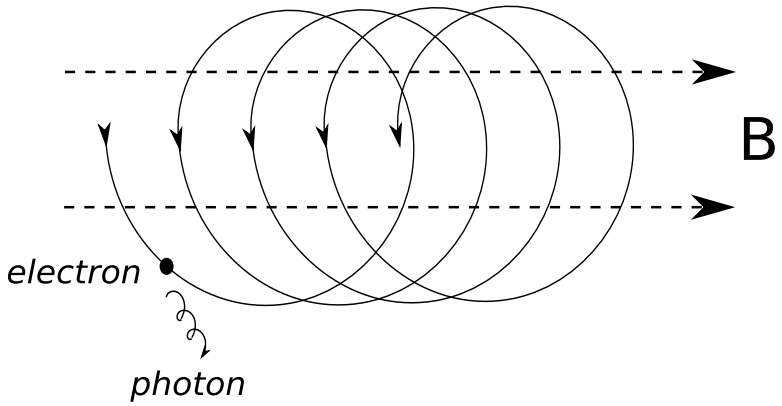

Figure 2.2: An electron will take a helical trajectory in a straight magnetic field: the electron acceleration results in radiation.

infrared (commonly associated with a steady jet in XRBs).

Hjellming and Johnston (1988) presented a jet model to explain the observations of the source SS433. They modelled the jet in the form of a "twin-jet". They model the jet in the form of a two-flow, or in other words, a jet inside a jet. Different layers within the jet then give rise to different emissions. They are able to reproduce a flat spectrum, but require a *slowed* lateral expansion of the jet. The slowed expansion helps to control the adiabatic losses. Once again we can see it is difficult to reproduce a flat spectrum whilst self consistently taking the adiabatic losses into account.

More recently, models by Kaiser (2006) and Pe'er and Casella (2009) further explore the flat spectrum and the involvement of the adiabatic and radiative energy losses. Kaiser (2006) showed how it is possible to obtain a flat spectrum with a conical jet, if only the radiative energy losses are considered; the presence of the adiabatic energy losses produces a highly inverted spectrum (unless a non-conical jet geometry is assumed).

All these studies therefore lead us to conclude that either the assumed conical jets do not suffer from adiabatic energy losses or some mechanism replenishes the energy losses. Here, the latter is assumed and further explored with our model.

2.2 Physical processes

Before outlining how our model works, it is important to describe the physical processes that are essential and inherent to the workings of our, and many other, jet models. Two of the main processes are the synchrotron radiation and the acceleration of high energy particles.

2.2.1 Synchrotron radiation

A treatment of synchroton radiation can be found in Rybicki and Lightman (1979). However, some of the key principles are outlined below.

An electron accelerating in a magnetic field, **B**, radiates. Figure 2.2 demonstrates the princi-

ple of electron acceleration in a magnetic field. The electron takes a helical trajectory with the acceleration perpendicular to the velocity. If the particle is non-relativistic then the radiation is referred to as the cyclotron radiation, where the emission frequency corresponds to the gyration frequency. However, if the particle in question is relativistic, then the emission is referred to as synchrotron radiation. The emission frequency calculation in this case is more complex. The emitted radiation has a particular profile: it is beamed into a cone along the direction of motion. Due to this beaming effect, and when the radiation cone matches the observer direction, an observer sees pulses of radiation from such an electron. The period of these pulses can be much smaller than the gyration period (by a factor of γ^3, where γ is the electron Lorentz factor).

With the pulse being quite narrow (temporally), the synchrotron spectrum is quite broad, due to the relation:

$$\Delta t \Delta \omega > 1 \, , \tag{2.1}$$

where ω is the frequency ($= 2\pi f$). The broad synchrotron spectrum, however, has quite a sharp cut off after the critical frequency:

$$\omega_c = \frac{3\gamma^2 qB\sin\alpha}{2mc} \, , \tag{2.2}$$

with q and m representing the charge and the mass of the emitting particle. Typically, the spectrum is peaked at the critical frequency. If the spectrum is calculated for a single electron, then this can be generalized to a whole distribution. There is a particularly simple relationship between a power-law electron energy distribution and the spectral index of the synchrotron spectrum:

$$\alpha = \frac{p-1}{2}, \tag{2.3}$$

where s is the spectral index and p is the power-law index of the electron distribution. As mentioned earlier, our focus is on the self-absorbed synchrotron spectrum. The spectrum in that case looks different.

In addition to emitting a photon, an electron can also absorb a photon in the presence of a magnetic field. This self absorption results in the spectrum taking the peaked shape (see the individual peaks in figure 2.1). For a power-law energy distribution of electrons,the self absorbed, optically thick [1], part of the spectrum follows the relation $\nu^{5/2}$ whilst the optically thin part follows $\nu^{-(p-1)/2}$. The spectrum calculation is discussed further in section 2.3.5.

2.2.2 Shock acceleration

Enrico Fermi proposed a stochastic acceleration mechanism by which the particle collisions with the interstellar clouds would result in the colliding particles being accelerated to higher energies (Fermi, 1949); he suggested this as the origin of the high energy cosmic rays. This

[1] true for a power-law energy distribution of emitting electrons; therefore the electrons emitting at different frequencies are actually at different effective temperatures. The thermal emitting population at a single temperature would give rise to a different spectral index.

original acceleration process is now referred to as the *Fermi second order acceleration*: the reason for this is that only the second order term in the energy of the particles sees a gain. This process involves the particles "bouncing" off a large molecular cloud. Depending on whether the collision is head-on (this results in maximum energy gain) or tail-on, the energy gains vary. Blandford and Eichler (1987) later expanded on this process and gave a more thorough treatment of the process. Once accelerated, the particles end up in a power-law distribution. However, the Fermi second order acceleration is still not the most efficient method for accelerating particles.

The *Fermi first order acceleration* (Blandford and Ostriker, 1978; Bell, 1978) on the other hand holds more promise for higher acceleration efficiencies. In this case, a shock is viewed as passing through a medium with different plasma properties in front of and behind the shock front. In this process, particles gain energy at every crossing of the shock front. In other words, we end up with repeated "head-on" collisions for particle acceleration. The first order acceleration therefore is a lot more efficient and still produces a power-law energy distribution of electrons.

The shocks in our model, although not modelled in detail, are analogous to the Fermi first order acceleration; the passage of shock front through a shell results in the re-energization of the electrons and the magnetic field.

2.3 The *i*Shocks Model

Our model (*i*Shocks) is based on the Spada *et al.* (2001) internal shocks model for radio-loud quasar. Many modifications have been carried out to make the model more flexible, and applicable to different scales and scenarios. The jet is simulated using discrete packets of plasma or *shells*. Only the jets at relatively large angle of sight are modelled: this is because the Comptonization effects and the influence of radiation from one shell on another shell are not taken into account. Each shell represents the smallest emitting region and the spatial resolution in the model is limited to the shell size. While the simulation is running, the jet can "grow" with the addition of shells at the base while the previously added shells move further along the jet. If the time interval between consecutive shell injections is kept small, a continuous-jet approximation can be achieved. Variations in the shell injection time gap and velocity cause the faster shells to catch up with the slower ones, leading to collisions: the internal shocks, discussed later, are a result of these shell collisions. A schematic of the model set up is shown in figure 2.3. The two conical frusta shown represent the shells.

2.3.1 Shell properties

The shell volume is based on a conical frustum (cone opening angle = jet opening angle, φ). As a shell moves along the jet, it can expand laterally as well as longitudinally (figure 2.3). The emitting electron energy distribution is assumed to be power-law in nature; each shell contains

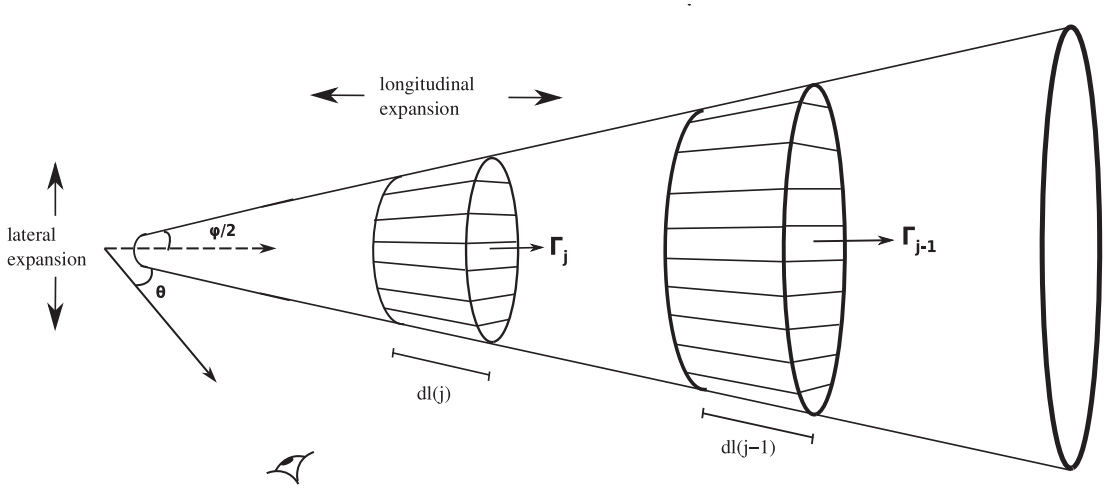

Figure 2.3: An illustration of shells in our jet model. If the outer boundary of the inner shell, (j), contacts the inner boundary of the outer shell, (j-1), a collision is said to occur. The lateral expansion is due to jet opening angle; the longitudinal expansion is due to the shell walls expanding within the jet. The illustration is not to scale.

its own distribution. The power-law energy distribution is of the form:

$$N(E)\mathrm{d}E = \kappa E^{-p}\mathrm{d}E \ , \tag{2.4}$$

where $E = \gamma mc^2$ is the electron energy, p is the power-law index and κ is the normalization factor. If the total kinetic energy density of electrons, E_k, and the electron energy is expressed in terms of the Lorentz factor, then κ' can be calculated for the two cases of power-law index: $p \neq 2$, and $p = 2$. (κ and κ' are related via $\kappa = \kappa'(m_e c^2)^{(p-1)}$). We have:

$$E_k = \int_{\gamma_{min}}^{\gamma_{max}} \kappa' \gamma^{-p}(\gamma - 1)\mathrm{d}\gamma \tag{2.5}$$

which can be solved in general when $p \neq 2$, to get:

$$\begin{aligned} E_k &= \kappa' \left[\frac{1}{2-p}(\gamma_{max}^{(2-p)} - \gamma_{min}^{(2-p)}) \right. \\ &- \left. \frac{1}{(1-p)}(\gamma_{max}^{(1-p)} - \gamma_{min}^{(1-p)}) \right] \ , \end{aligned} \tag{2.6}$$

equation 2.5 can also be solved for the special case of $p = 2$:

$$E_k = \kappa' \left\{ [\ln(\gamma_{max}) - \ln(\gamma_{min})] + [\gamma_{max}^{-1} - \gamma_{min}^{-1}] \right\} \ , \tag{2.7}$$

where the subscripts *max* and *min* denote upper and lower energy bounds for the electron energy distribution. The relations given in equations 2.6 and 2.7 can therefore be used to calculate the change in the power-law distribution normalization when there is a change in the total kinetic energy, assuming the power-law index and γ_{min} are fixed.

A magnetic field is essential to give rise to the synchrotron radiation. In the shells, the magnetic field is assumed to be randomly oriented and constantly tangled in the plasma, leading to an assumption that the magnetic field is isotropic, and, that it can be treated like an ultra-relativistic gas (Heinz and Begelman, 2000). If the magnetic energy density (E_B) is given, the field (B) can be calculated:

$$E_B = \frac{B^2}{2\mu_0} , \tag{2.8}$$

where μ_0 is the magnetic permeability of free space.

Other shell properties include the shell bulk Lorentz factor, Γ, and the shell mass, M. These quantities remain constant throughout the lifetime of a given shell. If there is variability in the Γ of the shells being modelled, then the faster inner shells are able to catch up with the slower outer ones, causing shell collisions; the shell collisions create internal shocks, which ultimately generate the internal energy. The shell bulk Lorentz factor and mass are re-calculated upon a collision.

2.3.2 Internal shocks

When two shells collide, a shock forms at the contact surface. Some of the steps involved in a two-shell collision, and the subsequent merger, are illustrated in figure 2.4. The collisions are considered to be inelastic. With many shells present inside the jet, the next collision time between two shells needs to be calculated first: a collision is said to occur when the outer boundary of the inner shell, R_j^{outer}, comes in contact with the inner boundary of the outer shell, R_{j-1}^{inner}. The following relation can be used to calculate the time interval for a two shell collision:

$$\mathrm{d}t_{coll} = \frac{R_{(j-1)}^{inner} - R_{(j)}^{outer}}{(\beta_{(j-1)}^{e} + \beta_{(j)}^{e})c + (\beta_{(j)} - \beta_{(j-1)})c} , \tag{2.9}$$

where the subscripts $j-1, j$ denote the two consecutive shells, β^e is the shell longitudinal expansion velocity (along the jet axis), and β is the shell velocity ($= \sqrt{\Gamma^2 - 1}/\Gamma$); $\mathrm{d}t_{coll}$ is calculated for all the shells inside the jet and the minimum of these collision time gaps is selected, that is, the next earliest collision. The shell longitudinal expansion (β^e) is due to any thermal energy the shell may have. We do not explicitly model a thermal electron population; however, the expansion effects of having such a population are incorporated into the model. The shell expansion velocity is given by (Spada *et al.*, 2001):

$$\beta^e = \frac{2\beta_s'}{\Gamma^2} \frac{1}{1 - (\beta\beta_s')^2} , \tag{2.10}$$

where $\beta_s = v_s'/c$ corresponds to the sound velocity in the plasma (in the shell rest frame), and:

$$v_s' = \sqrt{\frac{1}{3}\frac{E_{th}'}{M}} , \tag{2.11}$$

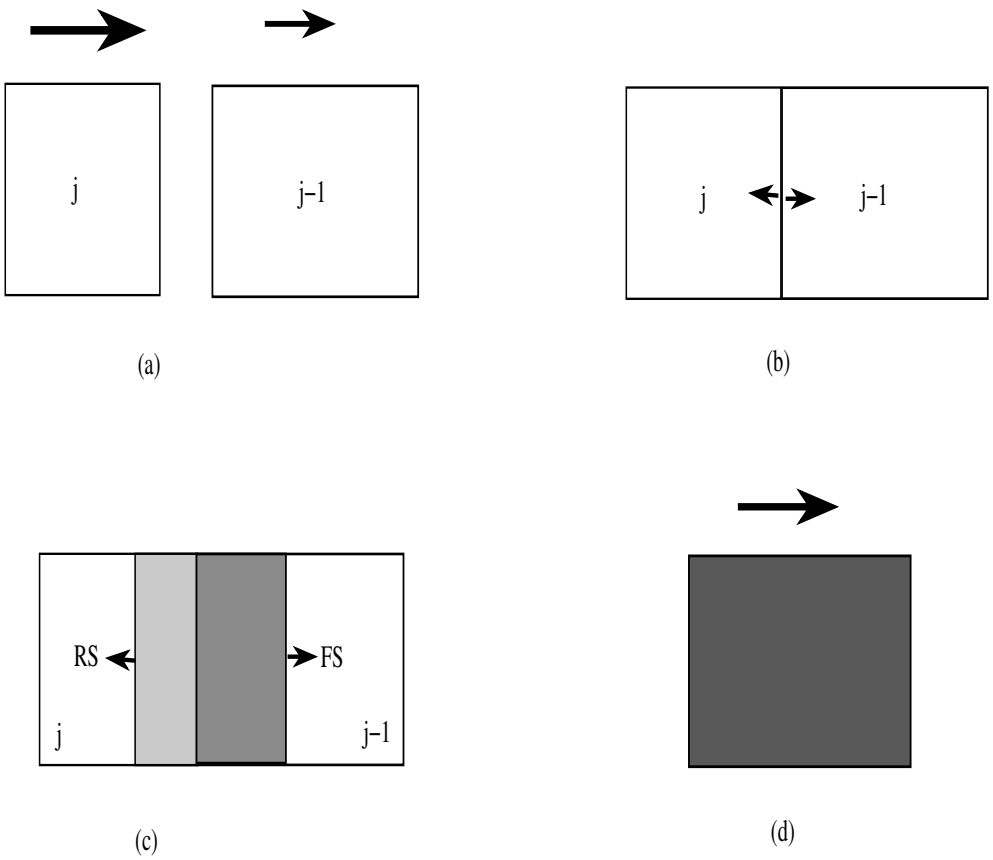

Figure 2.4: An illustration of a two shell collision leading to a merger: (a) when the inner shell, j, comes in contact with the outer shell, j-1, (b) a shock starts to form; (c) the forward shock, FS, travels through the outer shell while the reverse shock, RS, travels through the inner shell; (d) once shock fronts have traversed the two shells, a new 'merged' shell is formed.

with E'_{th} being the shell thermal energy and M is the shell mass. The prime denotes quantities in the shell rest frame. The Panaitescu and Mészáros (1999) treatment of a shock propagation is followed to work out various quantities associated with the shock itself. The shock propagation can be split into two shock-fronts: a forward shock travelling from the contact surface and through the outer shell $(j-1)$, and a reverse shock travelling through the inner shell (j) (injected after shell $(j-1)$). Once the shock-front has passed through, the plasma/shell is considered to be *shocked* (S) and will have different physical properties compared with the unshocked plasma (see figure 2.4). In one of the shells' rest-frame, the shock-front's (SF) velocity can be calculated as:

$$\beta'_{SF} = \frac{(\Gamma'_S - 1)(\hat{\gamma}\Gamma'_S + 1)}{\beta'\Gamma'_S[\hat{\gamma}(\Gamma'_S - 1) + 1]} \,, \tag{2.12}$$

$\hat{\gamma}$ is the adiabatic index and Γ'_S corresponds to the shocked plasma and is given by:

$$\Gamma'_S = \Gamma_m \Gamma(1 - \beta_m \beta) \,, \tag{2.13}$$

where the subscript m denotes the merged shell properties. A merged shell forms once the shock-fronts have passed through both the colliding shells, leaving a single combined shell. The merged shell mass is simply a linear combination of the two merging shells, that is:

$$M_m = M_{(j)} + M_{(j-1)} \ . \tag{2.14}$$

The merged shell Lorentz factor is given by (Kobayashi *et al.*, 1997):

$$\Gamma_m = \left(\frac{\mu_{(j)}\Gamma_{(j)} + \mu_{(j-1)}\Gamma_{(j-1)}}{\mu_{(j)}/\Gamma_{(j)} + \mu_{(j-1)}/\Gamma_{(j-1)}} \right)^{1/2} \ , \tag{2.15}$$

where $\mu = M + \eta/c^2$ and η is the shell internal energy. However, this is only valid if $\Gamma_{(j)}, \Gamma_{(j-1)} >> 1$. The exact calculation can be done in the following way. The conservation of energy gives (for convenience of notation j and $j-1$ have been replaced by 1 and 2):

$$\Gamma_1\mu_1 + \Gamma_2\mu_2 = \Gamma_m(M_m + \eta_m/c^2) \ . \tag{2.16}$$

While the conservation of momentum gives:

$$\Gamma_1\mu_1\beta_1 + \Gamma_2\mu_2\beta_2 = \Gamma_m(M_m + \eta_m/c^2)\beta_m \ , \tag{2.17}$$

where β has the usual meaning and is equal to $\sqrt{1-1/\Gamma^2}$. Combining equations 2.16 and 2.17, we get:

$$\beta_m = \frac{\Gamma_1\mu_1\beta_1 + \Gamma_2\mu_2\beta_2}{\Gamma_1\mu_1 + \Gamma_2\mu_2} \ , \tag{2.18}$$

which can be used to calculate the Γ_m, that is also valid for low Γ_1, Γ_2 as well.

Because the shell collisions are considered to be inelastic, a certain amount of internal energy is also generated. This can be given by:

$$\begin{aligned} E_{int} &= E_{tot} - E_{kin} \\ &= (\Gamma_1\mu_1 + \Gamma_2\mu_2) - (\Gamma_M)[(\mu_1 - \eta_1) + (\mu_2 - \eta_2)] \\ &= \Gamma_1\mu_1 + \Gamma_2\mu_2 - \Gamma_m\mu_1 + \Gamma_m\eta_1 - \Gamma_m\mu_2 + \Gamma_m\mu_2 \\ &= (\Gamma_1 - \Gamma_m)\mu_1 + (\Gamma_2 - \Gamma_m)\mu_2 + \Gamma_m\eta_1 + \Gamma_m\eta_2 \end{aligned} \tag{2.19}$$

where η_i is the internal energy and $\mu_i = M_i + \eta_i/c^2$ for the two colliding shells. The efficiency of such a two-shell collision is given by:

$$\varepsilon = \frac{(\Gamma_1 - \Gamma_m)\mu_1 + (\Gamma_2 - \Gamma_m)\mu_2 + \Gamma_m\eta_1 + \Gamma_m\eta_2}{\Gamma_1\mu_1 + \Gamma_2\mu_2} \tag{2.20}$$

The formula given in equation 2.19 has the extra Γ_m factors which are missing in the internal

energy formula given in Spada *et al.* (2001):

$$E_{in} = \eta_1 + \eta_2 + \mu_1 c^2(\Gamma_1 - \Gamma_m) + \mu_2 c^2(\Gamma_2 - \Gamma_m) \ . \tag{2.21}$$

As mentioned earlier, Spada *et al.* (2001) treatment of internal shocks has been followed primarily, and therefore the equations given in 2.15 and 2.21 have been used instead of the exact solutions. The implications of these differences are discussed later.

Once the quantities, outlined above, associated with the shocked plasma are calculated, we are able to determine the new merged shell length. The shock propagation through the plasma has a compression effect on the shells. The merged shell length is given by:

$$\mathrm{d}l_m = \frac{\mathrm{d}l_1}{\rho_1} + \frac{\mathrm{d}l_2}{\rho_2} \ , \tag{2.22}$$

and the density, ρ, is:

$$\rho = \frac{\Gamma_m}{\Gamma} \frac{\hat{\gamma}\Gamma'_S + 1}{\hat{\gamma} - 1} \ . \tag{2.23}$$

The Lorentz factor, Γ, corresponds to one of the two shells involved in the collision while Γ'_S is given by equation 2.13. We do not consider the re-energization of the new merged shell to be instantaneous. Instead, the energy is dissipated over a time period that the shock-fronts would take to cross the inner and outer shells i.e.

$$\mathrm{d}t_{ER} = \frac{\mathrm{d}l_1}{\beta_{RS}} + \frac{\mathrm{d}l_2}{\beta_{FS}} \ , \tag{2.24}$$

where the subscripts ER, FS and RS denote the energy release (time), the forward shock and the reverse shock respectively. Due to limitations in the way the shocks are modelled, the merged shell is given the corresponding length (equation 2.22) at the point of creation; only the energy release is delayed over time $\mathrm{d}t_{ER}$. If adiabatic energy losses are taken into account, then the merged shell will also be losing energy during the period $\mathrm{d}t_{ER}$.

2.3.3 Adiabatic losses

For an expanding conical jet, the adiabatic energy losses must be taken into account. These energy losses are due to the work done by the jet material while expanding. Implicit assumptions are made about the pressure gradient across the jet boundary that would result in a conical jet.

The internal energy for a gas with d_f degrees of freedom, N particles, and temperature T is given by:

$$U = d_f \frac{1}{2} N k_B T \ , \tag{2.25}$$

where k_B is the Boltzmann constant. The degrees of freedom are related to the adiabatic index via:

$$d_f = \frac{2}{(\hat{\gamma} - 1)} \ . \tag{2.26}$$

Therefore,

$$U = \frac{1}{(\hat{\gamma}-1)} N k_B T \ . \tag{2.27}$$

(At this stage, using $\hat{\gamma} = 4/3$ for a relativistic gas can be used to derive a specific case. However, we shall continue to derive a general case.) We also know that:

$$\begin{aligned} PV &= N k_B T && (2.28)\\ \therefore U &= \frac{1}{(\hat{\gamma}-1)} PV && (2.29)\\ \Longrightarrow PV &= (\hat{\gamma}-1)U \ . && (2.30) \end{aligned}$$

also,

$$\begin{aligned} dU &= -P dV && (2.31)\\ dU &= -PV\frac{dV}{V} && (2.32) \end{aligned}$$

using 2.30,

$$\begin{aligned} dU &= -(\hat{\gamma}-1)U\frac{dV}{V} && (2.33)\\ \Longrightarrow \frac{dU}{U} &= -(\hat{\gamma}-1)\frac{dV}{V} && (2.34)\\ \Longrightarrow \ln U &= -(\hat{\gamma}-1)\ln V \ . && (2.35) \end{aligned}$$

Using the above and applying to a change in the energy and volume, we get:

$$\begin{aligned} \ln U - \ln U_0 &= -(\hat{\gamma}-1)(\ln V - \ln V_0) && (2.36)\\ \Longrightarrow \ln(\frac{U}{U_0}) &= -(\hat{\gamma}-1)\ln(\frac{V}{V_0}) && (2.37)\\ \Longrightarrow \ln(\frac{U}{U_0}) &= \ln(\frac{V}{V_0})^{-(\hat{\gamma}-1)} && (2.38)\\ \Longrightarrow \frac{U}{U_0} &= (\frac{V}{V_0})^{-(\hat{\gamma}-1)} && (2.39) \end{aligned}$$

Assuming that all the synchrotron emitting electrons are highly relativistic the above relation can be written as:

$$\frac{\gamma}{\gamma_0} = \left(\frac{V}{V_0}\right)^{-(\hat{\gamma}-1)} \ , \tag{2.40}$$

with the adiabatic index, $\hat{\gamma} = 4/3$; subscripts '0' denote the quantities before the change in volume; the Lorentz factor γ corresponds to the power-law electrons accelerated to high energies due to the shock-front passing through the plasma. Therefore the adiabatic energy losses for the kinetic energy contained in the power-law electron distribution can be calculated using

equation 2.40. To calculate the change in the power-law normalization, κ, for a change in volume, the treatment is followed: If $\gamma >> 1$ then $E_k = (\gamma - 1)m_e c^2$ can be approximated by $\gamma m_e c^2$. The conservation of total number of electrons gives:

$$\begin{aligned} (N_0 &=)V_0 \kappa_0 \gamma_0^{-p} \mathrm{d}\gamma_0 = V \kappa \gamma^{-p} \mathrm{d}\gamma (= N) && (2.41) \\ \kappa &= \frac{V_0 \kappa_0 \gamma_0^{-p} \mathrm{d}\gamma_0}{V \gamma^{-p} \mathrm{d}\gamma} && (2.42) \\ \implies \kappa &= \left(\frac{V_0}{V}\right) \left(\frac{\gamma_0}{\gamma_0}\right)^{-p} \left(\frac{\mathrm{d}\gamma_0}{\mathrm{d}\gamma}\right) \kappa_0 \,, && (2.43) \end{aligned}$$

which can be solved when equation 2.40 is used to solve for change in volume. We finally get:

$$\kappa = \kappa_0 \left(\frac{V}{V_0}\right)^{p+\hat{\gamma}(1-p)-2} . \tag{2.44}$$

Once the initial power-law normalization is calculated using equation 2.6 or 2.7, the above relation can then be used to calculate the subsequent changes in the normalization (with an appropriate adiabatic index, for example, 4/3). If the shell is involved in a collision then the distribution is re-calculated completely. The change in the maximum Lorentz factor of the electrons, γ_{max}, as the shell volume changes, can be calculated using equation 2.40. The combined effect of varying γ_{max} and κ is to effectively *evolve* the power-law electron energy distribution.

Changes in the magnetic energy density can also be determined in a similar manner. If we assume that the magnetic field is constantly tangled in plasma and treat it is as an ultra-relativistic gas, we can calculate the changes in magnetic pressure, $P(B)$ using:

$$PV^{\hat{\gamma}} = P_0 V_0^{\hat{\gamma}} \,, \tag{2.45}$$

therefore,

$$P(B) = P_0(B) \left(\frac{V}{V_0}\right)^{-\hat{\gamma}} \,, \tag{2.46}$$

where the adiabatic index is once again = 4/3.

2.3.4 Implications of calculating Γ_m and E_{int} differently

We can look at the quantitative difference made by the changes in Γ_m and E_{int} formulae. The range of Γ's shall be restricted to the kind of regimes we are interested in the present work. Although, as we shall see, the impact of using approximations instead of exact solutions is minimal, it is important that any future work carries out exact calculations.

2.3.4.1 Difference in bulk Lorentz factor (BLF)

Figure 2.5 shows the difference between an exact and an approximate calculation of the bulk Lorentz factor of the merged shell. The approximation (equation 2.15) overestimates the merged BLF and is particularly poor when the two colliding shells have very different BLF.

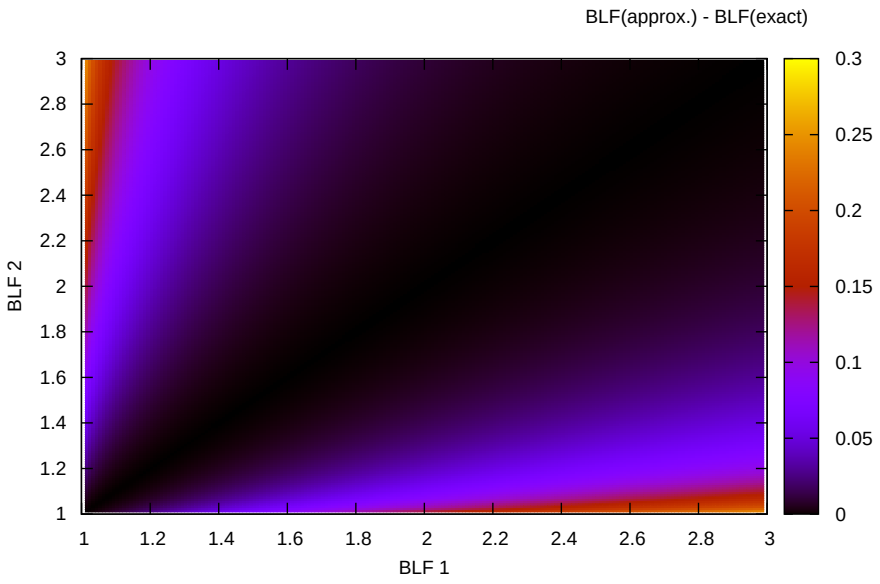

Figure 2.5: The map shows how the merged bulk Lorentz factors differ depending on approximate formula (equation 2.15) or the exact calculation (2.18).

2.3.4.2 Difference in merger efficiency

Inspecting equation 2.20, it is clear that the merged BLF affects the efficiency of the shell collisions. Figure 2.6 shows the efficiencies possible for a range of Γ_1 and Γ_2. The correct internal energy and Γ_m formulae are used to calculate the efficiency. On the hand, figure 2.7 shows how the collision efficiency changes when equation 2.15 is used to calculated BLF. The efficiency increases when 2.18 is used to calculate Γ_m. The collision efficiency presented here assumes no existing internal energy. Therefore the missing Γ_m factors, mentioned in section **??**, do not have an influence. However, if the colliding shells do have internal energy present, and the correct internal energy formula (equation 2.19) is used, the efficiency would be improved when compared to the formula with the Γ_m factor missing.

2.3.5 Partially self absorbed synchrotron emission

To model the self absorbed synchrotron radiation, we employ the treatment outlined in Longair (1994). With only the power-law electrons present, the synchrotron emission calculation is simplified; the monochromatic synchrotron intensity is given by:

$$I_\nu = \delta_{\mp}^3 \frac{J_\nu}{4\pi\chi_\nu}(1 - e^{-\chi_\nu r}) \; . \tag{2.47}$$

The emission coefficient, J_ν, and the absorption coefficient, χ_ν, are given by Longair (1994) (see appendix A for the numerical values); r is the shell radius ($\tau_\nu = \chi_\nu r$); the Doppler factor,

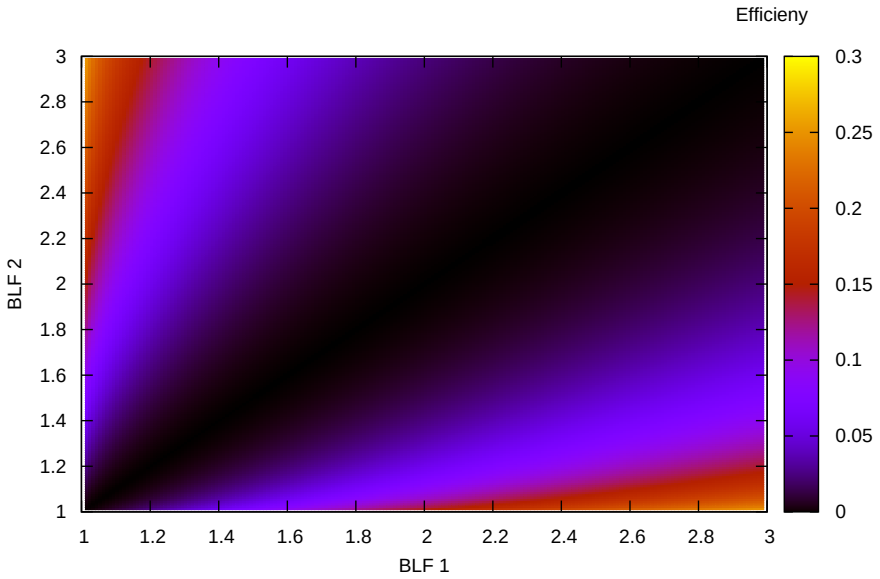

Figure 2.6: The map shows how the collision efficiency as a function of the two colliding shell BLFs. The formula outlined in equation 2.20 is used to calculate the efficiency.

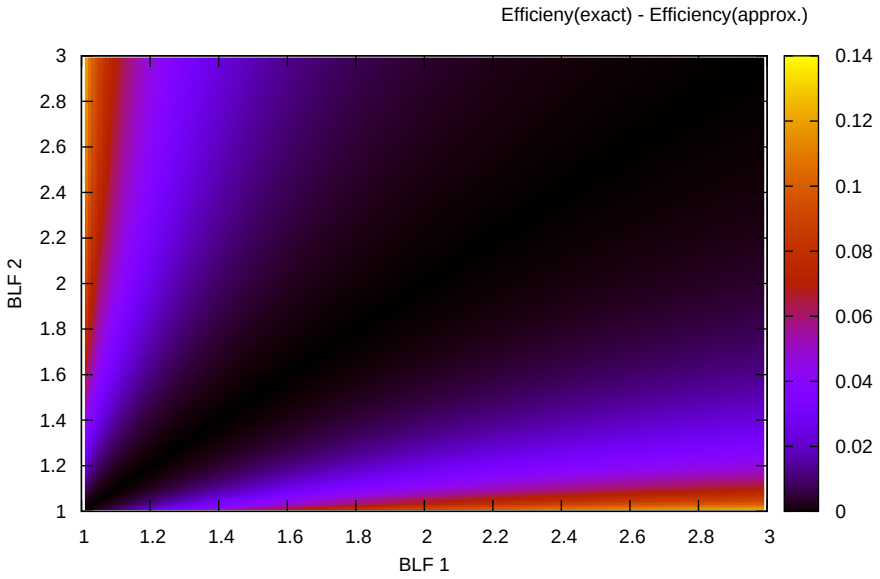

Figure 2.7: The map shows how the collision efficiency changes with different merged BLFs. The efficiency calculated using approximate merged BLF is subtracted from the efficiency using exact merged BLF.

$\delta_{\mp}$, is:

$$\delta_{\mp} = [\Gamma(1 \mp \beta(\cos\theta)]^{-1} \ , \tag{2.48}$$

where, θ is the jet viewing angle and '$\mp$' corresponds to either an approaching or a receding component of the jet.

If the shell area is given by A and the distance to the jet is D, then the flux, dF_ν, from a single shell has the following form:

$$\mathrm{d}F_\nu = \delta_{\mp}^3 \frac{A}{4\pi^2 D^2} \frac{J_\nu}{\chi_\nu}(1 - e^{-\chi_\nu r}) \ . \tag{2.49}$$

The above relations are used to self consistently calculate the synchrotron spectrum as it varies with the shell properties. When the shell expands, its optical depth with respect to a given frequency also changes; hence, a shell that is optically thick to a given frequency can become optically thin to the same frequency, as it moves along the jet. The emission for a frequency ν usually peaks when the optical depth for that frequency is unity ($\tau \sim 1$). It should be noted that some of the relativistic effects, such as the aberration effect, which would affect the shell area calculation are not taken into account. With the shell emission peaking at $\tau_\nu \sim 1$, the omission of this effect will only affect the normalization of the overall spectrum. Also, when calculating the emission, the optical depths of the neighbouring shells are not taken into account. Therefore to minimize the impact of these factors, only jets at relatively large angle of sight from the viewer are modelled.

2.3.6 Model parameters

So far, only some of the key physics and the principles behind the model have been outlined. It is therefore important to list some of the parameters used in our model to see how they influence the physical properties of a jet. Appendix C contains the list of all the model parameters.

The internal energy of the shell is split between the electron kinetic energy (u_e), the shell thermal energy (u_{th})and the magnetic energy(u_B) i.e.

$$E_{int} = u_e + u_{th} + u_B \ . \tag{2.50}$$

With no obvious data available on how such energy may be split, equipartition between the electron kinetic and magnetic energy is assumed. It is possible to constrain the distance to the source (D) and the jet viewing angle (θ) from observations. The shell mass on the other hand is a free parameter. In the case of a massive ejection event, the mass can be set manually. For a continuous jet (multiple ejections), we have a choice of setting the individual shell's properties manually or sampling from a pseudo-random distribution of these parameters. In the pseudo-random case, if the jet kinetic luminosity, L_W, is known then it can be used to generate the shell

mass values by using:

$$\sum_{j=1}^{N} M_j \Gamma_j c^2 = L_W t_{jet} \ , \tag{2.51}$$

where t_{jet} is the duration the jet is "on". Therefore the total relativistic mass of all the shells present in the jet has to correspond to the kinetic luminosity of the jet being modelled. The time gap, $\mathrm{d}t_{inj}$, between any two shells can also be set either manually or sampled from a Gaussian distribution with a given mean and standard deviation. This time gap and equation 2.51 determine how massive a shell can be:

$$M_j = \frac{L_W \mathrm{d}t_{inj}}{\Gamma_j c^2} \ , \tag{2.52}$$

that is, a larger time gap means a more massive shell.

The shell bulk Lorentz factor (Γ), if not set manually, is picked from a random distribution of values with the maximum and the minimum values ($\Gamma_{max}, \Gamma_{min}$) set by the user; the bulk Lorentz factor for a shell does not vary as it moves through the jet, unless it is involved in a collision. The shell length ($\mathrm{d}l$) and the jet opening angle (φ) can also be set by the user. For the shell length, attempting to achieve a continuous jet approximation results in the following relation:

$$\mathrm{d}l = l_{scale} \ dt_{inj} \ \beta_{shell} c \ , \tag{2.53}$$

where l_{scale} is a scaling factor with a maximum of unity. $l_{scale} = 1$ means no spatial gap between two consecutively injected shells; in the simulation, however, l_{scale} is set < 1 in order to avoid a "pile-up" of shells at the source.

When it comes to the power-law electrons, the power-law index (p) is set at 2.1 while the Lorentz factor limits ($\gamma_{min}, \gamma_{max}$) are set at 1 and 10^6 respectively; γ_{min} is kept constant at unity, whilst γ_{max} is allowed to vary due to energy losses.

The data from the simulation are in the form of flux corresponding to the frequencies being *observed*. The observed frequency range is logarithmic with the user setting the minimum and the maximum frequency, plus the number of bins for the range. The data are written at every time step, where the time step is defined as an "event". The event refers to either a shell injection or a merger: the time step tends to be less than $\mathrm{d}t_{inj}$, if the mergers are also taking place. However, if one wishes, the time resolution can be increased manually and set to a desired time step.

2.4 Demonstrating some of the model capabilities

The following section illustrates some of the *i*Shocks capabilities. The simplest scenarios are used to demonstrate how the model produces self consistent and accurate results: the more

complex scenarios are presented in chapters 3 and 4.

2.4.1 Single ejection

A single shell ejection scenario may be used to simulate the massive ejection events observed in X-ray binaries, in the form of radio flares, when the source is transitioning from a hard state to a soft state (Fender *et al.*, 2004) (discussed further in section 3.3). When shells are injected into the jet, they only start emitting radiation, or "light-up", when they have been involved in a collision i.e. the shock front has passed through and energized the plasma within the shell (unless they are injected with some internal energy). In the case of a single shell, however, no collisions can take place; thus, the shell will require artificial lighting-up. This is achieved by creating a *shock-zone* at an arbitrary point, x_{shock}, along the jet; the *shock-zone* picture is reminiscent of the jet models involving a single shock-zone in the jet (see Falcke, 1996, Falcke and Markoff, 2000, Markoff *et al.*, 2001, Markoff *et al.*, 2003, Pe'er and Casella, 2009 and the references therein). In our model, once a shell passes through the shock zone it is energized instantly. A fraction of the shell's relativistic energy, E_{frac}, is used as scaling for the amount of internal energy given to a shell after energization; the shell velocity, Γ, and the mass, M, remain unchanged.

2.4.1.1 Without energy losses

Not taking the shell energy losses into account, as it expands, is similar to assuming that any energy losses are continually replenished. With this kind of a set up, a shell is allowed to propagate down the jet and expand laterally. The shell's longitudinal expansion due to the thermal energy of plasma is suppressed: the thermal energy is set to zero. The change in volume is therefore not associated with any work done by the shell.

The emission from a single shell at radio and infra-red frequencies is shown in figure 2.8. The plot also shows how the shell optical depth for the two frequencies changes as the shell moves down the jet. The increase in the shell volume causes it to become more optically thin to lower frequencies. This behaviour is evident in the figure, as the radio emission peak is much further down the jet, compared to the infra-red peak: the emission peaks at $\tau_\nu \approx 1$. Various shell and jet volume parameters are outlined in table 2.1.

The radio and the infra-red lightcurves, in figure 2.9, illustrate how the radio rise time is much longer than that of the infra-red. These rise times are determined by the shell energy density, and how quickly this energy density changes with the change in volume. Therefore in the case shown here, the shell properties are such that the infra-red peaks soon after injection, but the radio takes much longer. It should be noted that because the energy losses are not considered here, only the energy density of the shell is decreasing due to the lateral expansion; the shell's total energy content remains constant.

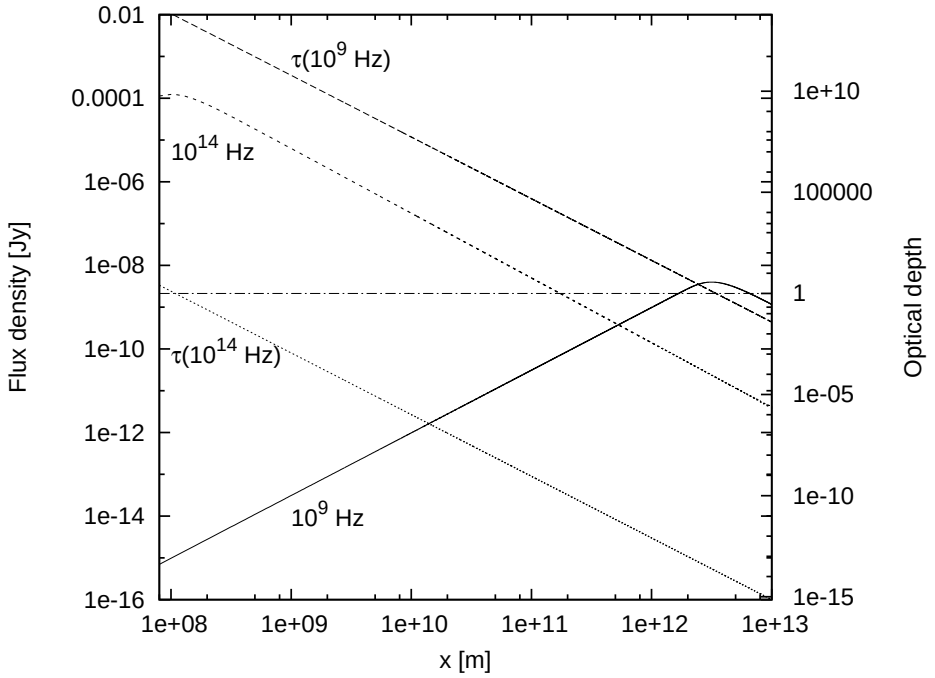

Figure 2.8: Emission from a single shell: radio and infra-red frequencies are shown. The shell optical depth, τ_ν, is also shown; the horizontal line marks optical depth of unity.

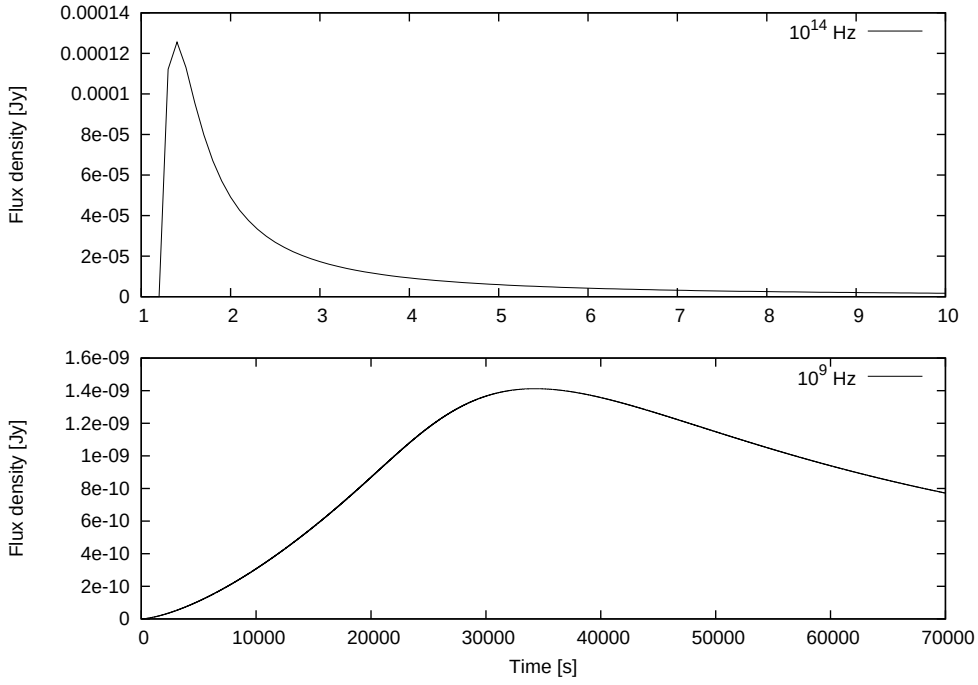

Figure 2.9: Infra-red and radio lightcurves for a single shell without adiabatic energy losses.

Table 2.1: The parameters used for single ejection scenarios.

Parameter	fig 2.8, 2.9	fig 2.10, 2.11
φ	5^o	5^o
θ	40^o	40^o
D	2 kpc	2 kpc
M	1×10^7 kg	1×10^7 kg
Γ	2.0	2.0
dl	1×10^4 m	1×10^4 m
u_e	0.5	0.5
u_B	0.5	0.5
u_{th}	0.0	0.0
x_{shock}	0.2 ls	0.2 ls
E_{frac}	0.3	0.3
Sim. Duration	7×10^4 s	500 s

2.4.1.2 With adiabatic energy losses

When the adiabatic energy losses are taken into account, an increase in the shell volume causes a decrease in the shell internal energy. In this particular simulation, as in the previous scenario, the shell thermal energy is again set to zero. Therefore any increase in the shell volume is purely due to the lateral expansion of the jet.

The radio and infra-red emission from a single shell, with the adiabatic energy losses taken into account, are shown in figure 2.10. When compared with the emission with no energy losses, figure 2.8, two main differences become apparent: the radio peak is at much lower flux value, and at much smaller distance along the jet. The infra-red peak flux values, however, remain relatively unchanged; the peak occurs at smaller radii when compared to the case with no energy losses. These differences can be explained when one looks at how the shell energy density changes with and without the energy losses present.

The shell's optical depth is a function of the shell's energy density; that is, a shell becomes optically thin to lower frequencies as the energy density drops. When energy losses are not considered, the change in the shell volume solely effects the change in the energy density. However, when the adiabatic energy losses are taken into account, the energy losses along with an increase in the shell volume drive the change in the shell energy density. In such a scenario, there is a two fold effect on the shell energy density: increase in the shell volume and the decrease in the shell internal energy. This means that the shell optical depth, for a given frequency, changes more rapidly than when only the volume is effecting the change. However, the emission intensity is also affected by the energy losses. With the adiabatic energy losses active a shell may be able to peak, for example, in radio frequencies at smaller jet radii, x, but the peak intensity is lower due to the energy losses suffered by the emitting electrons and the magnetic field. If the longitudinal expansion is also taken into account then the energy losses are accelerated and a shell is able to peak in radio frequencies even earlier with a further

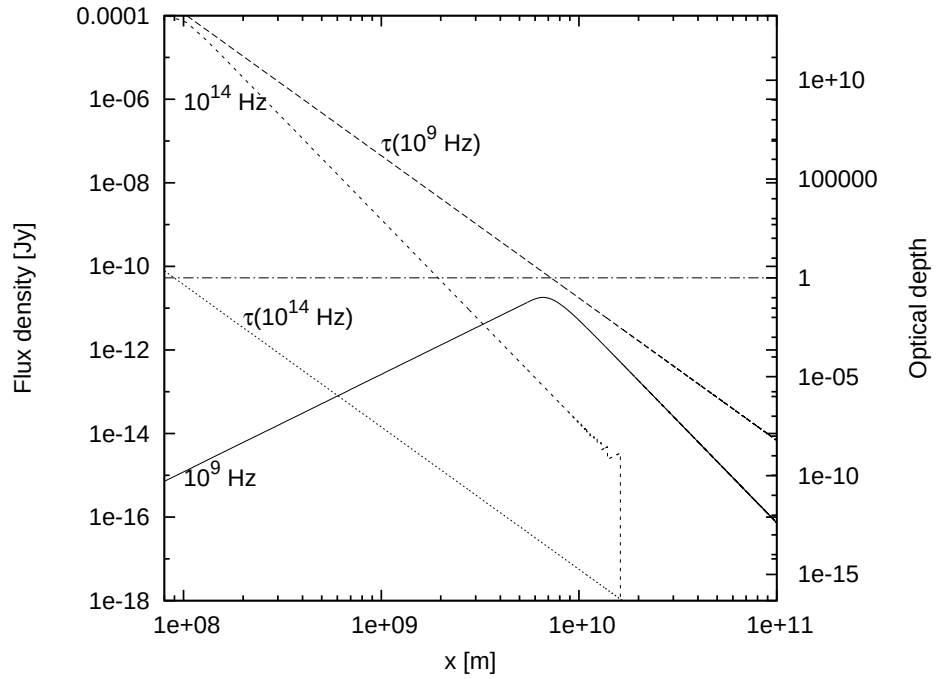

Figure 2.10: Emission from a single shell with adiabatic energy losses: radio and infra-red frequencies are shown. The shell optical depth, τ_ν, is also shown; the horizontal line marks the optical depth of unity.

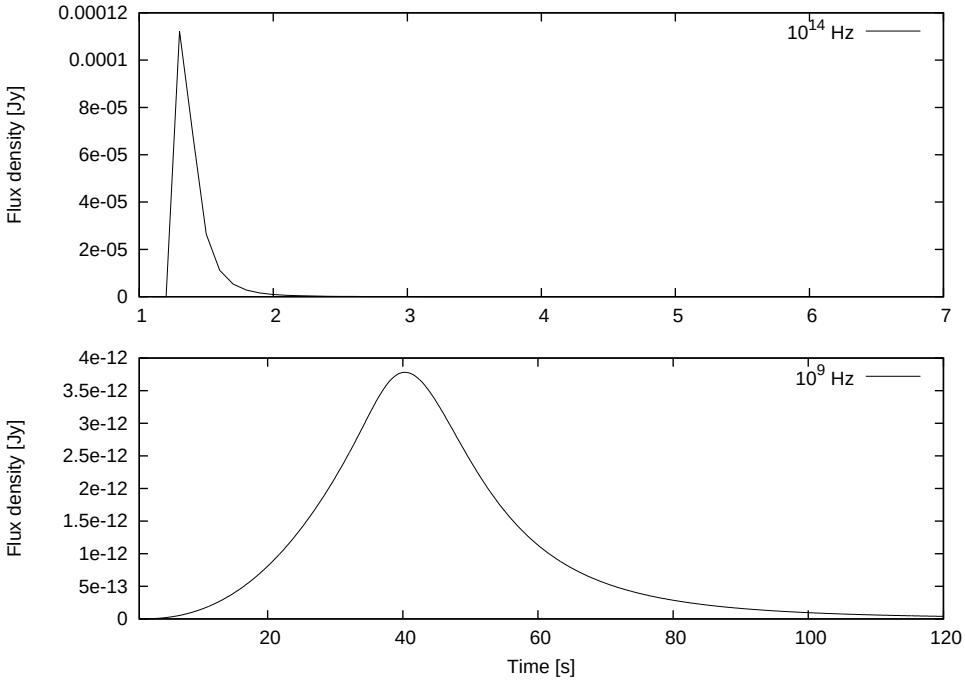

Figure 2.11: Infra-red and radio lightcurves for a single shell with adiabatic energy losses.

Table 2.2: The properties of the two shells injected in the double-ejection scenario shown in figures 2.12, 2.13, 2.14and 2.15

Parameter	shell 1	shell 2
Inj. time	1 s	10 s
Mass	1×10^6 kg	1×10^{10} kg
Γ	2.0	3.0
dl	1×10^5 m	1×10^7 m

decrease in flux values. This can be seen in figure 2.10, and 2.11, where the peak radio flux is nearly two orders of magnitude lower when compared with the peak radio flux in figure 2.8. The infra-red peak flux on the other hand has a relatively small change. This is due to the shell becoming optically thin to the IR frequency very quickly in both cases, thus not having the time to suffer much energy loss. When the adiabatic losses are active, the shell starts off optically thin to IR. This is because the relative change in volume from the moment of injection to the subsequent time step being sufficient to drop the shell energy density below the limit for the shell becoming optically thin to the infra-red frequencies. The initial volume of a shell, in addition to the relative change in volume, also plays a part in how quickly that shell becomes optically thin to a given frequency: a large enough shell could start off as optically thin to the infra-red frequencies. The sharp cut off for the infra-red flux, in figure 4, is due to γ_{max} dropping below the energy threshold for the power-law electrons to emit in the infra-red.

2.4.2 Double ejection

A double ejection scenario involves two shells being injected into the jet volume with a time interval, dt_{inj}, between them. If the second shell, j, has a higher velocity than the preceding shell, $j-1$, then the two shells will eventually collide. This scenario also demonstrates the core principle of multiple ejections: a large number of two-shell collisions taking place all along the jet to give rise to multiple shocks.

The shock-zone location, mentioned in the previous scenario, is set at zero. This means that the shells are injected with finite internal energy instead of gaining it after passing through an arbitrary point. The adiabatic energy losses are also modelled, but only due to the lateral expansion of the jet; the shell thermal energy is set to null.

The properties of the two shells injected into the jet volume are outlined in table 2.2. The first shell, $(j-1)$, is not only less massive than the following one, j, but also larger. The combination of these parameters means that shell $(j-1)$ becomes optically thin to lower frequencies sooner than shell (j). This can be seen in figures 2.12 and 2.13 where the radio peak for shell $(j-1)$ is at much smaller jet radii than that for shell j; in the case of IR emission, shell $(j-1)$ is already optically thin at those frequencies, when it is injected, while shell j reaches the peak IR flux later. The figures also show the point where the two-shell collision, or the merger, takes place: it is marked by a sharp increase in both the radio and the IR emissions.

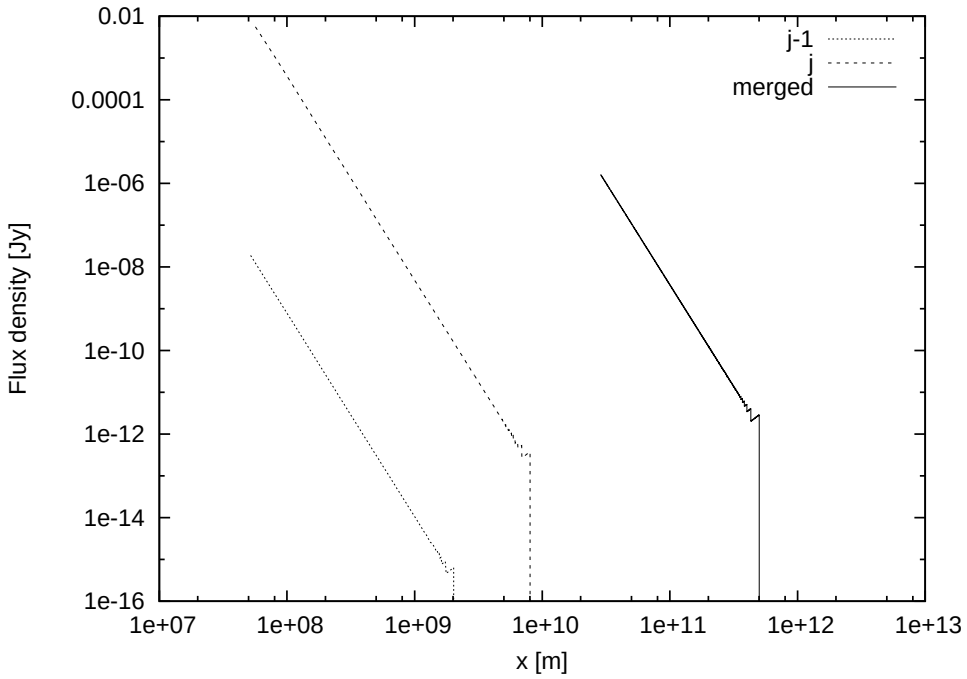

Figure 2.12: The infra-red (1×10^{14} Hz) emission from the two injected shells that later on merge (at $\sim$100s) to become a single shell. The properties of the two injected shells are outlined in table 2.2 while the simulation parameters are outlined in table 2.3. Adiabatic energy losses due to lateral expansion only are being modelled.

.

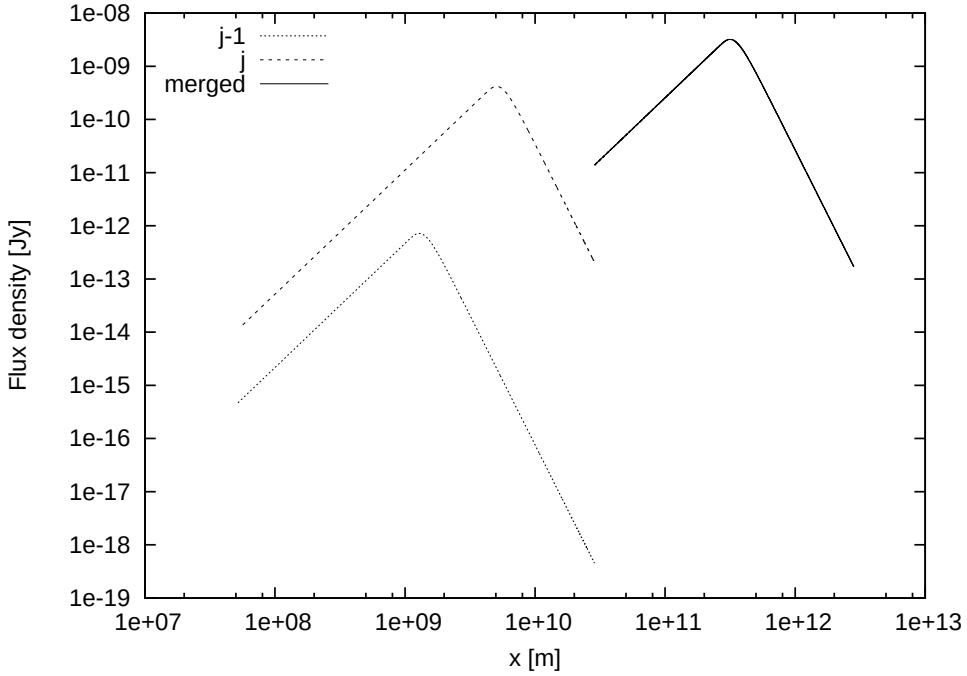

Figure 2.13: The radio (1×10^{9} Hz) emission from the two shells injected that later on merge (at $\sim$100s) to become a single shell. The properties of the two shells are outlined in table 2.2 while the simulation parameters are outlined in table 2.3. Adiabatic energy losses due to lateral expansion only are being modelled.

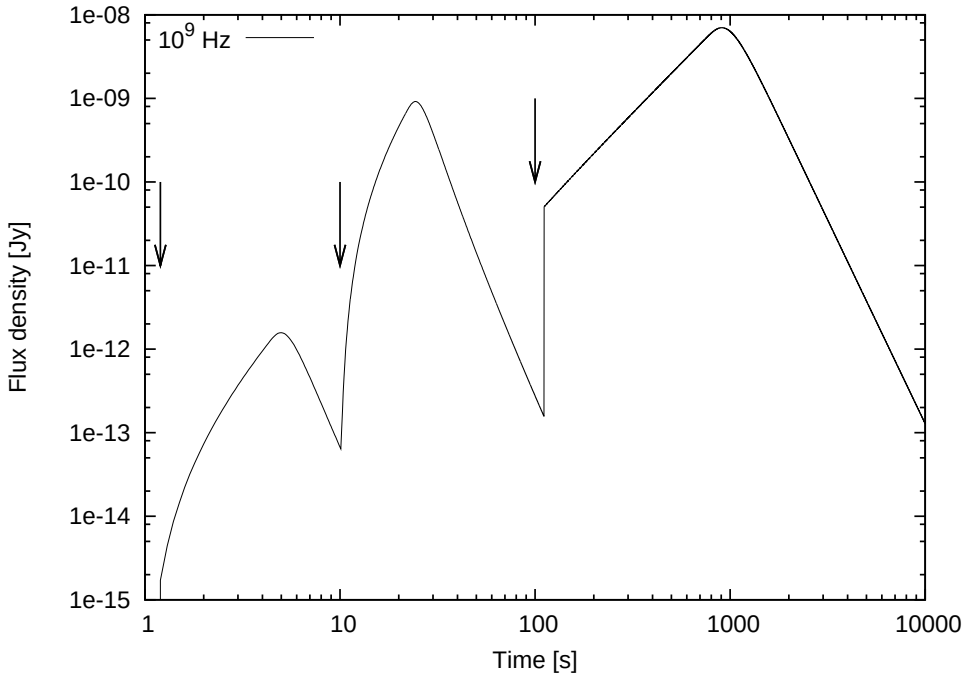

Figure 2.14: The lightcurve for the radio emission. The two arrows on the left signify injection of the two shells; the third arrow shows the time of merger. Initially (after the second shell injection at 10s) the lightcurve comprises emission from both the shells; later, after merger at $\sim$ 100s, only a single shell exists in the jet. The properties of the two shells are outlined in table 2.2; the simulation parameters are outlined in table 2.3. The unusual *log*(time) is used for demonstrative purposes.

Table 2.3: The parameters used for double-ejection scenario.

Parameter	Figures 2.12, 2.13, 2.14 and 2.15
φ	5^o
θ	40^o
D	2 kpc
u_e	0.5
u_B	0.5
u_{th}	0.0
x_{shock}	0.1 ls
E_{frac}	0.2
Sim. Duration	1×10^4 s

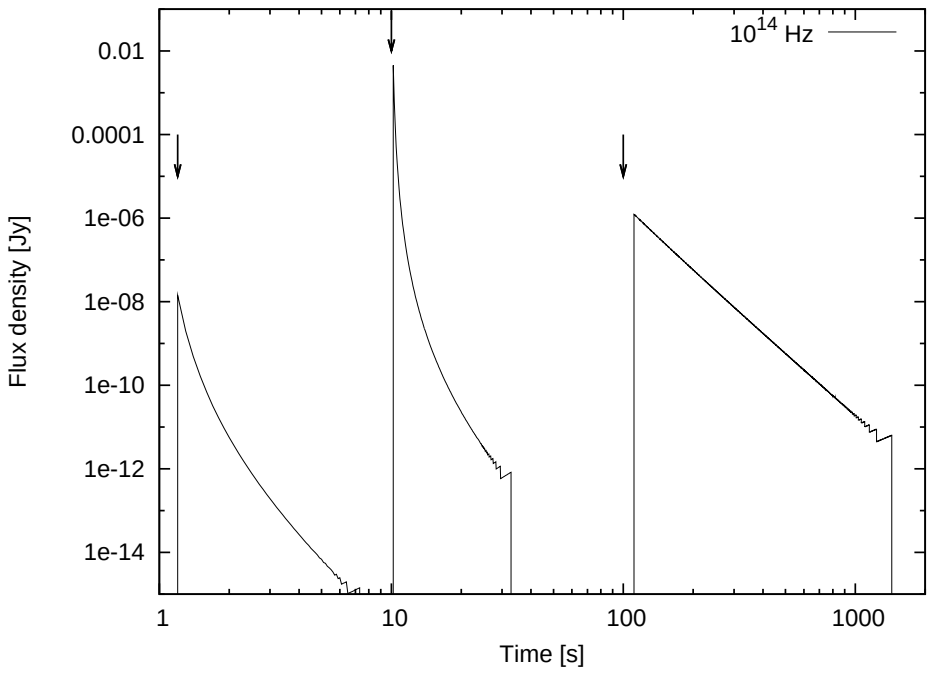

Figure 2.15: The lightcurve for the infra-red emission. The two arrows on the left signify injection of the two shells; the third arrow shows the time of merger. Initially (after the second shell injection at 10s) the lightcurve comprises emission from both the shells; later, after merger at $\sim$ 100s, only a single shell exists in the jet. The properties of the two shells are outlined in table 2.2; the simulation parameters are outlined in table 2.3. The unusual *log*(time) is used for demonstrative purposes.

The infra-red emission had in fact faded away completely by the time the merger took place, thus demonstrating the re-energization aspect of these collisions/internal shocks.

The light curves shown in figures 2.14 and 2.15 illustrate the lag between the high and the low frequency peaks, already seen from the individual shells scenario. In this case, however, the light curves show the total emission from the entire jet (only two shells for this scenario; the multiple shells case is presented in the following chapter). The radio emission not only lags behind the infra-red emission, but also has a much lower peak flux value, due to the energy losses. Also, the radio emission rise and decay times are much longer than those corresponding to the infra-red. For the infra-red, there is a sharp rise in the emission at the point of shell merger. As mentioned earlier, the infra-red fades away almost completely by the time the shell collision takes place. The merger, however, has a compression effect, thus increasing the energy density of the newly formed shell, causing it to start emitting in the infra-red. The internal energy generated at the collision is still not sufficient to make the shell optically thick to infra-red; therefore we do not see a slow rise in the infra-red flux from the merged shell. The picture is slightly different for the radio: the merged shell has high enough energy density that it becomes optically thick to the radio frequencies, leading to a slow rise in the flux. The other point to note, for the radio emission, is that after the second shell is injected into the jet there is a delay before the maximum flux value is reached. This is due to the delay in the second shell becoming optically thin to the radio frequency.

2.5 Conclusions

The focus of this chapter has been to provide the details of the internal shocks model, *i*Shocks. The chapter also outlines some of the other models around and how certain questions have remained unanswered. The *i*Shocks model's first aim is to address the energy replenishment problem for the adiabatic jets, discussed in the proceeding chapter. However, before delving into these complex scenarios, some simple setups were used to demonstrate how the model works: the single and the double ejection scenarios are a greatly simplified picture of what would be taking place inside a multiple ejections jet. The results presented in this chapter show how the emission processes and the mergers are calculated self-consistently. These scenarios have also outlined how when the adiabatic energy losses are considered, the spectrum would become highly inverted.

3

From the flat spectrum to the flares

The following chapter delves a little further into the X-ray binary jet behaviour and how the *i*Shocks model can be used to model observations. There is a particular focus on two aspects of an X-ray binary jet: the flat spectrum and the flaring behaviour. It should be noted that these two behaviours are generally considered to be associated with very different states of the system.

3.1 The Flat Spectrum

The basics of the flat spectrum and how it is possible to obtain such a spectrum from the superposition of multiple self-absorbed synchrotron spectra were outlined in section 2.1. Various other models outlined in the previous chapter were in response to the observations of flat spectra in compact radio cores of AGN.

The spectrum at the radio frequencies for X-ray binaries is generally flat or inverted ($\alpha \geq 0$) when observed in the low/hard state. This flat spectrum component has been seen to extend up to mm (Fender *et al.*, 2000, 2001) and even the infrared (Chaty *et al.*, 2003; Kalemci *et al.*, 2005; Migliari *et al.*, 2007). By analogy to the jet signature in the compact radio cores of AGN (Blandford and Königl, 1979; Hjellming and Johnston, 1988; Falcke and Biermann, 1999), this flat spectrum is also considered to be the signature emission from the jet in X-ray binaries. One would be inclined to believe that with such extensive use and history of the flat spectrum, its origin would be well understood. Unfortunately, this is not the case. A variety of models, outlined in the previous chapter, have been suggested, but none can provide a satisfactory answer nor reproduce the canonical flat spectrum with the adiabatic energy losses active.

Table 3.1: The parameters used to demonstrate multiple ejections (without energy losses).

Parameter	Figures 3.1, 3.2, 3.3, 3.4
φ	5^o
θ	40^o
D	2 kpc
L_W	1×10^{30} J/s
Γ	2.0
l_{scale}	0.2
u_e	0.5
u_B	0.5
u_{th}	0.0
x_{shock}	0.0 ls
E_{frac}	0.01
dt_{inj}	$\approx$1 s
Sim. Duration	5×10^4 s

Using our *i*Shocks model, we reproduce, for the first time, a flat/inverted spectrum (over a large frequency range) and provide one possible solution to the re-acceleration conundrum.

3.2 Modelling the flat spectrum with *i*Shocks

The *i*Shocks model is used to simulate a hard state jet. With the discretization of the jet, multiple shell ejections are required to simulate a continuous jet.

3.2.1 Multiple ejections

The relatively simple single and double ejection scenarios were shown in the previous chapter. Here, the multiple ejections set-up is demonstrated with and without the adiabatic energy losses. When the energy losses are absent, internal shocks/collisions are also omitted, because no energy replenishment is required; On the other hand, the collisions are modelled when the energy losses are incorporated. When the collisions are active, the shell properties are sampled from a pseudo-random distribution (as described in section 2.3.6).

3.2.1.1 Without energy losses

If the time gap between ejections is kept small, then an almost continuous jet can be approximated by the multiple ejections. All the shells here are injected with the same properties (time gap, velocity etc.), hence no collisions take place. The simulation parameters are given in table 3.1.

The spectrum in figure 3.1 shows how a flat spectrum (for a specific frequency range) can be recovered when no energy losses are considered. This set up can be compared to a situation where one assumes a constant replenishment of any energy losses by an unknown mechanism

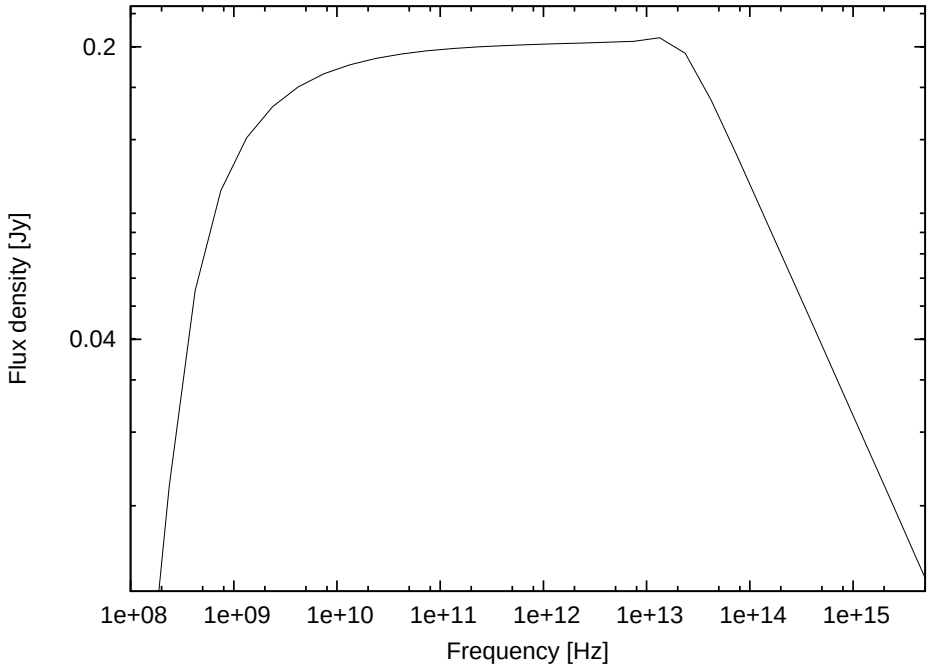

Figure 3.1: Spectrum of a jet modelled using multiple ejections (without energy losses). An almost flat spectrum is achieved over a large frequency range. It should be noted that the low frequency turn over point is dictated by the duration of the simulation: longer simulation means a longer jet which means a lower frequency turnover. (see table 3.1 for parameters).

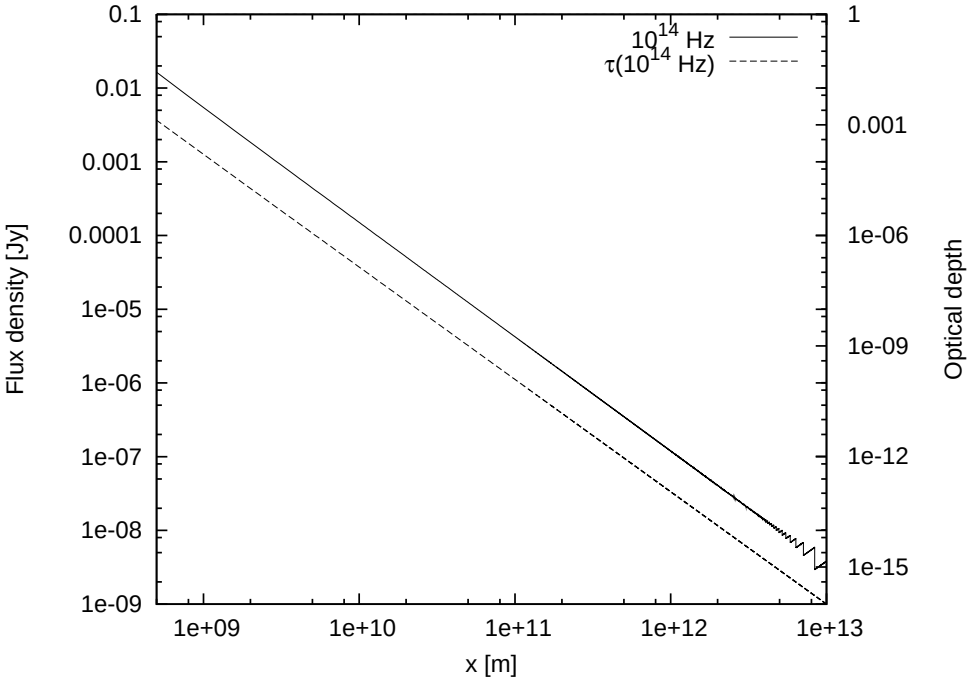

Figure 3.2: The infra-red emission of a multiple ejections jet (without energy losses). Optical depth corresponding to the infra-red frequency is also plotted (long dashed line). The wriggles at the end of the IR spectrum are a numerical artefact.(see table 3.1 for parameters).

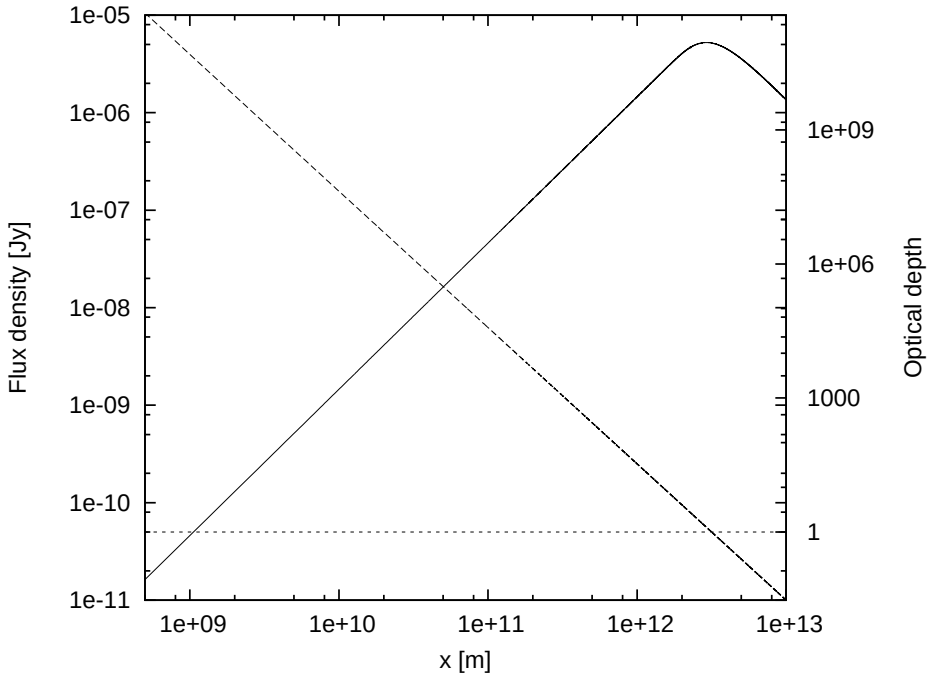

Figure 3.3: The radio emission of a multiple ejections jet (without energy losses). Optical depth corresponding to the radio frequency is also plotted (long dashed line); short dashed line shows where the optical depth ≈ 1.(see table 3.1 for parameters).

(Blandford and Königl, 1979). The evolution of a radio and an IR frequency along the jet can be seen in figures 3.2 and 3.3 respectively. The two frequencies show very different behaviours: the IR spectrum shows a constant decline while the radio spectrum peaks much further down the jet. A look at the optical depths for the two frequencies shows that the injected shells, and ultimately the jet, is optically thin to the infrared ($\tau_\nu << 1$). For the radio frequency the jet becomes optically thin at a large distance from the source. (The same behaviour was observed with single ejections as well.) The emission for a range of frequencies (radio $< \nu <$ infra-red) is shown in figure 3.4. The different emissions shown in figure 3.4 follow the $R_{\tau\approx 1} \propto \nu^{-1}$ relation [as shown analytically by Blandford and Königl (1979)].

3.2.1.2 With adiabatic energy losses

Internal shocks are a possible way to address the problem of replenishing the energy losses in a jet. In the simulations presented below, the shells are expanding both longitudinally and laterally; therefore the adiabatic losses can be extremely fast, making the flat spectrum difficult to obtain. The spectra from the simulations where shells are not injected with any internal energy can also be compared with those where the shells are injected with internal energy: internal shocks are the only source of the internal energy production in the former case, whereas in the latter they serve to replenish the energy losses.

Figure 3.5 shows a highly inverted spectrum, when the shells are not injected with any internal energy. The internal shocks taking place are not sufficient to produce the internal energy in addition to replenishing the energy losses that are taking place.

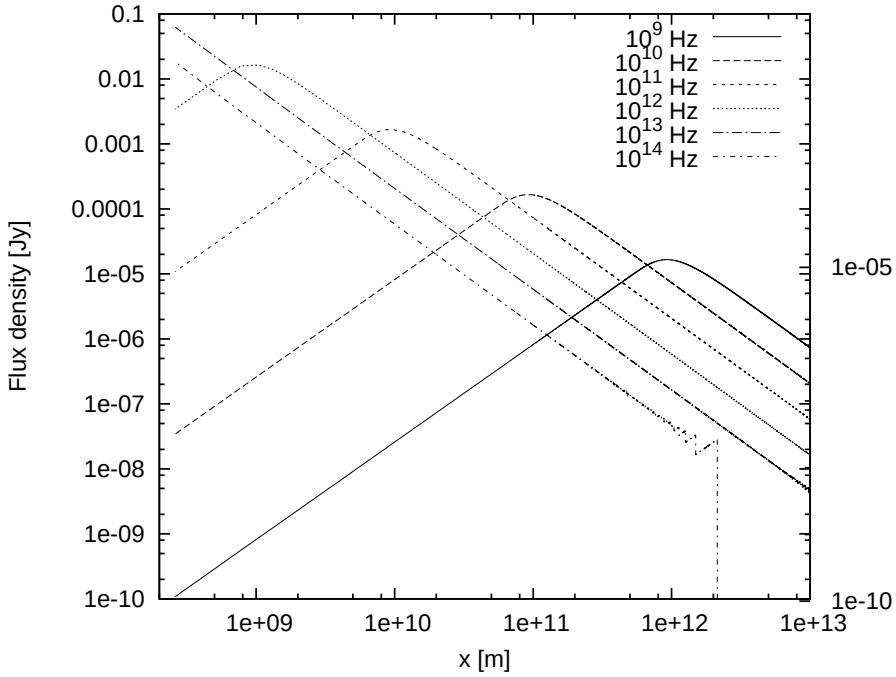

Figure 3.4: The emission as a function of the jet radius for a range of frequencies in a multiple ejections jet (without energy losses). (see table 3.1 for parameters).

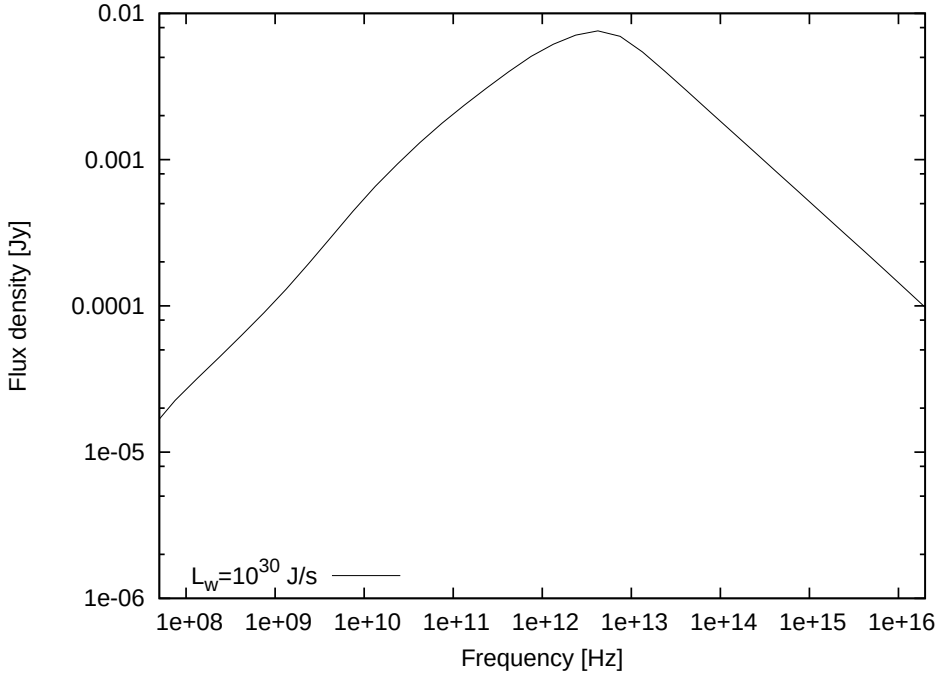

Figure 3.5: Time averaged spectrum ($\approx$1 ks) from a multiple ejection jet with adiabatic energy losses. The shells involved undergo lateral and longitudinal expansion. The shells are not injected with any internal energy. (see table 3.2 for parameters).

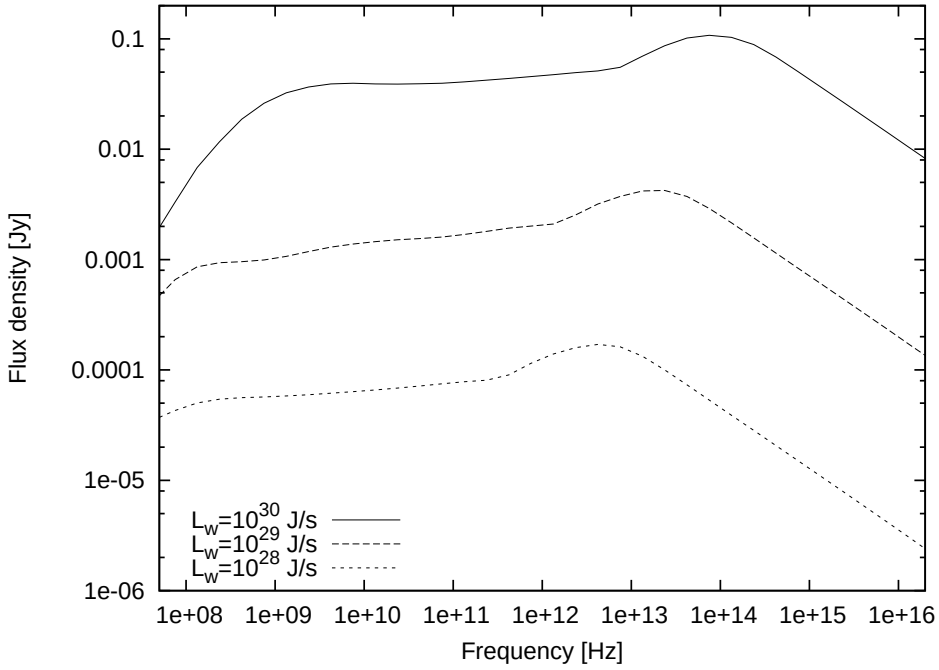

Figure 3.6: Time averaged inverted/flat spectra (≈2 ks) from multiple ejection jets with the adiabatic energy losses. The three spectra correspond to different jet kinetic luminosities. The shells involved undergo lateral and longitudinal expansion. The shells are injected with internal energy, creating a much different spectrum from seen in figure 3.5.(see table 3.2 for parameters).

Table 3.2: The parameters used for multiple ejections jet with adiabatic energy losses.

Parameter	fig 3.5	fig 3.6
φ	5^o	5^o
θ	40^o	40^o
D	2 kpc	2 kpc
L_W	1×10^{30} J/s	$1 \times 10^{28-30}$ J/s
Γ_{min}	1.5	1.5
Γ_{max}	2.0	2.0
l_{scale}	0.2	0.2
u_e	0.33	0.33
u_B	0.33	0.33
u_{th}	0.33	0.33
E_{frac}	0.0	0.01
dt_{inj}	≈1 s	≈1 s
Sim. Duration	5×10^4 s	5×10^4 s

On the other hand, the spectra given in figure 3.6 illustrate how it is possible to obtain flat/inverted spectra even with adiabatic energy losses taking place. In order to achieve this, it is necessary to inject the shells with some internal energy. In other words, when the internal shocks are used to produce the internal energy, plus replenish the adiabatic losses, a flat spectrum cannot be obtained; however, when the internal shocks are used for the energy replenishment only, the flat/inverted spectrum is recovered. The injection with the internal energy is not that far from the "real" picture because one would expect the jet plasma to be emitting from the moment it is ejected into the jet. However, the internal energy scaling does lead to a free parameter in the simulation and worth constraining.

We can also note in figure 3.6 that the flux is correlated with the jet kinetic luminosity. This is because E_{frac} is scaled according to the relativistic energy of the shell, which is related to the mass and the bulk Lorentz factor of the shell; the mass is dependent on the kinetic luminosity (see equation 2.51), which ultimately means that a higher jet kinetic luminosity creates shells with higher internal energy, thus producing greater flux. The higher energy density also means that a shell would be optically thick to higher frequencies. The effects of the jet kinetic luminosity on the flux (and the spectrum) are degenerate with E_{frac} parameter: a lower luminosity jet, but with higher a E_{frac} value can produce similar results. This degeneracy extends to any parameter that influences the internal energy of a shell at injection; for instance, the jet opening angle and the shell length (l_{scale}) will also influence the form of the spectra obtained. The spectra show in figure 3.6 conform approximately to the relation: $F_\nu \propto L_{\rm W}^{\approx 1.4}$. This is in agreement with the relation found analytically by Falcke and Biermann (1995); Heinz and Sunyaev (2003), stating: $F_\nu \propto L_{\rm W}^{\approx 1.4}$.

The flat/inverted spectra produced have shown other interesting correlations: both the high and the low frequency turnover points in the spectrum correspond to certain jet properties. The high frequency shifts to higher frequencies with an increase in the jet power (mainly $L_{\rm W}$, but also E_{frac}). The high frequency break scales approximately as: $\nu_b \propto L_{\rm W}^{\approx 0.6}$, which is remarkably close to previously observed and calculated relation of $\nu_b \propto L_{\rm W}^{\approx 0.7}$ (Falcke and Biermann, 1995; Markoff *et al.*, 2003; Heinz and Sunyaev, 2003). The low frequency turnover, on the other hand, is also affected by the jet luminosity, but the re-energization by the internal shocks appears to play the biggest role: both the number of shells present in the jet and the collision radii of the shells influence the low frequency turnover.

3.2.2 Impact of approximations the flat spectrum

Section 2.3.4 showed how the approximations for various internal shock quantities differ from the exact calculations. Here, we can see what, if any, impact these approximations have on a flat spectrum. The spectra presented in figure 3.7 show a comparison of how the flat spectra differ depending on whether we are using the exact solution (section 2.3.4) or the approximation for the merger Lorentz factor. (The simulation parameters are identical to those used for figure 3.6 when the jet luminosity is 10^{30} J/s.) The "exact" also includes the correction for the missing Lorentz factors in the internal energy formula. We can see that the corrections do not change

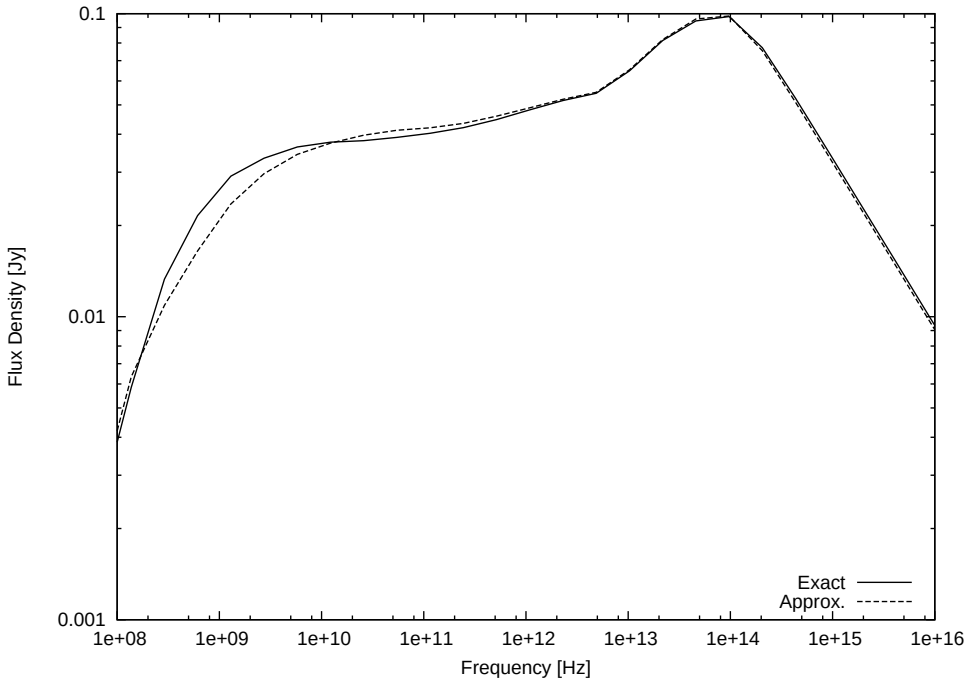

Figure 3.7: The plot shows a comparison of the flat spectra obtained whether using exact solutions outlined above or the approximations.

the spectrum drastically and in fact help obtain a flatter spectrum at lower frequencies. This is because the corrections have improved the collision efficiencies. However, it is worth noting that the parameter E_{frac}, the internal energy which the shells are injected with, is comparable to the amount of internal energy generated in the mergers (for the Γ range of 1.5-2). The parameter E_{frac} therefore requires attention. In other words, if possible, the dependence on E_{frac} needs to be minimized. This minimization may be a scenario where E_{frac} is much lower than the internal shocks efficiencies.

3.3 Flares in X-ray binaries

By contrast to the continuous jets modelled in the previous section, radio flares represent a very sporadic jet. There are several examples of the radio flaring/oscillations and repeated ejections behaviour in X-ray binaries (Hjellming and Rupen, 1995; Hjellming *et al.*, 1999; Pooley and Fender, 1997; Fender and Pooley, 2000; Fender *et al.*, 2009, plus more). Radio flares are usually single events associated with a state transition from the hard state to the soft state. This is supported by the position of these flares on the hardness-intensity diagrams (Fender *et al.*, 2009). In the case of the source GRS 1915+105, however, repeated large ejections or radio flares have been observed. A specific episode, shown in Fender and Pooley (2000), is of particular interest because simultaneous mm and infra-red observations exist. The following section aims to model these observations.

3.3.1 GRS 1915+105 observations

GRS 1915+105 is one the most widely studied of all the microquasars. Some of the reasons for this include its high luminosity and variability behaviour (Mirabel and Rodríguez, 1994). The source is considered to be at a distance of $\approx$ 11kpc (Rodriguez *et al.*, 1995; Zdziarski *et al.*, 2005), powered by a $\approx 14 M_{\odot}$ black hole (Greiner *et al.*, 2001) and at an inclination angle of $\approx 70^{\circ}$ (Mirabel and Rodríguez, 1994; Fender *et al.*, 1999). Eikenberry *et al.* (1998) observed a correlation between the X-ray and the infra-red events. This multi-wavelength connection was extended further by Mirabel *et al.* (1998), when they observed the source simultaneously in the X-ray, the infra-red and the radio.

The observations outlined in Fender and Pooley (2000) were carried out using the United Kingdom Infrared Telescope (UKIRT) and the James Clerk Maxwell Telescope (JCMT). The IRCAM3 instrument on UKIRT was used for the 2.2 μm observations while the SCUBA instrument on JCMT was used for the 1350 μm observations. The quasi-simultaneous (a few days before and after the UKIRT/JCMT observations) radio (15 GHz) observations from the Ryle telescope were also used.

Fender and Pooley (2000) results show no discernible delay (with an upper limit of $\approx$ 4 min) in the rise times for the infra-red and the millimetre observations; the radio observations were not simultaneous, hence such comparison is not possible. The JCMT observation show a series of mm wavelength oscillations with a quasi-period of $\approx$ 23 min. Figures 3.8, 3.9 and 3.10 show some of the simultaneous mm-IR data, plus the radio data distribution, obtained by Fender and Pooley (2000).

3.3.2 Modelling the flares in GRS 1915+105

Different *i*Shocks model set ups were used to model the mm-IR-Radio flares shown in figures 3.8, 3.9 and 3.10. The results presented below are split according to the set up being explored.

3.3.2.1 Regular interval: without mergers

The simplest attempt at modelling these flares involves a regular and uniform dt_{inj} between the shell injections. All the shell properties are identical, including the Γ value; hence, no collisions taking place. The injection time gap was set at $\approx$1400 s, based on the periodicity of $\approx$23 min in the observations shown in figure 3.9.

The results of $\approx$1400s ejection interval are shown in figures 3.11 and 3.12; the corresponding parameters are outlined in table 3.3. The first thing to note is the periodicity of $\approx$23 min is achieved, as expected, for the various observing frequencies. The flux rise times are different for the different frequencies: the lower frequency takes longer to reach peak flux value. The infra-red peaks do not have a slow rise. Instead, the IR peaks rise instantaneously and then decay over the $\approx$23 min interval. This difference in the rise and decay times is due to the initial shell conditions: the shell size and the energy density mean that each shell is already optically thin to the infra-red, hence no slow rise occurs. Increasing the E_{frac} or reducing the l_{scale} would

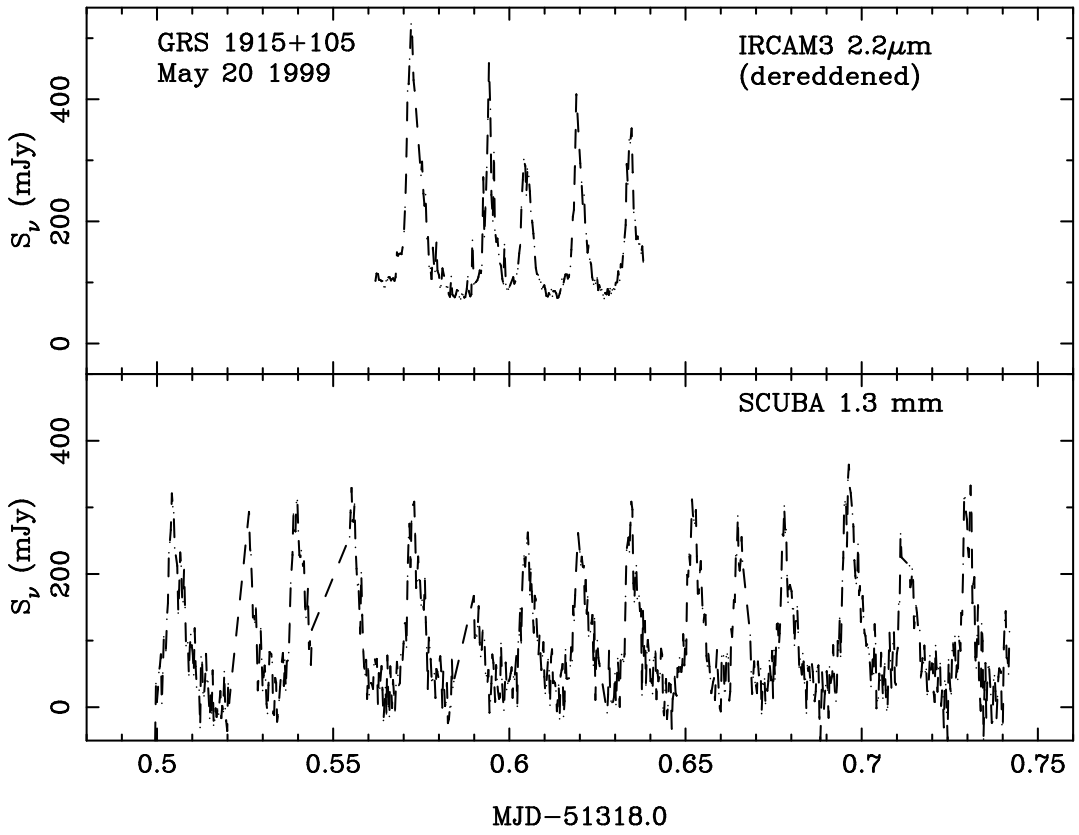

Figure 3.8: IRCAM and SCUBA observations of the flaring events in GRS 1915+105. The image is from Fender and Pooley (2000)

Table 3.3: The parameters used to model GRS 1915+105 flares with regular injection interval and without mergers.

Parameter	Figures 3.11, 3.12
φ	5^o
θ	70^o
D	11 kpc
L_W	1×10^{31} J/s
Γ	2.0
l_{scale}	0.3
u_e	0.5
u_B	0.5
u_{th}	0.0
x_{shock}	0.0 ls
E_{frac}	0.15
dt_{inj}	$\approx$1400 s
Simulation Duration	$\approx 3.5 \times 10^4$ s
Adiabatic Losses	yes

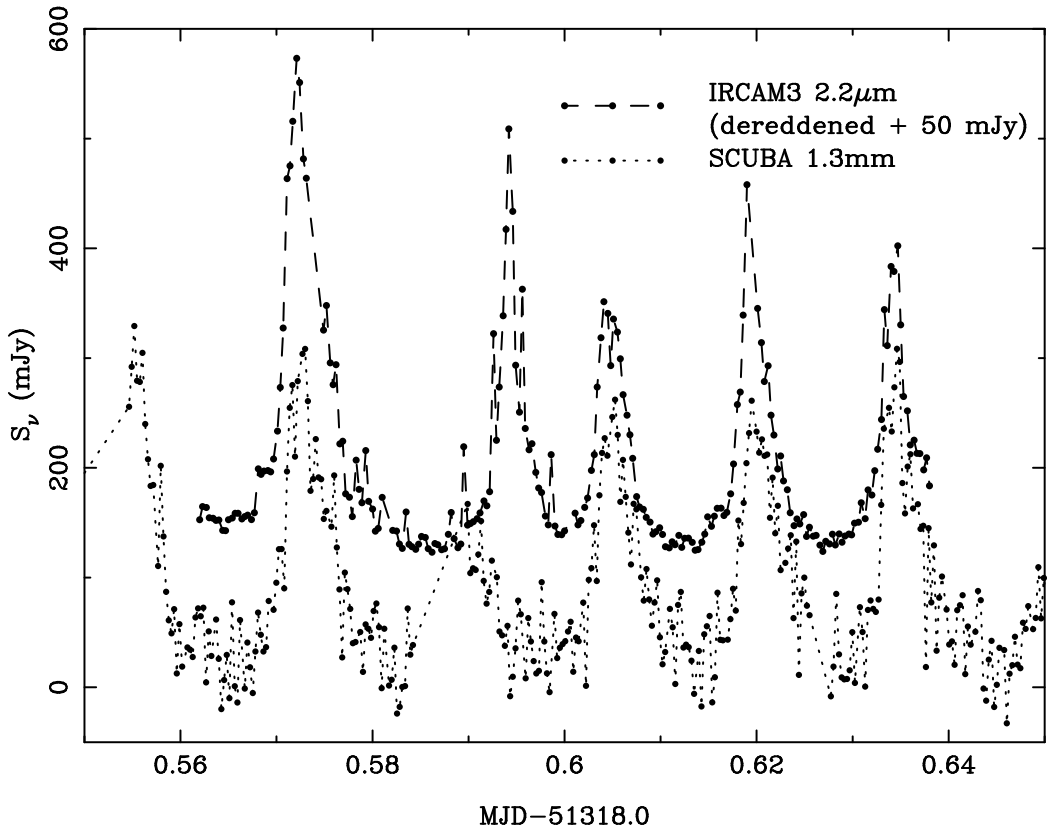

Figure 3.9: Simultaneous IRCAM and SCUBA observations of the flaring events in GRS 1915+105. The image is from Fender and Pooley (2000)

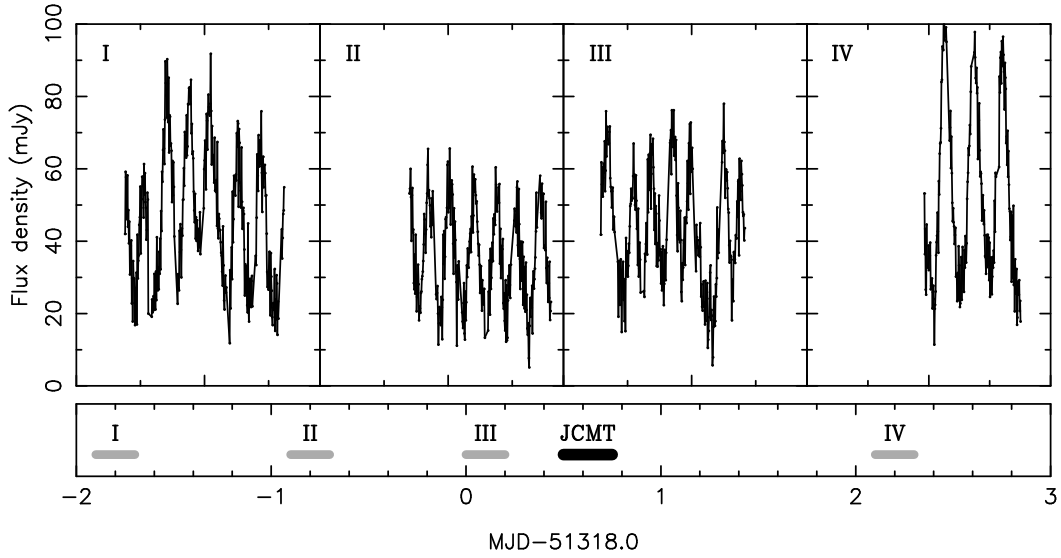

Figure 3.10: Radio observations, using Ryle Telescope, of the flaring events in GRS 1915+105. Each top panel corresponds to 0.2d; the bottom panel shows the UKIRT/JCMT observations distribution. The image is from Fender and Pooley (2000)

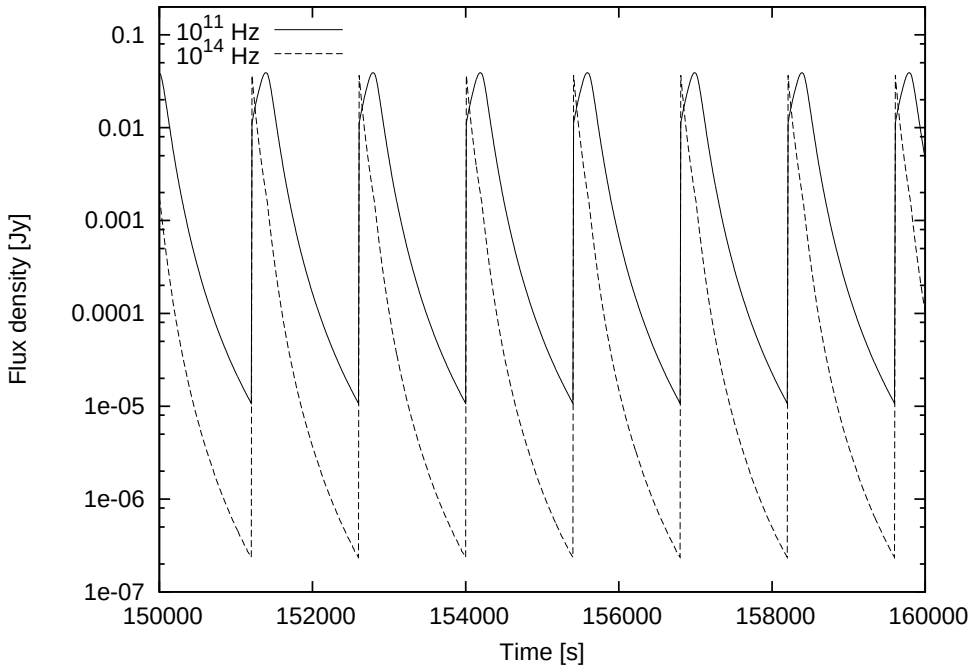

Figure 3.11: The mm and the IR light curves produced by regular injection interval ($\approx$ 1400s) with no collisions taking place.

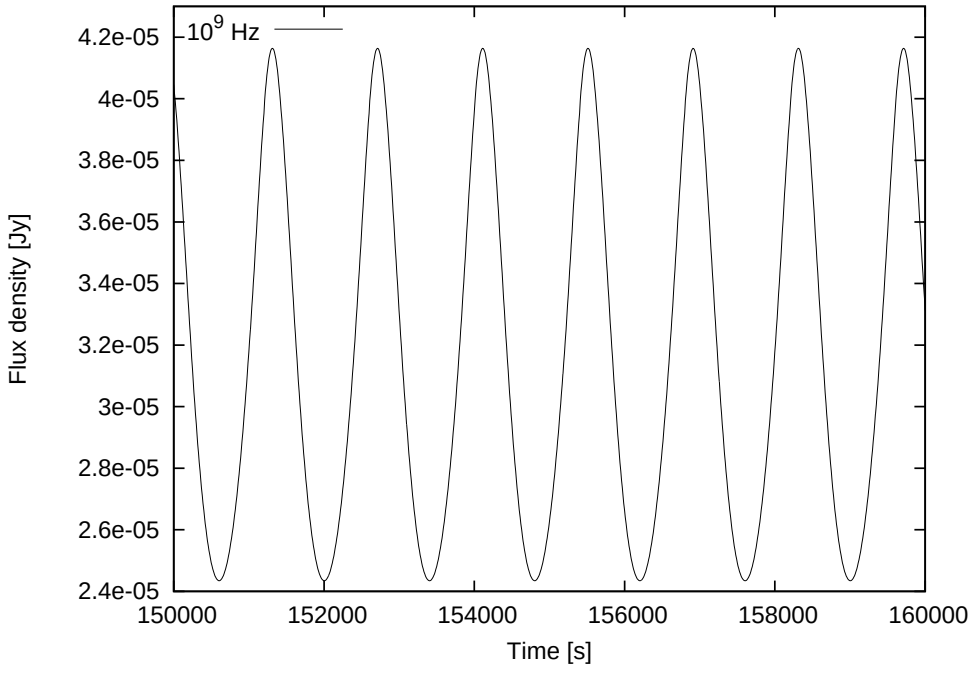

Figure 3.12: The radio light curve produced by regular injection interval ($\approx$ 1400s) with no collisions taking place.

result in a much more energy dense shell, which may be optically thick to the IR frequencies at the start. Unfortunately, this cannot be allowed in the simulation shown here without creating shells with an unphysical energy density. One way to get around this problem would be to allow longitudinal expansion ($u_{th} \neq 0.0$): this is explored in the later scenarios. However, the longitudinal expansion needs to be suppressed here as no mergers are taking place. Even though the periodicity is achieved with this simple set up, the flux is not high enough to model the flares observed in GRS 1915+105. The low flux can be attributed to a couple of factors: the E_{frac} value, and the adiabatic losses without any means of re-energization. Obtaining higher flux values with the help of re-acceleration is explored further in section 3.3.2.3.

3.3.2.2 Sinusoidal M_{shell}: without mergers

The previous section showed that it is possible to obtain the observed periodicity by using discrete massive ejections (simply hardwired in the parameters). The following section explores the possibility of a more continuous variability in the form of shell mass variations. The shell mass is varied with the periodicity of ≈1200 s and the injection frequency is set at 1 Hz ($dt_{inj} \approx 1$ s). The shell mass variation is show in figure 3.13, while the parameters are outlined in table 3.4. The idea behind this sort of variation is that the shell injection is continuous, but the shell mass varies in a way to give the impression of a discrete massive ejection.

The IR-mm-radio variability is illustrated in figure 3.14. Once again the periodicity is achieved, plus the similar rise times for the different frequencies. However, the flux values still remain low and the reasons for this are similar to the ones already outlined in section 3.3.2.1. Even with the shortcomings in the flux values, this is an exciting results as we can see how it may be possible to obtain similar (and almost simultaneous) rise times for very different frequencies.

3.3.2.3 Pseudo-Random shell properties: with mergers

The previous two sections (3.3.2.1 and 3.3.2.2) have shown how the periodicity and the rise times seen in the GRS 1915+105 flares can be reproduced; however, the flux normalization remained too low. The following section attempts to address that problem.

As mentioned before, larger flux values can be obtained if a re-acceleration mechanism is present, in addition to having higher E_{frac} values; the higher E_{frac} values necessitate longitudinal expansion to stop the individual shells from reaching unphysical energy densities. These requirements are reflected in the parameters presented in table 3.5. The periodicity in this case is achieved by, once more, setting dt_{inj} to ≈1300s. Also the variation in Γ, picked randomly between Γ_{min} and Γ_{max}, means that the collisions/mergers take place.

The results are show in figures 3.16, 3.17, 3.18, and 3.19, illustrating the mm, IR and radio light curves respectively. For a comparison with the previous section, figure 3.15 shows the mass distribution of the injected shells. It should be noted that mass distribution of the shells in the jet will be different from that of injected due the mergers taking place. The first point to

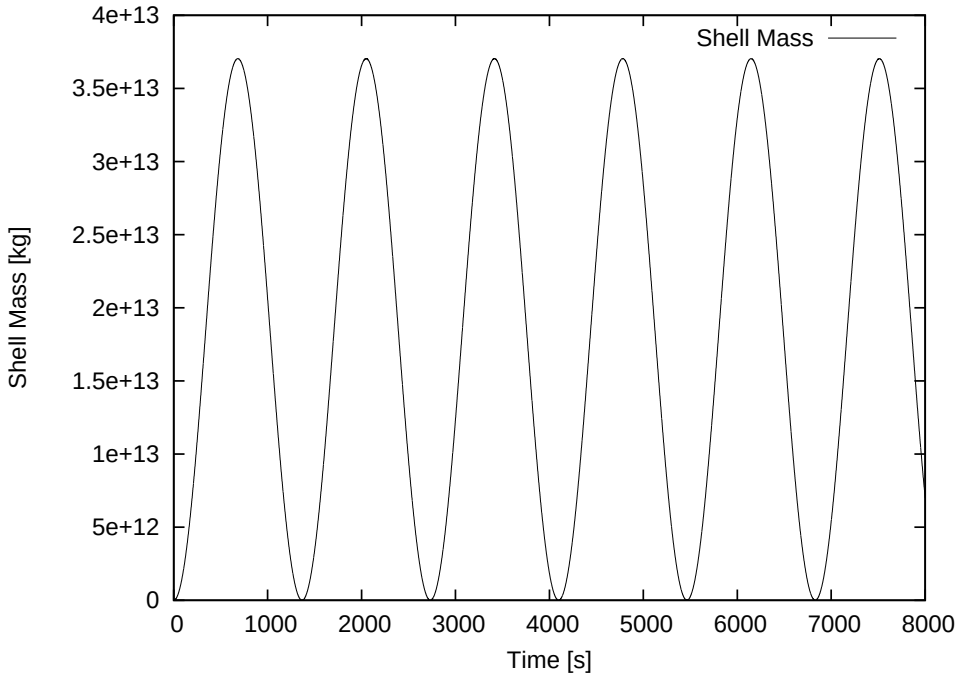

Figure 3.13: The sinusoidal shell mass distribution.

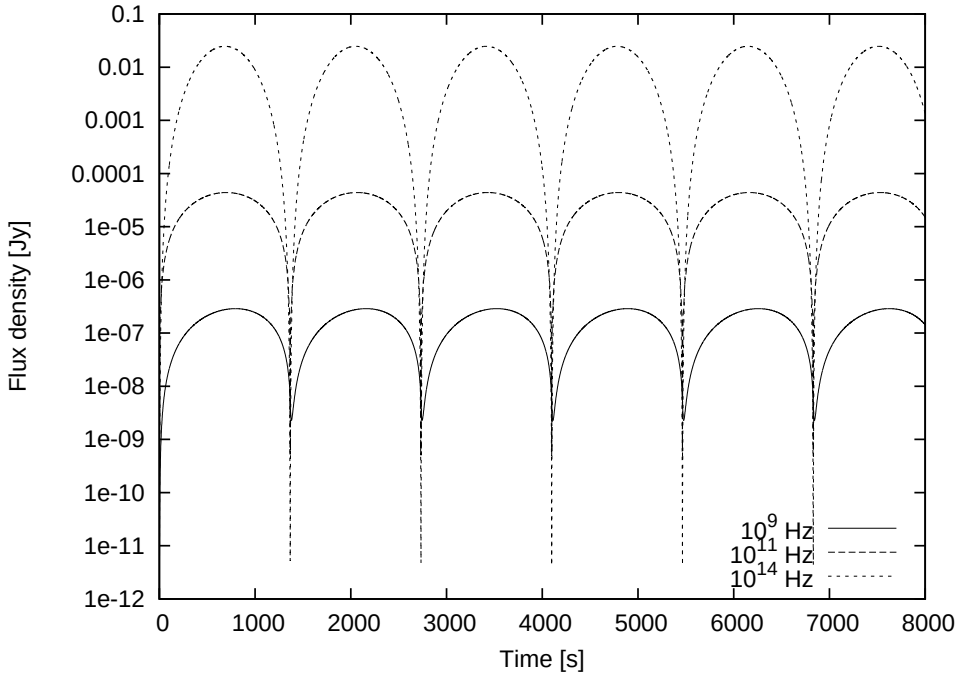

Figure 3.14: The radio, the mm, and the IR light curves produced by sinusoidal shell mass variation with no collisions taking place.

Table 3.4: The parameters used to model GRS 1915+105 flares with sinusoidal shell mass and without mergers.

Parameter	Figures 3.16, 3.17, 3.18, 3.19
φ	5^o
θ	70^o
D	11 kpc
M_{shell}	$\approx 0-1\times10^{13}$ kg
Γ	4.0
l_{scale}	0.3
u_e	0.5
u_B	0.5
u_{th}	0.0
x_{shock}	0.0 ls
E_{frac}	0.1
dt_{inj}	$\approx$1 s
Simulation Duration	$\approx 1\times10^4$ s
Adiabatic Losses	yes

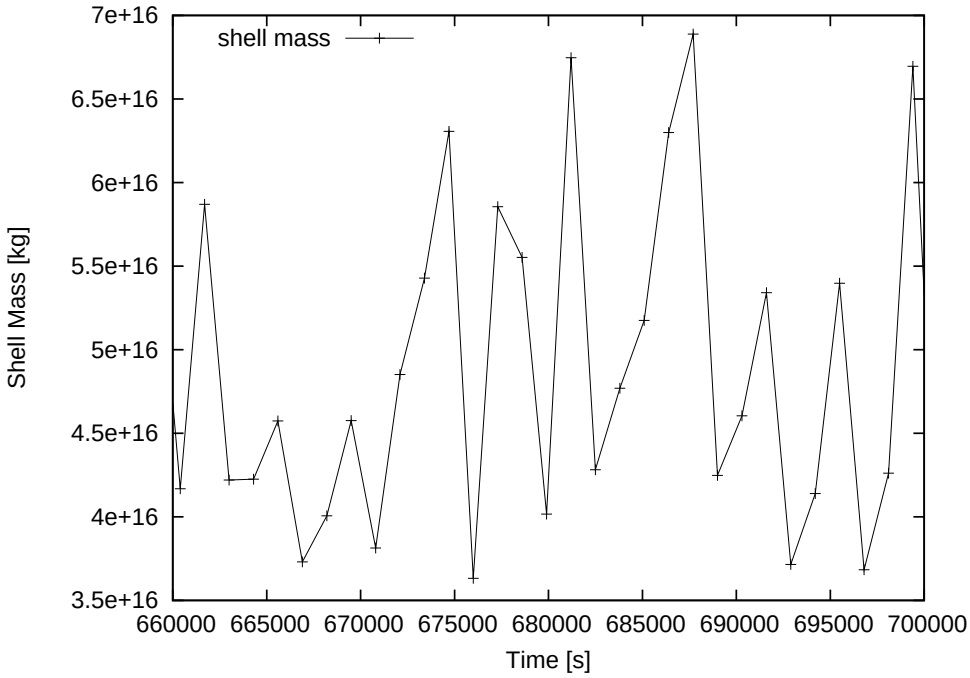

Figure 3.15: The shell mass distribution with pseudo-random shell properties.

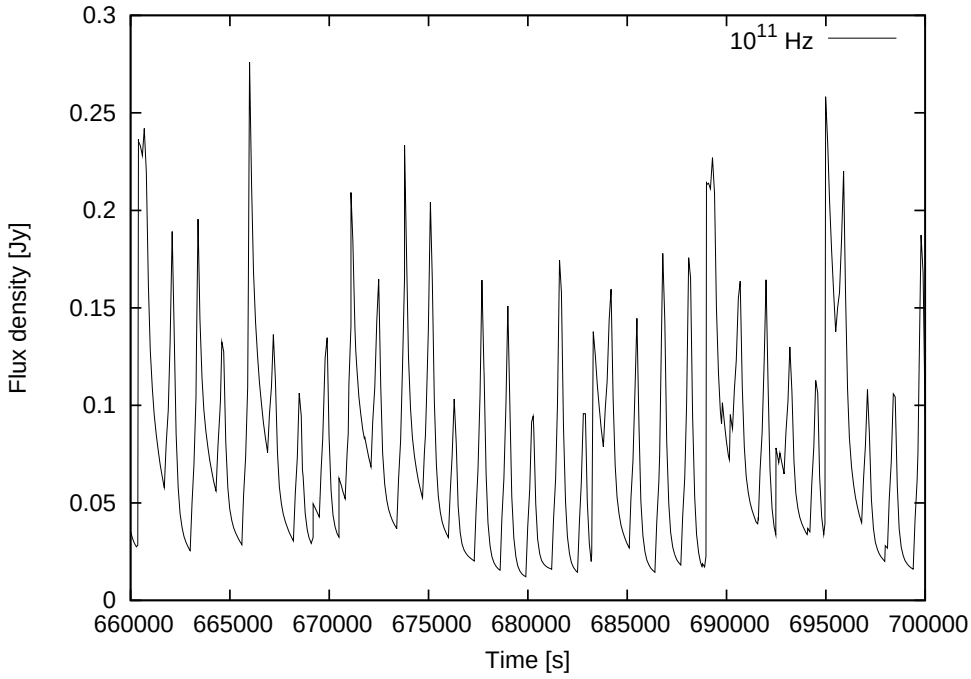

Figure 3.16: The millimeter wavelength light curve with pseudo-random shell properties.

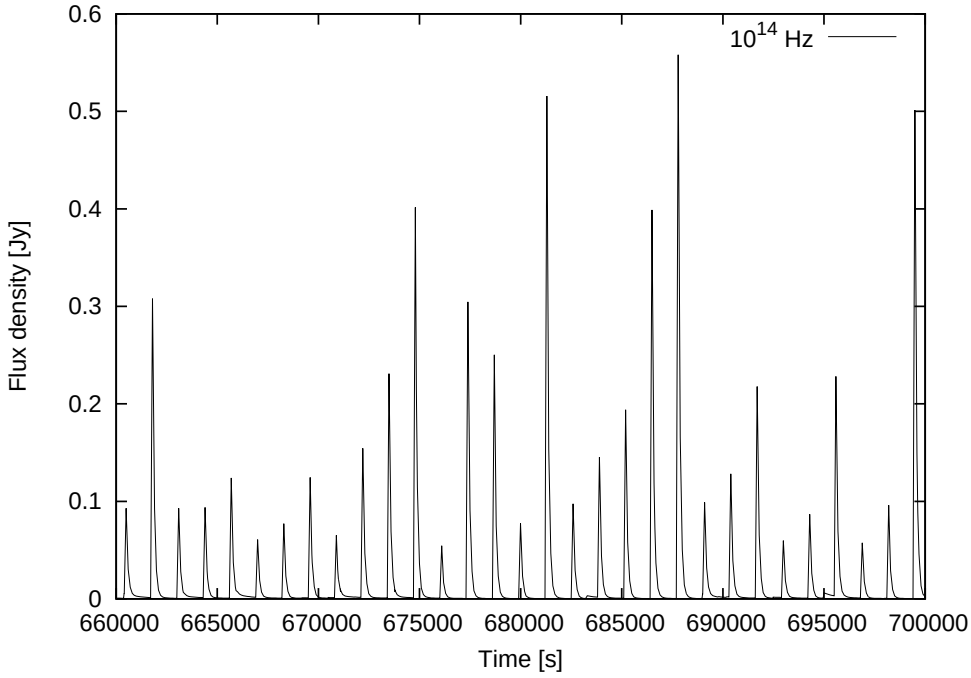

Figure 3.17: The infra-red light curve with pseudo-random shell properties.

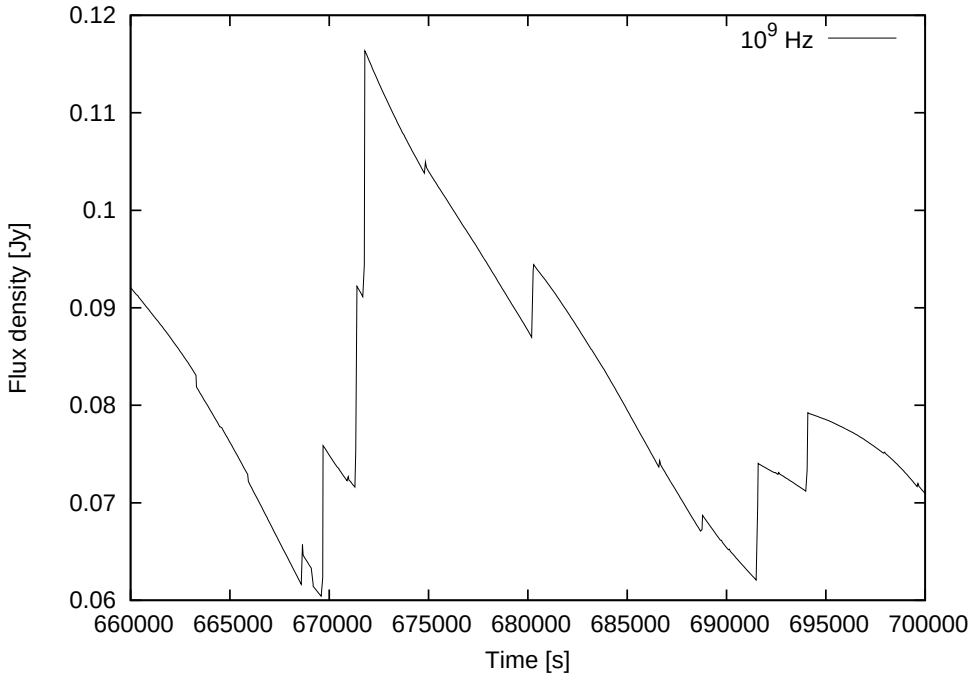

Figure 3.18: The radio light curve with pseudo-random shell properties.

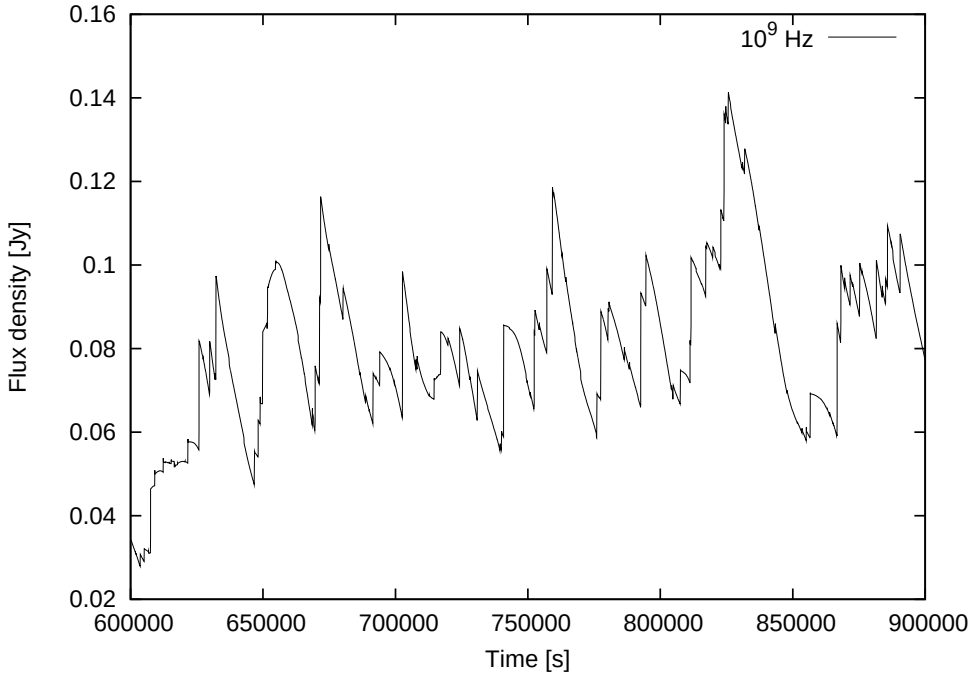

Figure 3.19: The longer radio light curve with pseudo-random shell properties to show the radio flar periodicity.

Table 3.5: The parameters used to model GRS 1915+105 flares with pseudo-random shell properties and mergers taking place.

Parameter	Figures 3.16, 3.17, 3.18, 3.19
φ	5^o
θ	70^o
D	11 kpc
L_W	1×10^{31} J/s
Γ_{min}	2.0
Γ_{max}	4.0
l_{scale}	0.4
u_e	0.33
u_B	0.33
u_{th}	0.33
x_{shock}	0.0 ls
E_{frac}	0.5
dt_{inj}	$\approx$1300 s
Simulation Duration	$\approx 1.3 \times 10^6$ s
Adiabatic Losses	yes

note about the results presented here is that flux values for the different frequencies are in the range that were observed in the GRS 1915+105 repeated ejections. However, the peaks are not uniform. This is caused by the collisions taking place and the different merger efficiency results in different flux values. The mergers also mean that periodicity of the peaks is different from that of the injected shells: the mm-IR periodicity is $\approx$1250 s. However, the radio frequency periodicity is very different. The radio light curve in figure 3.18 shows how for the same time-scale as figure 3.16 and 3.17, the radio peak periodicity is much longer. The longer time-scale radio light curve in figure 3.19 illustrates the extremely long and quite aperiodic nature of the radio emission. The radio emission behaviour is influenced heavily by the mergers: the re-energization makes the shells optically thick to the radio frequencies and with many collisions taking place, the radio rise times are lengthened greatly (the light curve is the summed total of the emission from the entire jet at any given time).

3.4 Conclusions

3.4.1 The flat spectrum

The results presented in this chapter show how it is possible to reproduce a canonical flat spectrum even when a discretized jet is used. We have also shown how the flat/inverted spectrum is also reproducible if the internal shocks are used for the energy replenishment. If the internal shocks are used for the initial electron acceleration, on top of replenishing the energy losses, the spectra become highly inverted ($\alpha > 0$).

The multiple internal shocks created by the multiple ejections into the jet volume can

provide a considerable amount of energy to the shells. The results show that even with an essentially random distribution of the shell velocities and the injection times, adequate re-energization is possible: the flat/inverted spectrum is achieved. This is an important result in furthering our understanding of the jet physics. We have also seen that the high frequency break in the flat/inverted spectra is correlated with the jet power; the lower frequency turnover shows dependence on the number of shells present in the jet in addition to their collision radii. Further investigation is required to quantify, fully, the relation that may exist between the jet properties and the various break frequencies. However, the break frequency correlations seen thus far, are in agreement with the theoretical prediction, as well as the observations.

The results outlined above also hint at being able to tie the timing properties (the X-ray with the optical in the case of X-ray binaries) to the jet physics. It should also be possible to link the shell properties (such as the time gap between the ejections and the bulk Lorentz factor) with the X-ray timing information. A crude attempt at this was made by modelling the repeated ejections from GRS 1915+105.

3.4.2 The flares in GRS 195+105

Modelling the flaring behaviour gave an interesting insight into just how complex that picture really is. At face value, the infra-red and the millimetre data give the impression of large ejections from the source. The data, however, are not reproducible with this kind of a scenario. The closest match to the GRS 1915+105 behaviour was seen when the shell masses were made to vary sinusoidally, rather than with the straightforward periodicity in ejection times. The main drawback of the sinusoidal mass picture is the flux normalization being too low. “Correct” flux values could be obtained with the re-accelerating mergers taking place, but the periodicity of the light curves was lost (especially at the radio frequencies). This suggests that the “repeated massive” ejections scenario is some combination of the scenarios presented here (that is, the masses could be varying with time, plus the re-energization taking place, but perhaps not in the form of the discrete mergers modelled here).

The jet timing properties and how it may be possible to tie the X-ray timing information with the optical light curves are explored further in the next chapter.

4

Jet timing analysis

The following chapter delves a little further into exploring the timing properties of X-ray binaries and their jets. The salient timing properties of these sources are outlined with the current models for explaining these data. The tools and techniques specific to this investigation are outlined as well. The results from the *i*Shocks simulations are also presented.

4.1 Optical/X-ray Correlations in XRBs

Some of the key X-ray binary timing properties were outlined in chapter 1 (specifically section 1.2.3). The following work focuses on one particular aspect of the various relations exhibited by the XRBs: the optical/X-ray correlations.

The first question would be: why focus on these correlations at all? The main motivation is that these correlations are quite likely to be the best way to probe the disc:jet connection from the inner parts of the disc, nearest the black hole: the X-rays originate from inner, hotter parts of the disc, while the optical emission is from the inner parts of the jet. Thus, these correlations are a window into the regions very close to the black hole. The other motivation for focusing on these correlations, in the present work, is the fact that there are still many unexplained results of optical and X-ray timing which require attention.

The simultaneous X-ray and optical observations of the transient source XTE J1118+480 have provided one of the best and earliest examples of the optical/X-ray correlated variability (Kanbach *et al.*, 2001) (also see Hynes *et al.*, 2006). Similar behaviour has now also been observed in the source GX 339-4 (Gandhi *et al.*, 2008). In the case of XTE J1118+480, the X-rays and the optical show a very distinctive correlation. The optical emission shows a lag (with

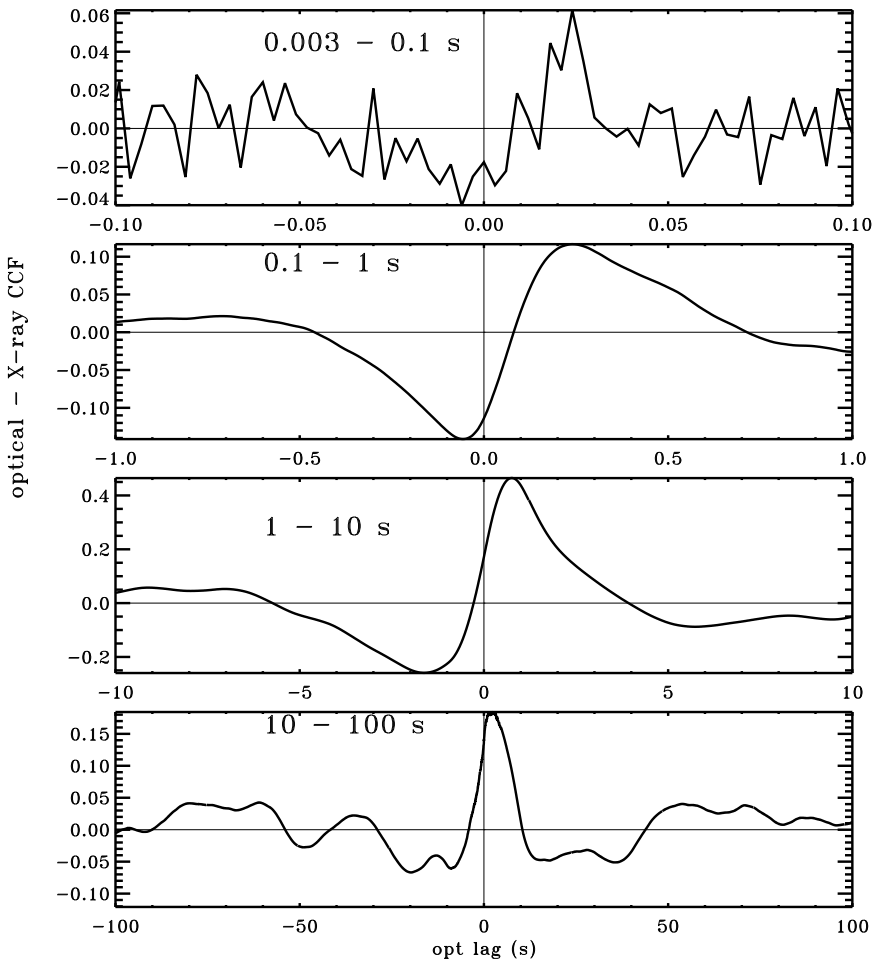

Figure 4.1: The optical vs. X-ray CCFs for XTE J1118+480 for a variety of time-scales. The pre-cognition dip and the positive lags can be seen at almost all the time-scales. The image is from Malzac *et al.* (2003).

respect to X-ray) of a few tens of milliseconds. The rapid variability of the optical emission has meant that it is not considered to originate from the cool optical emitting outer part of the accretion disc. The re-processing of the X-rays from the outer part of the disc is also ruled out on the basis of the auto-correlation functions: if the optical emission is the re-processed X-rays, the optical auto-correlation function should be wider than that of the X-rays; however, the opposite is observed.

Among other interesting properties, the optical/X-ray cross correlation function (CCF) show a dip before a sharp rise associated with the positive lag — the "pre-cognition dip". In other words, the optical emission shows a decline *before* the rise in the X-rays. This kind of pre-cognition re-enforces the case against the re-processing scenario, in addition to presenting an extremely interesting problem. The CCFs show the same behaviour on a variety of time-scales (Malzac *et al.*, 2003): this is illustrated in figure 4.1.

Even though the source GX 339-4 shows similar behaviour, there are also some quite interesting differences (figure 4.2). The main one being that the GX 339-4 CCF is a mirror image

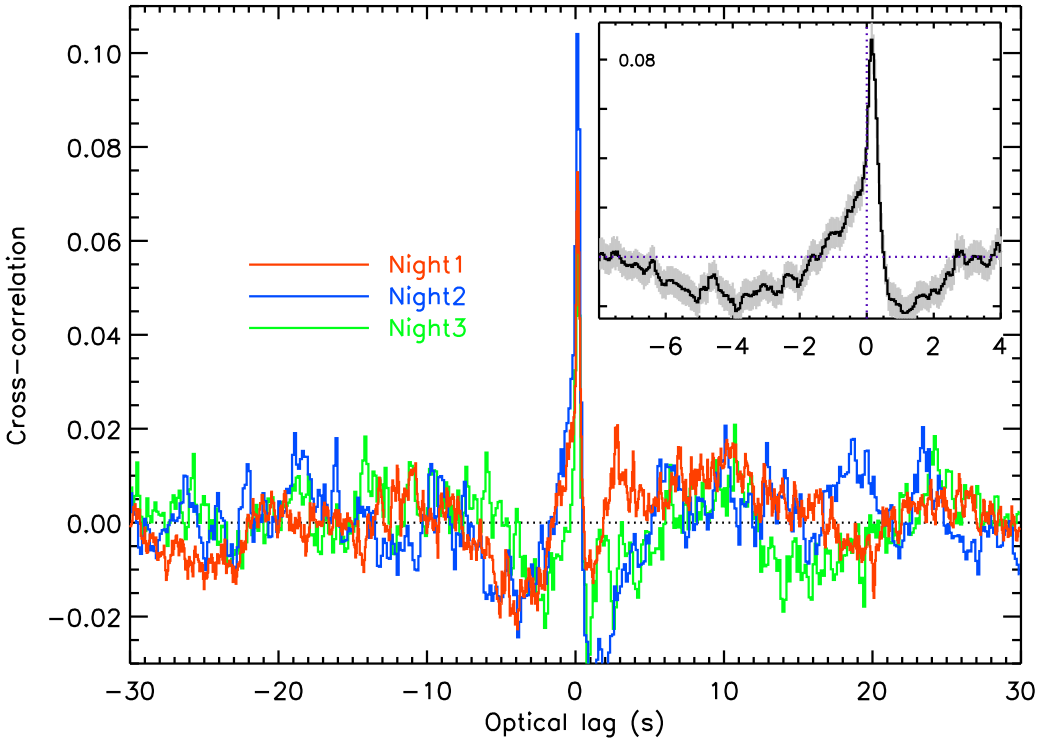

Figure 4.2: The optical vs. X-ray CCFs for GX 339-4 on different nights. The inset shows the average CCF. The image is from Gandhi *et al.* (2008).

of the XTE J1118+480 CCF. That is, there is a slow rise and a sharp decline in the CCF rather than the vice versa observed in XTE J1118+480 (see figure 4.1). The pre-cognition dip also does not appear as distinct, plus there is another dip after the positive lag peak. The time-scales also appear to be longer; however, as we saw in the case of XTE J1118+480, a variety of time-scales were present for the CCF. Gandhi *et al.* (2008) on the other hand do not present any such detailed analysis, but this does not rule out GX 339-4 possessing longer time-scales as well. These, however, are not the only sources that exhibit these characteristics; SWIFT J1753.5-0127 has also been observed to show similar, and quite interesting, optical/X-ray correlations (Durant *et al.*, 2008), demonstrating the possibility that these correlations could be inherent to the disc:jet geometry rather than a quirk of a particular source.

4.1.1 Current models

Current the most successful explanation of the source XTE J1118+480 optical/X-ray behaviour has been provided by Malzac *et al.* (2004). They suggest an energy reservoir model for explaining the various optical/X-ray correlations. A very brief description of this model is given below.

Malzac *et al.* (2004) use a simple analogy of a tall water tank with two outlets (one large and one small; large outlet has a valve on it) and one inlet. The large outlet represents the jet power, the small outlet represents the X-ray power, and the inlet is the power coming into

the energy reservoir that feeds both the jet and the X-rays; the optical emission is assumed to come from the jet via the synchrotron emission. The jet power therefore has an influence on the X-ray output and vice versa; hence, a rather complex correlation. The authors state that the model is independent of the exact nature of the energy reservoir. However, they propose a scenario where the magnetic energy constitutes the energy reservoir.

The time dependent aspect of the model is determined by the dissipation rates, for both the X-rays and the jet, that link the time-dependent jet power (and the X-ray power) with the energy available to these outputs. The dissipation rate, plus the power input are allowed to fluctuate randomly and the values that best fit the observations are chosen. The fluctuation is assumed to have a shot noise profile.

The authors are able to reproduce many of the XTE J1118+480 optical/X-ray correlation behaviours and provide the best fit parameters. This model has not been applied to the source GX 339-4 data, thus the differences between these two sources have not been explained. The authors also concluded that these correlations arise in a jet-dominated regime. In other words, the jet power is much greater than the X-ray luminosity ($P_{jet} >> L_X$) — an exciting and original result at the time. However, due to the complexity of the model, it is not surprising that the parameter-space exploration was not exhaustive. Their model is therefore excellent for explaining the XTE J1118+480 observations from a phenomenological point of view, but the physical interpretation of such a model remains problematic.

Another interesting property of XTE J1118+480 data is that the optical flux scales not only with X-ray count rate, but also the X-ray variability (Malzac *et al.*, 2003). Specifically, the optical emission is correlated with the rate of change in the X-rays. Malzac *et al.* (2004) are able to reproduce this with the aide of a randomly fluctuating parameter that gives their model the time-dependent property. The optical lags are also simply assumed to occur due to the matter injected into the jet emitting photons after a given time. The upshot therefore is that the Malzac *et al.* (2004) model has been an excellent starting point for a better phenomenological understanding of these correlations, but more physical modelling is necessary to complete the picture.

4.2 Using *i*Shocks to model optical/X-ray relation

The *i*Shocks architecture, with the shell structure plus the changes in the shell bulk Lorentz factor and the shell mass influencing the merger properties, is ideal for exploring the X-ray optical correlations. If one considers the X-ray data to be correlated with accretion rate then this can be translated into the jet properties, and subsequently the shell properties. Also, in order to explore the observed X-rays rate-of-change correlation with the optical, *i*Shocks can be used to simulate the rate-of-change of the shell properties and see how this impacts the optical.

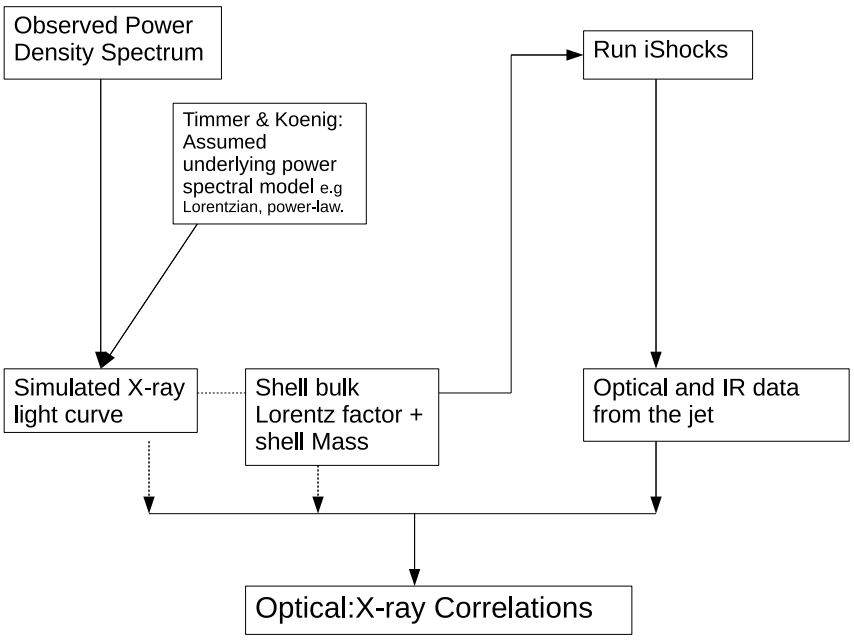

Figure 4.3: The flow-chart shows the various steps involved in generating the shell Lorentz factor and the shell mass time-series, which is then used in the *i*Shocks model. The optical (or the required frequency) data can then be used to correlate with the simulated X-ray or the shell properties time-series data. The end results is to obtain the optical/X-ray(simulated) correlations.

4.2.1 Generating the time series

The main technique used in the following chapter, which has not yet been outlined, is the time series (light curve) simulation. Timmer and Koenig (1995) presented a very useful method for the simulation of light curves. The same method is adapted here to generate the shell mass and the bulk Lorentz factor time series (Uttley, 2009).

The first step in the time series generation is obtaining the power density spectrum (PDS). An underlying power spectral model and its normalization are chosen to model the PDS. The models can take a variety of forms, such as: Lorentzians, power-law, and/or any combination of the two. Then at each Fourier frequency, two Gaussian-distributed random numbers are drawn and multiplied by the square root of half the power spectral model value at that frequency. These two numbers represent the real and the imaginary parts of the Fourier transform of the simulated data. The Fourier components for the negative frequencies have to be chosen such that they are the complex conjugate of the positive frequencies: this is required to produce real valued time series. The inverse Fourier transform of the simulated data then yields the simulated light curve. The simulated light curves form a random subset of the all the possible light curves for a given power spectral model. Figure 4.2.1 shows the various steps involved in the whole process.

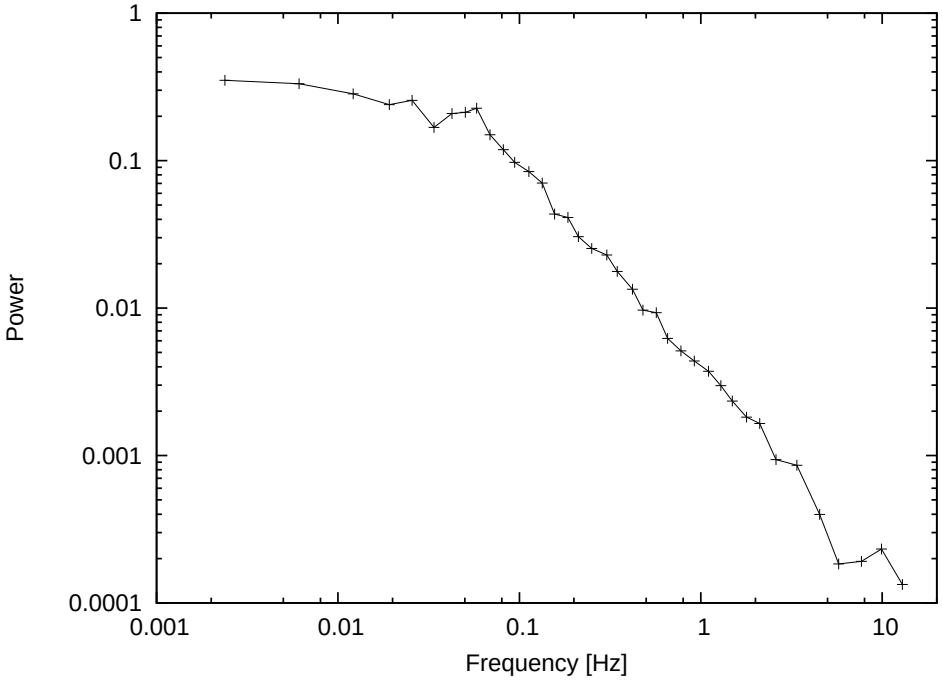

Figure 4.4: The XTE J1118+480 X-ray power spectrum. The image data has been extracted from Malzac *et al.* (2003).

The process used for generating the X-ray light curve can also be applied to generate the shell mass and the bulk Lorentz factor time series. These, however, require further constraints. The mass time series is normalized to unity and does not drop below zero. The user-set shell mass is then used to scale the shell masses for the simulation. The bulk Lorentz factor (Γ_{sh}) is constrained to be greater than unity and then scaled similarly to the shell mass; Γ_{sh} is also *weighted* according to the mass "flux" in a given time bin. That is, a higher shell mass also results in a higher bulk Lorentz factor. This is done due to the relativistic energy relationship ($E = \Gamma_{sh} M_{sh} c^2$) between the Γ_{sh} and the shell mass; without any data on how these quantities may scale together, this is a first order modelling of such a relationship. The Γ_{sh} and the M_{sh} time series can be modelled using separate Lorentzians or both tied to an arbitrary combination of Lorentzians and broken power-law power spectral components.

The time series, apart from the two simple set-ups presented in sections 4.3.1 and 4.3.2, have been generated in order to model the X-ray PDS observed in XTE J1118+480 (Malzac *et al.*, 2003); this is shown in figure 4.4. Such a power spectrum can be approximated using two Lorentzians (one Lorentzian at 0.01 Hz and another at 0.1 Hz) or a broken power-law (with the high frequency break at 0.1 Hz and the high frequency slope of 1.4; the low frequency break can be set at 0.001 Hz and the mid-frequency slope of 0.1). It should be noted that we do not aim to do detailed fitting of the power-spectrum, but rather to make a qualitative fit to study the possible links between the X-ray variability and the optical emission.

4.2.2 The *i*Shocks set-up

The previous chapters outline how it is possible to reproduce the canonical flat/inverted spectrum using the *i*Shocks model. The following investigation shows that our model can be used to understand the optical/X-ray correlations better. With the shell mass and the bulk Lorentz factors affecting the flux directly, the model lends itself naturally to such a study. This study will be the first attempt to tie the jet physical properties with the timing properties.

As mentioned earlier, the optical[1] flux is correlated with the rate of change in the X-rays. In our model, this rate-of-change can interpreted as the change in the shell mass or the shell bulk Lorentz factor, which then may be correlated with the optical flux; the previous section outlined how the Γ_{sh} and the M_{sh} time series can be produced based on the X-ray variability.

It has been shown that the internal energy plays quite an important role in achieving a flat/inverted spectrum (see chapter 3). The timing properties being modelled below are generally found in the hard state of the X-ray binaries: a flat/inverted spectrum is typical of such a state. Therefore in order to be consistent with the parameters essential for obtaining such a spectrum, most of the simulations presented below have the internal energy injection active. The scaling fraction, E_{frac}, for various simulations are outlined in the respective parameters tables.

Injecting the shells with internal energy, however, leads to a limiting, but necessary model constraint on the shock location (x_{shock}). This is the arbitrary location along the jet which marks the point of shell energization (for the initial internal energy injection). In the simulations presented in the previous chapters, this shock location was set to be either zero or kept small ($\approx$ 0.1s in light travel time). In the present simulation this location needs to be a little further along ($\leq$0.5 light seconds) the jet for a couple of reasons. Firstly, the shell sizes are a lot smaller in the present simulation, compared to flat/inverted spectrum simulation due to the smaller injection interval (dt_{inj}). By allowing these shells to move further along the jet, they become slightly larger before being injected with the internal energy, thus avoiding the jets reaching unphysically large energy densities. The flat/inverted spectrum, however, is still reproducible with these parameters; the shell energy (injected and re-energized) influence the high frequency break in the overall spectrum.

Secondly, the shell bulk Lorentz factors are smaller here than in previous simulations (chapter 3). That is, the maximum value is set be low ($\sim$1.2). This means that a longer delay is required for the shells to move away from the source without creating a pile up. By having the shock location a little further out, the longitudinal expansion is delayed as well, avoiding all the collisions taking place at the source itself. The low bulk Lorentz factor values are used to moderate the collisions location along the jet: with the sub-second cross correlation values and high variability, the collisions need to happen at quite small radii. The lower BLF values for a jet have also been found by other authors [for example see Malzac *et al.* (2009)]

For a more physical interpretation, however, the arbitrary shock location can be thought of

[1] the optical here, and other places in this chapter, corresponds to the wavelength of 450 nm in the visible light range (frequency of $\sim 7 \times 10^{14}$ Hz)

as the size/location of the jet "nozzle" put forward by various authors (Falcke and Biermann, 1995; Falcke, 1996; Markoff *et al.*, 2001). The jet nozzle is considered the zone where the initial plasma acceleration takes place: *i*Shocks differs from the other simulations by considering several other re-energizations via the mergers. Of course, currently the size of this nozzle or shock-location cannot be constrained directly from observations and is a free parameter in the simulations.

4.3 Results

The following section presents the results obtained for reproducing the kind of X-ray and optical timing behaviour seen in the sources XTE J1118+48 and GX 339-4. The main focus shall be on XTE J1118+480, with a rather brief look at how the picture looks for GX 339-4.

The sections have been split according to the combination of parameters used for the simulation: the shell mass and the bulk Lorentz factor are combined in a variety of manners to explore this parameter space.

4.3.1 Mass variable; constant Γ_{sh}

The first and the simplest scenario to explore is the one with no shell collisions taking place: all the shells are injected with the same bulk Lorentz factor and the thermal (longitudinal expansion) is suppressed. The adiabatic energy losses are being modelled. This does mean that a flat spectrum would not be achievable, but gives an idea of how to proceed further.

The mass time series was produced using the techniques outlined in section 4.2.1: two Lorentzians (0.1 Hz and 0.01 Hz) were used to model the power spectrum (the other simulation parameters are outlined in table 4.1). The resultant optical-M_{sh} CCF is shown in figure 4.5. The first point to note is that the optical light curve lags the shell mass time series by $\sim$0.95 s with a strong correlation. This strong symmetric correlation is not a surprise as no shell collisions are taking place. As it will be shown later, shell collisions are a major source of variability in the optical light curve. In this simulation, the optical light curve simply traces the input mass variation, with the lag reflecting the delay due to the shock location and the time the shell emission takes to peak at the observed frequency.

4.3.2 Γ_{sh} variable; constant mass

Next we consider the case where the shell bulk Lorentz factors are varying. Similarly to the previous scenario, the shell bulk Lorentz factor distribution is modelled using two Lorentzians (0.1 Hz and 0.01 Hz); the shell mass in this case is kept constant at 1×10^{11} kg. (The variation in Γ_{sh} will also mean variations in the jet power, $\Gamma_{sh} M_{sh} c^2$, similarly to the case where only the mass is varying.) The other simulation parameters are outlined in table 4.2. The optical-Γ_{sh} CCF shown in figure 4.6 display an interesting behaviour: there is not only an expected positive lag for the optical emission, but also an anti-correlation. The cross correlation is also

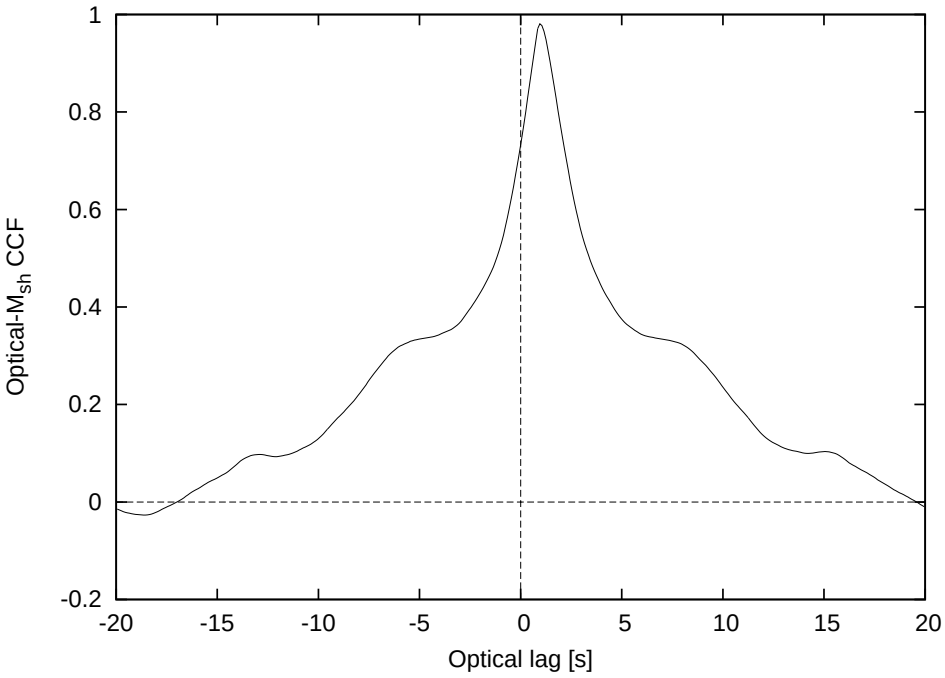

Figure 4.5: The optical-Mass cross correlation function with no collisions taking place. The optical light curves lags the mass times series by $\sim$0.95 s

Table 4.1: *i*Shocks parameters for modelling the optical variability with no collisions taking place

Parameter	fig 4.5
High Freq. Lorentzian	0.1 Hz
Low Freq. Lorentzian	0.01 Hz
φ	5^o
θ	70^o
D	1.9 kpc
L_W	$\sim 1 \times 10^{31}$ J/s
Γ_{min}	1.3
Γ_{max}	1.3
dl	1×10^6 m
u_e	0.5
u_B	0.5
u_{th}	0.0
E_{frac}	0.01
x_{shock}	0.1 ls
dt_{inj}	0.1 s
Sim. Duration	1×10^3 s

Table 4.2: *i*Shocks parameters for modelling the optical variability with only the bulk Lorentz factor varying and constant mass.

Parameter	fig 4.6, 4.7, and 4.8
High Freq. Lorentzian	0.1 Hz
Low Freq. Lorentzian	0.01 Hz
φ	5^o
θ	70^o
D	1.9 kpc
L_W	$\sim 1 \times 10^{29}$ J/s
Γ_{ave}	1.1
M_{sh}	1×10^{11} kg
dl	1×10^{6} m
u_e	0.33
u_B	0.33
u_{th}	0.33
E_{frac}	0.01
x_{shock}	0.5 ls
dt_{inj}	0.1 s
Sim. Duration	1×10^{3} s

asymmetric (c.f. figure 4.5). The positive lag can once again be attributed mainly to the time taken for the shells to peak at the observed frequency. The bulk Lorentz factor will play a part in that due to the scaling of the internal energy with the total relativistic energy of the shell. The anti-correlation behaviour, however, is a bit more complex.

The optical light curve and the bulk Lorentz factor time series are shown in figure 4.7. It is evident from the CCF that an extra level of complexity has been added by the mergers taking place. The shell collisions create extra variability in the resultant optical light curve, which also shows in the optical periodogram in figure 4.8. There are additional time-scales in the optical light curve compared with the BLF time series, although they are not obvious in the time series and the light curve shown in figure 4.7. The average distance between the peaks for the bulk Lorentz factor is $\sim$10 s, whereas the optical light curve shows additional peaks at half the time scale; the time-scales are a little clearer to see in the periodogram shown in figure 4.8. The additional peaks in the optical light curve end up being anti-correlated with the Γ_{sh} time series. The additional time-scales in the optical light curve is a direct result of the numerous collisions taking place in the jet at various length scales. In fact, the collisions at different radii along the jet complicate the correlation further as different length scales correspond to different times scales. For this reason effort was made to keep the majority of the collisions in the inner parts ($<$10 light-seconds) of the jet, by setting the average shell bulk Lorentz quite low (for a hard state jet).

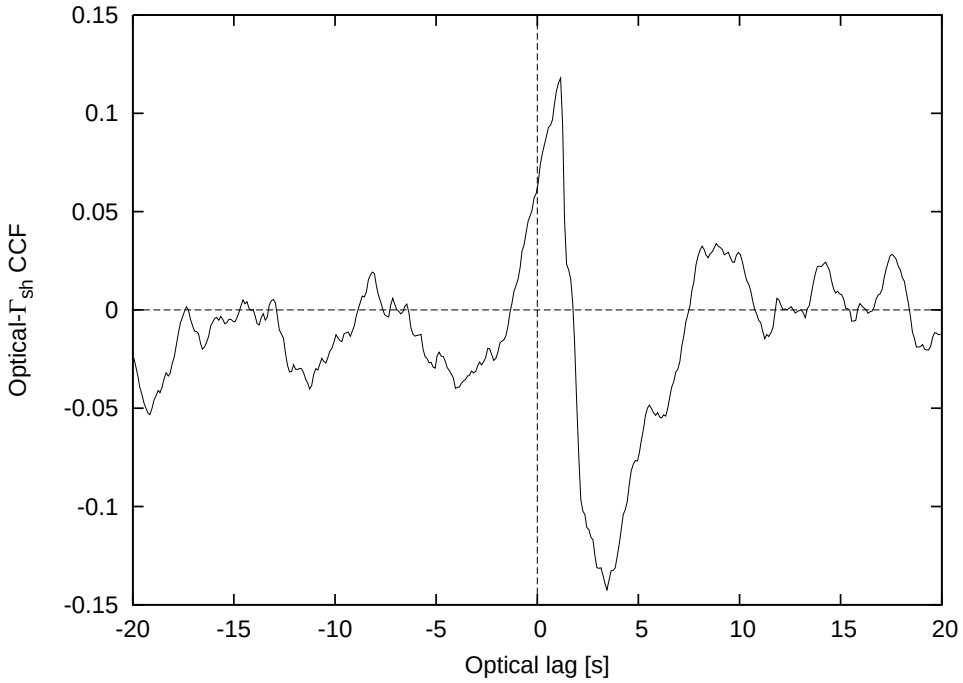

Figure 4.6: The optical-Γ_{sh} cross correlation function with constant mass. The optical light curves lags the Γ_{sh} times series by $\sim$1.15 s and an anti-correlation at $\sim$3.4 s

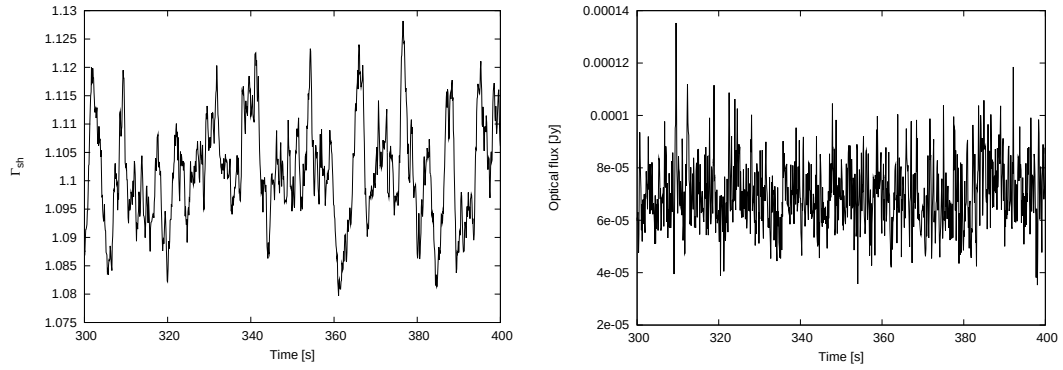

Figure 4.7: The figure on the left shows the bulk Lorentz factor time series; the figure on the right shows the optical light curve corresponding to the same time interval. Γ_{sh} generated using two Lorentzians (0.1 Hz and 0.01 Hz); constant mass

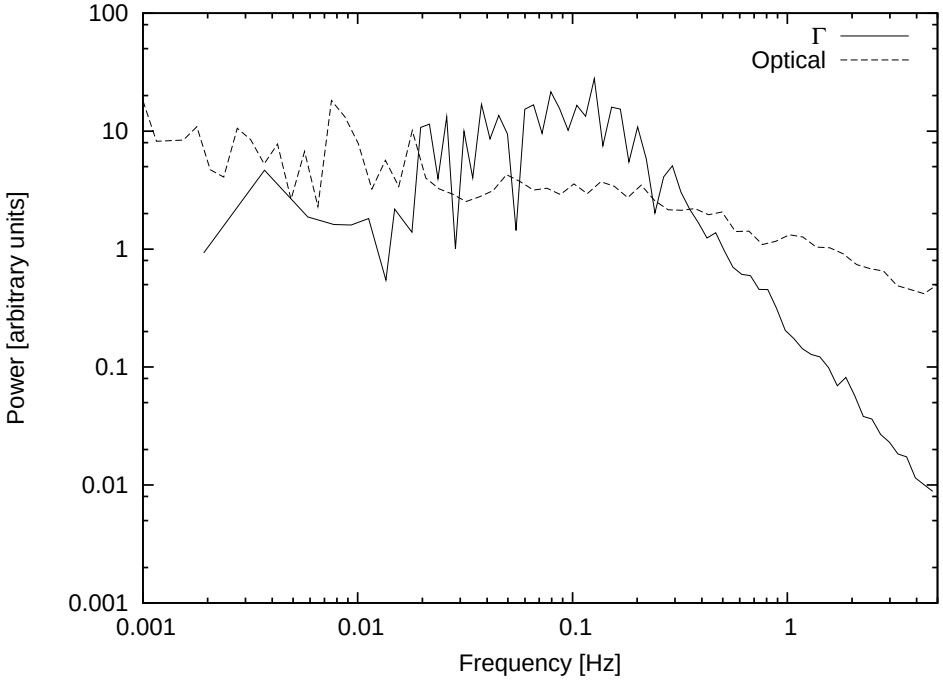

Figure 4.8: The figure shows the bulk Lorentz factor and the optical periodograms. Γ_{sh} generated using two Lorentzians (0.1 Hz and 0.01 Hz); constant mass

4.3.3 Mass and Γ_{sh} variable; two Lorentzians

The next step in exploring these correlations is to let both the shell mass and the bulk Lorentz factor vary. The shell and mass time series are generated by using two Lorentzians (0.1 Hz and 0.01 Hz) to model the power spectrum, similarly to the cases presented earlier. In the following, both parameters (mass and BLF) are tied to both Lorentzians. The mass and the Γ_{sh} distribution will have an identical form; this can be seen in figure 4.9 that shows the mass and the bulk Lorentz factor time series. The resultant Optical-Mass and Optical-Γ_{sh} correlations from the simulations are shown in figure 4.10.

The CCFs once again show an asymmetric form. The anti-correlation seen in the previous set-up is also present, but this time for both the mass and the bulk Lorentz factor, as they have identically behaving time series. It is interesting to note that the anti-correlation appears only when comparing the light curve from the inner parts of the jet with the mass/Γ_{sh} time series. When the light curve is summed over the entire jet, this anti-correlation is washed out by the other time-scales present. The rapid variability in the shell mass means that shells with much different masses are injected on quite short time-scales when compared to the slow variability in mass. Therefore there is a higher shell mass density in the inner parts of the jet, that is, more of the massive shells are injected with a smaller interval. The combination of these factors, plus the Γ_{sh} variability, means that more collisions take place at smaller radii along the jet. The higher mass shells have a higher longitudinal expansion rate, so the average time gap between collisions is reduced and the collision radius also becomes smaller. The results of this

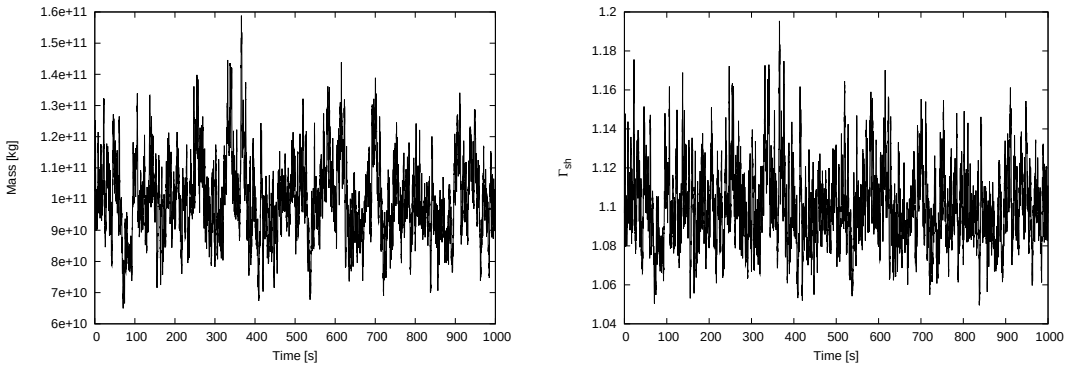

Figure 4.9: The figure on the left shows the mass time series; the figure on the right shows the Γ_{sh} time series. Two Lorentzians (0.01 Hz and 0.1 Hz) are used to model the PDS and generate the time series.

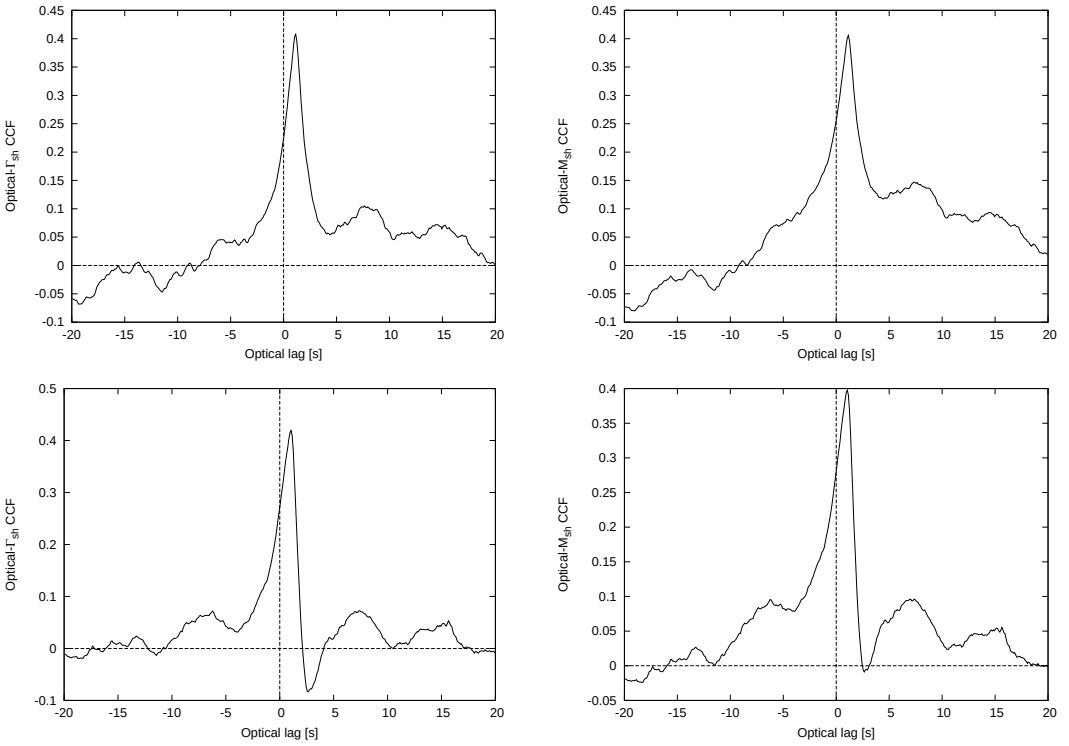

Figure 4.10: The cross correlation function when a double Lorentzian is used to model the Γ_{sh} and the M_{sh} time series. The top left figure shows the Optical-Γ_{sh} CCF from the entire jet; the top right figure shows the Optical-M_{sh} CCF from the entire jet; the bottom left figure shows Optical-Γ_{sh} CCF from only the inner ($\leq$ 3 light seconds) part of jet; the bottom right figure shows the Optical-M_{sh} CCF from only the inner ($\leq$ 3 light seconds) part of jet. The simulation parameters are outlined in table 4.3.

additional variability can be seen in figure 4.11, in the form of a broad QPO like structure at $\sim$0.2 Hz, which does not appear in the mass power spectrum. The increase in variability time-scales, when compared with the input parameter variations, gives rise to the anti-correlation seen in the CCF for the inner parts ($<$ 3 light seconds) of the jet (figure 4.10). The collision rate is lower (i.e. lower variability) in the outer ($>$3 light seconds) parts of the jet. Therefore when the light curve from the entire jet is used for the cross-correlation, the anti-correlation from the inner parts of the jet is suppressed by the multitude of correlations (or the lack of) from the larger length scales.

4.3.4 Mass and Γ_{sh} variable; broken power-law

A similar time-series to the one produced by two Lorentzians can also be modelled using a broken power-law. Figure 4.12 shows the mass and the bulk Lorentz factor time-series used to drive the jet and obtain the optical data. The Γ_{sh} power-spectrum is shown in figure 4.13; the mass times series has an identical form. The main difference between using a two-Lorentzian and a broken power-law spectral model is the high frequency slope, which is set to be 1.4 for the broken power-law, while the Lorentzian has a steeper slope. This difference, however, is not sufficient to change drastically the optical flux behaviour; hence, the CCFs shown in figure 4.14 show a very similar behaviour to the one seen for the case of two-Lorentzian power spectrum modelling. The optical power spectrum from the inner part of the jet (figure 4.13) is also very similar to the one seen for the two-Lorentzian case. Only the optical-M_{sh} correlations are shown in figure 4.14, as the optical-Γ_{sh} has identical form. Just like in the two-Lorentzian

Table 4.3: *i*Shocks parameters for modelling the optical variability with both the bulk Lorentz factor and the shell mass varying using two Lorentzians.

Parameter	fig 4.10
High Freq. Lorentzian	0.1 Hz
Low Freq. Lorentzian	0.01 Hz
φ	5^o
θ	70^o
D	1.9 kpc
L_W	$\sim 1 \times 10^{29}$ J/s
Γ_{ave}	1.1
$Avg.M_{sh}$	1×10^{11} kg
dl	1×10^{6} m
u_e	0.33
u_B	0.33
u_{th}	0.33
E_{frac}	0.01
x_{shock}	0.5 ls
dt_{inj}	0.1 s
Sim. Duration	1×10^{3} s

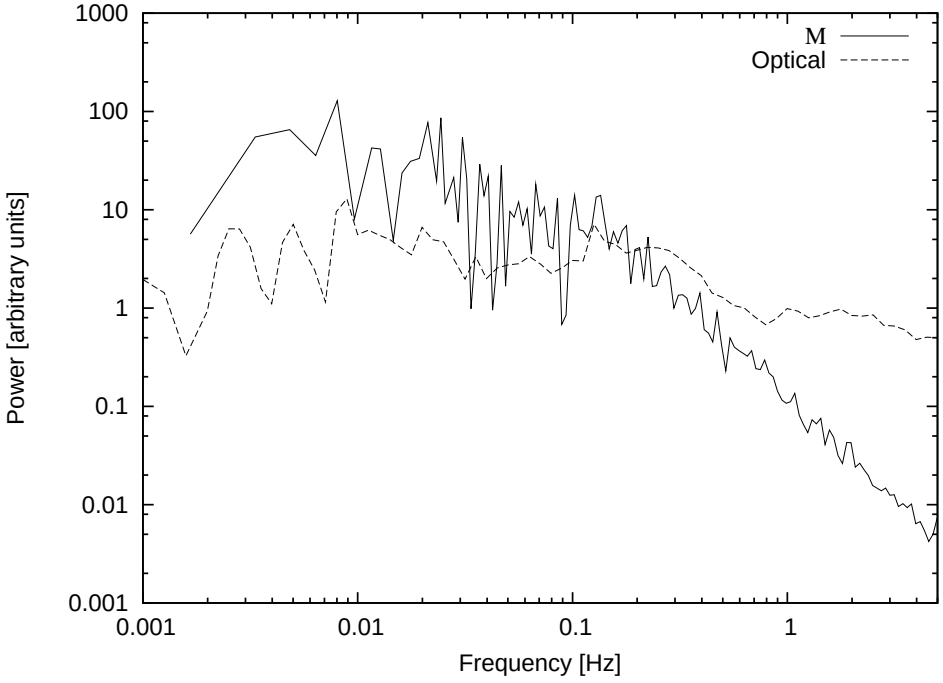

Figure 4.11: The optical periodogram (from the inner part of the jet, $<$3 ls) showing a broad QPO, at $\sim$0.2 Hz, due to the additional variability resultant from the collisions. The shell mass periodogram is also shown. Two Lorentzians (0.1 Hz and 0.01 Hz) are used to model the time series, with both the shell mass and the bulk Lorentz factor varying.

setup, the anti-correlation is present only in the inner part of the jet and washed out on longer time-scales when the entire jet is considered. This demonstrates not only the similarity in the shell Mass and the shell bulk Lorentz factor time series whether modelled using a broken power-law or two Lorentzians, but also the optical emission's dependence on the input time series.

4.3.5 Mass and Γ_{sh} variable; two separate Lorentzians

The previous two sections (4.3.4 and 4.3.3) have presented results with the Γ_{sh} and M_{sh} times series modelled in an identical manner. However, it is possible to generate the mass and the bulk Lorentz factor time series by associating these two parameters with different frequency Lorentzians. Although the separation of these parameters in such a way complicates the correlation, recent evidence suggests there might be merit in exploring this scenario. Wilkinson and Uttley (2009) have found evidence of the disc component showing more variability, especially on long time-scales (i.e. the low frequency Lorentzian), than the power-law component in the hard state. This suggests that quite different components of the power-spectrum can be varying separately. This kind of set-up can therefore be explored by linking different power-spectrum components with different shell properties. Figure 4.15 shows the bulk Lorentz factor and the shell mass time series when the mass and the Γ_{sh} are tied to separate Lorentzians. The figure illustrates how the time-scales in the mass and the bulk Lorentz factor are influenced heavily

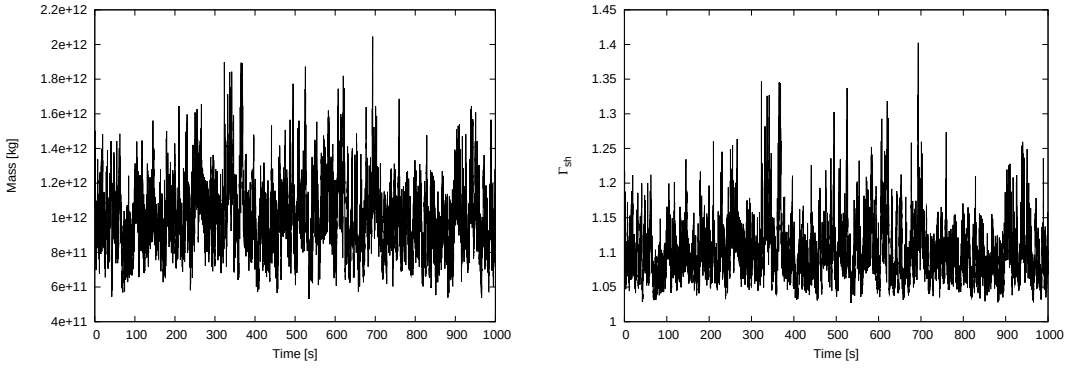

Figure 4.12: The figure on the left shows the mass time series; the figure on the right shows the Γ_{sh} time series. A broken power-law is used to model the PDS and generate the time series.

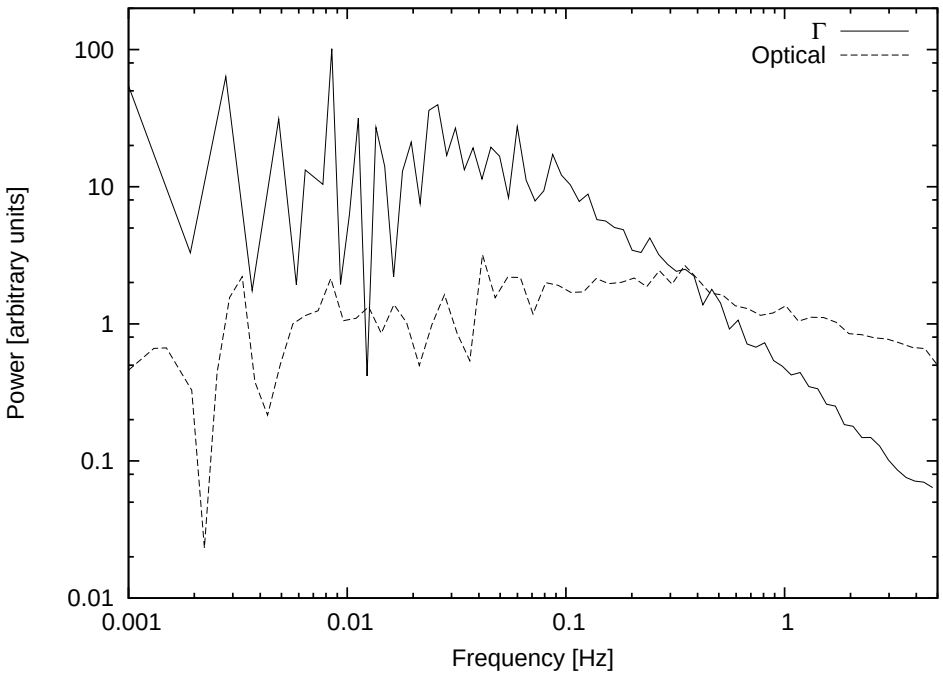

Figure 4.13: The optical periodogram from the inner part ($<$ 3 light seconds) of the jet, plus the shell bulk Lorentz factor periodogram when a broken power-law is used to model the time series. Both the shell mass and the bulk Lorentz factors are varying

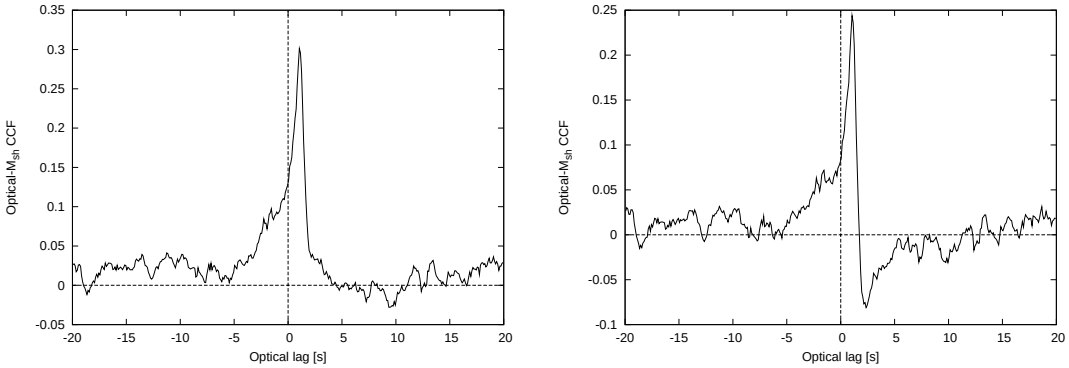

Figure 4.14: The cross correlation functions when a broken power-law is used to model the Γ_{sh} and the M_{sh} time series. The left figure shows the Optical-M_{sh} CCF from the entire jet; the right figure shows the Optical-M_{sh} CCF from only the inner (≤ 3 light seconds) part of jet. The optical-Γ_{sh} CCF has an identical form. The simulation parameters are outlined in table 4.4.

Table 4.4: *i*Shocks parameters for modelling the optical variability with both the bulk Lorentz factor and the shell mass varying using the broken power-law.

Parameter	fig 4.10
Broken P-Law Mid. freq slope	0.1
Broken P-Law Hi. freq slope	1.4
Broken P-Law Hi. freq break	0.1 Hz
Broken P-Law Low. freq break	0.001 Hz
φ	5^o
θ	70^o
D	1.9 kpc
L_W	$\sim 1 \times 10^{29}$ J/s
Γ_{ave}	1.1
$Avg.M_{sh}$	1×10^{11} kg
dl	1×10^{6} m
u_e	0.33
u_B	0.33
u_{th}	0.33
E_{frac}	0.01
x_{shock}	0.5 ls
dt_{inj}	0.1 s
Sim. Duration	1×10^{3} s

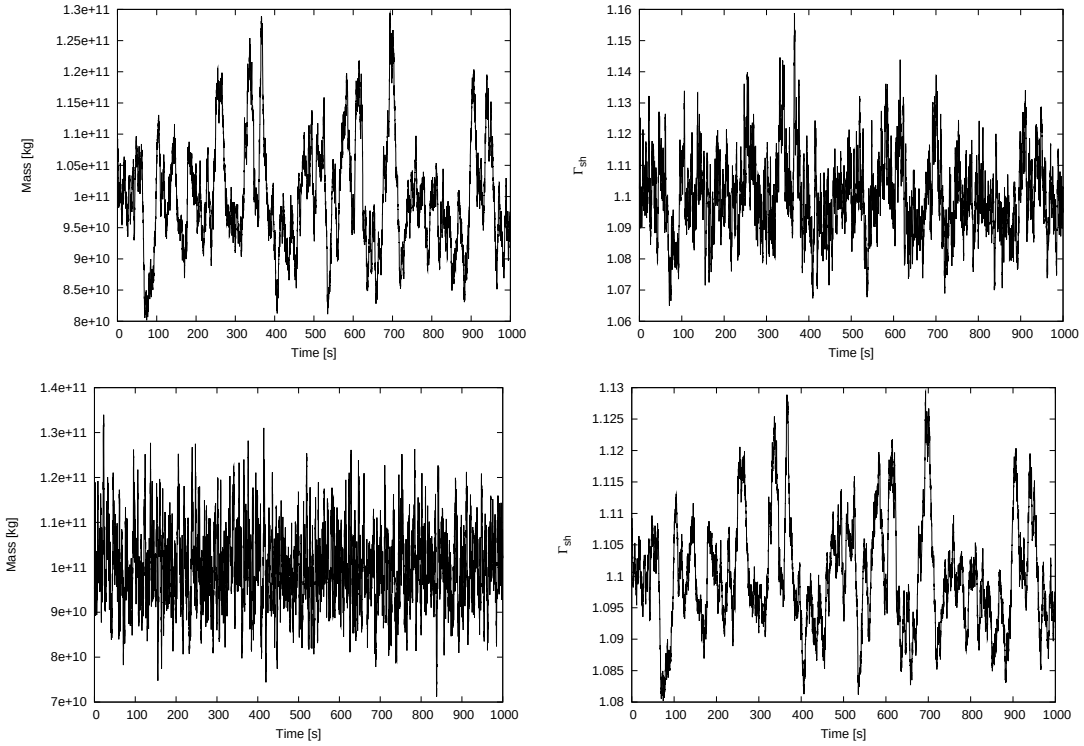

Figure 4.15: Top left: the mass time series when tied to 0.01 Hz Lorentzian. Top right: the Γ_{sh} time series when tied to 0.1 Hz Lorentzian. Bottom left: the mass time series when tied to 0.1 Hz Lorentzian. Bottom right: the Γ_{sh} time series when tied to 0.01 Hz Lorentzian.

by the Lorentzian frequency.

Figures 4.16 and 4.17 show the CCFs for the two of the possible set-ups (when two Lorentzians are being used): (1) the mass tied to the low frequency Lorentzian (0.01 Hz) only and Γ_{sh} to the high frequency Lorentzian (0.1 Hz), (2) the mass tied to the high frequency Lorentzian (0.1 Hz) only and Γ_{sh} to the low frequency Lorentzian (0.01 Hz). The CCFs for these set-ups elaborate further the origins of both the positive lag and the anti-correlation.

When Γ_{sh} is modelled with a high frequency Lorentzian and M_{sh} with the low frequency Lorentzian, a certain fraction of the total number of shell collision take place at radii $\leq$3 light seconds due to the average collision time-gap being influenced by not only the differences in the shell velocities, but also the longitudinal expansion rate (affected by the shell mass). This fraction increases when M_{sh} is modelled with the higher frequency Lorentzian instead, because on average there is a smaller time gap between more massive shells and their faster longitudinal expansion velocity results in them colliding sooner. This shift in the collision radius is reflected in the optical power spectra shown in figure 4.18. The inner radius collision are more energetic and can have a large influence on the power; thus, the different power spectrum shape depending on the where the shell collisions are taking place. The higher optical variability, as a result of higher M_{sh} variability, results in the optical-Γ_{sh} anti-correlation shown in figure 4.17. The same anti-correlation is present, but it is not as strong, when Γ_{sh} has the higher variability (0.1 Hz) instead because, in this set-up, there are fewer energetic collisions

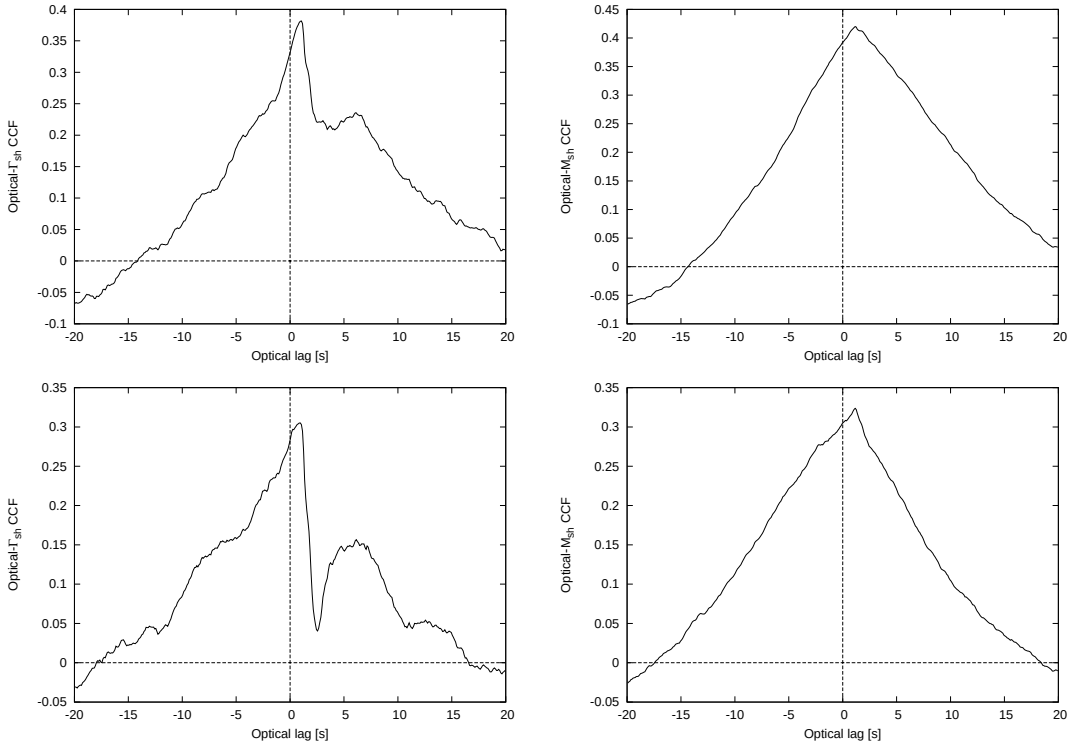

Figure 4.16: The cross correlation functions when the Γ_{sh} is tied to the high frequency Lorentzian, while the mass is modelled with the low frequency Lorentzian. The top left figure shows the Optical-Γ_{sh} CCF from the entire jet; the top right figure shows the Optical-M_{sh} CCF from the entire jet; the bottom left figure shows Optical-Γ_{sh} CCF from only the inner ($\leq$ 3 light seconds) part of jet; the bottom right figure shows the Optical-M_{sh} CCF from only the inner ($\leq$ 3 light seconds) part of jet. The simulation parameters are outlined in table 4.5.

at smaller radii (figure 4.16) when compared to the higher variability in M_{sh}.

Just the way the optical-Γ_{sh} correlation is influenced by the collisions radius, the optical-M_{sh} correlation is also subject to where (and how often) the shell collisions take place. The broad optical-M_{sh} CCF shown in figure 4.16 is symptomatic of the collisions taking place on larger length-scales, resulting in longer time-scales. However, the narrower correlation peak seen in figure 4.17 shows that fewer collisions are taking place at longer time-scales. Interestingly, the optical-M_{sh} correlation from the entire jet (figure 4.17) is the closest yet to the kind of correlations observed in XTE J1118+480. Unfortunately, due to the highly symmetric nature of these correlation, it is difficult to consider this "pre-cognition dip" significant. The lag, however, remains similar to the observed lags.

Although the looking at the optical-Γ_{sh}/M correlations can be very informative, a more *physical* point of view would be from the optical/X-ray(simulated) CCF instead; these are shown in the figure 4.19 for the simulation set-up presented in this section. The simulated X-ray light curve generation technique was outlined in section 4.2.1. The main difference here is that the X-ray light curve is generated using all the power-spectral components, instead of being tied to the individual components. The optical/X-ray correlation show that when the

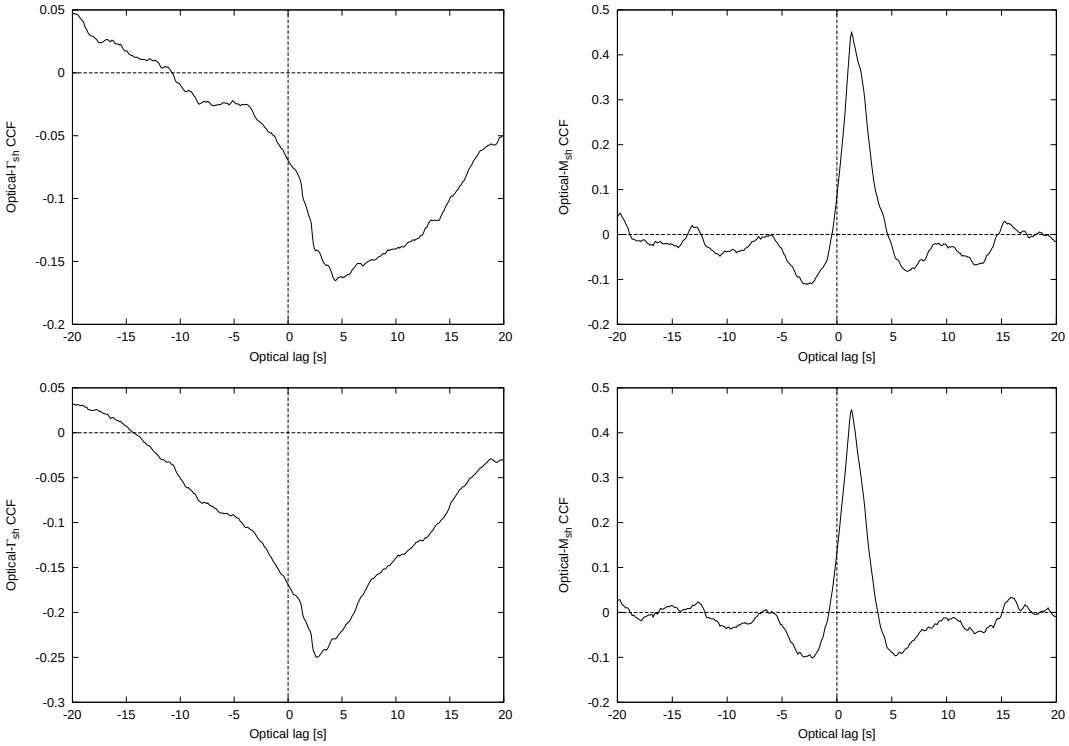

Figure 4.17: The cross correlation functions when the mass is tied to the high frequency Lorentzian, while the Γ_{sh} is modelled with the low frequency Lorentzian. The top left figure shows the Optical-Γ_{sh} CCF from the entire jet; the top right figure shows the Optical-M_{sh} CCF from the entire jet; the bottom left figure shows Optical-Γ_{sh} CCF from only the inner ($\leq$ 3 light seconds) part of jet; the bottom right figure shows the Optical-M_{sh} CCF from only the inner ($\leq$ 3 light seconds) part of jet. The simulation parameters are outlined in table 4.5.

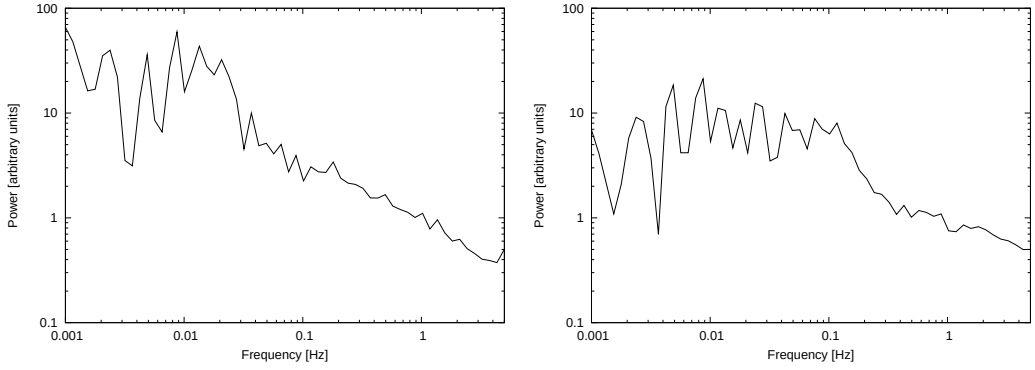

Figure 4.18: Left figure: The optical periodogram when Γ_{sh} is modelled with a 0.1 Hz Lorentzian and M_{sh} with a 0.01 Hz Lorentzian Right figure: The optical periodogram when M_{sh} is modelled with a 0.1 Hz Lorentzian and Γ_{sh} with a 0.01 Hz Lorentzian

Table 4.5: *i*Shocks parameters for modelling the optical variability with both the bulk Lorentz factor and the shell mass varying, but tied to separate Lorentzians.

Parameter	fig 4.16	fig 4.17
M_{sh} Lorentzian	0.01 Hz	0.1 Hz
Γ_{sh} Lorentzian	0.1 Hz	0.01 Hz
φ	5^o	5^o
θ	70^o	70^o
D	1.9 kpc	1.9 kpc
L_W	$\sim 1 \times 10^{30}$ J/s	$\sim 1 \times 10^{30}$ J/s
Γ_{ave}	1.1	1.1
$Avg.M_{sh}$	1×10^{12} kg	1×10^{12} kg
dl	1×10^{6} m	1×10^{6} m
u_e	0.33	0.33
u_B	0.33	0.33
u_{th}	0.33	0.33
E_{frac}	0.01	0.01
x_{shock}	0.5 ls	0.5 ls
dt_{inj}	0.1 s	0.1 s
Sim. Duration	1×10^{3} s	1×10^{3} s

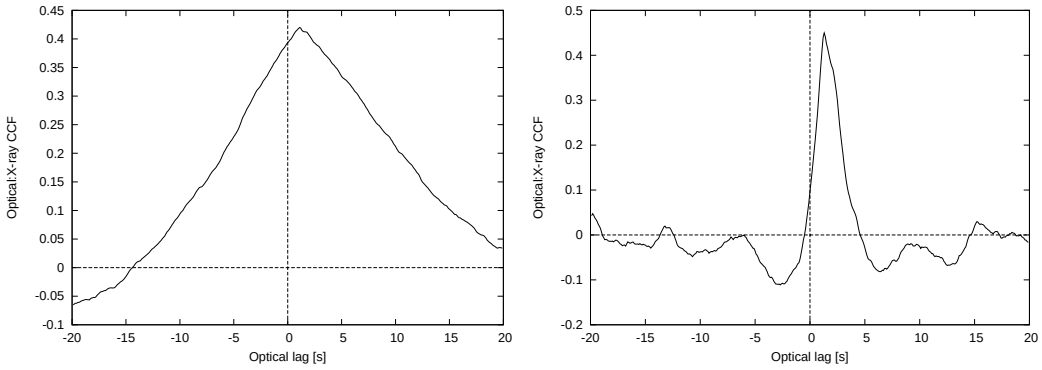

Figure 4.19: Left figure: The optical/X-ray(simulated) cross-correlation when Γ_{sh} is modelled with a 0.1 Hz Lorentzian and M_{sh} with a 0.01 Hz Lorentzian Right figure: The optical/X-ray(simulated) cross-correlation periodogram when M_{sh} is modelled with a 0.1 Hz Lorentzian and Γ_{sh} with a 0.01 Hz Lorentzian

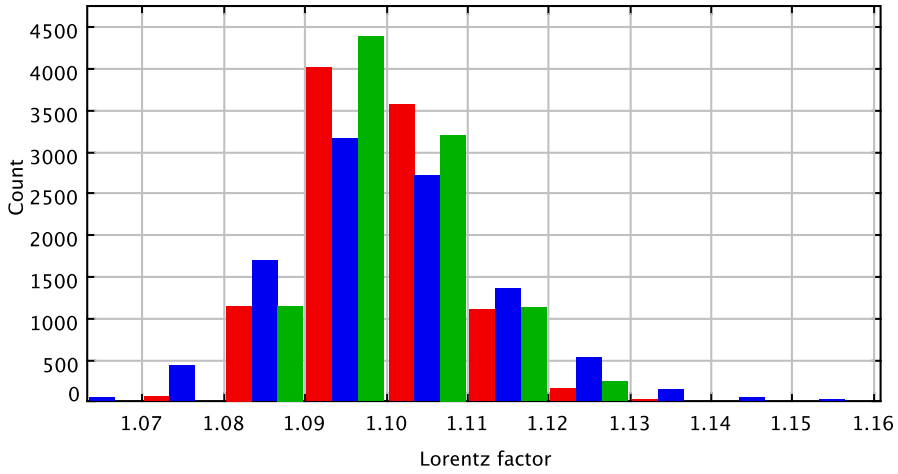

Figure 4.20: A Histogram of the Lorentz factors for the simulations presented above. The histogram shows how the Lorentz factor distribution changes with different power-spectral models. Red: Γ = 0.1 Hz + 0.01 Hz, M = constant; blue: Γ = 0.1 Hz, M = 0.1 Hz; green: Γ = 0.01 Hz, M = 0.1 Hz. The frequencies correspond to the Lorentzian frequencies used in the PDS modelling.

mass is varying rapidly, the correlations that are remarkably similar to the observed ones can be reproduced.

4.4 Discussion

The results in this chapter show an array of correlations and behaviours. Only the relatively simple cases were presented to show the complexity of the relationships between the jet parameters and the output light curves.

Before discussing further the various correlations presented in the previous section, it is important to look at the parameters that give rise to these results. Figures 4.20 and 4.21 show the bulk Lorentz factor distribution when different power-spectral models are used to generate the time-series; figures 4.22 and 4.23 show the distributions for the shell mass. The main point is to illustrate how the distribution of these parameters can be very different depending on our choice of the power-spectral model. This therefore leads to the differences observed in the CCF and the light curves presented in the previous section.

When no shell collisions are modelled, there is a very simple correlation between the optical output and the mass time series, which is a strong symmetric correlation with a positive lag. This lag, and others in the more complex scenarios, are a combination of the “artificial” lag introduced by the first-shock position and the “natural” lag which is the time interval for the shell emission to peak at the relevant observed frequency. (The longitudinal expansion was suppressed in this particular scenario to avoid the shell boundaries coming in contact each

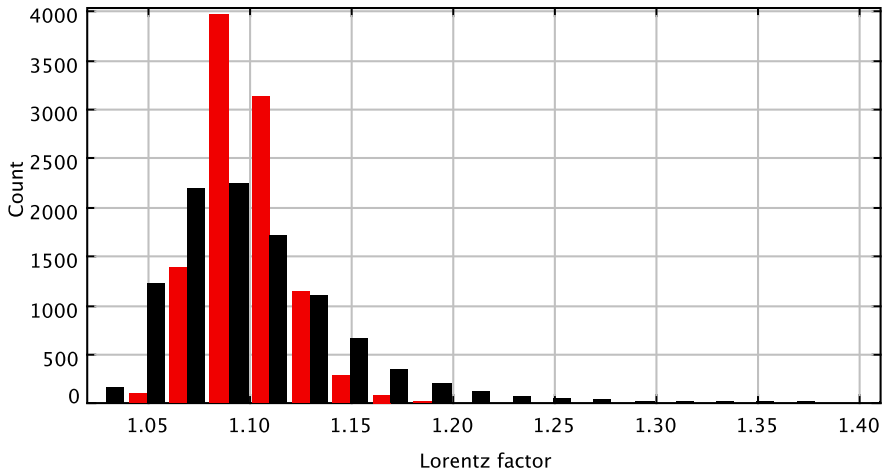

Figure 4.21: A Histogram of the Lorentz factors time-series generated using a broken power-law (black) and a double Lorentzian (0.1 Hz + 0.01 Hz; red).

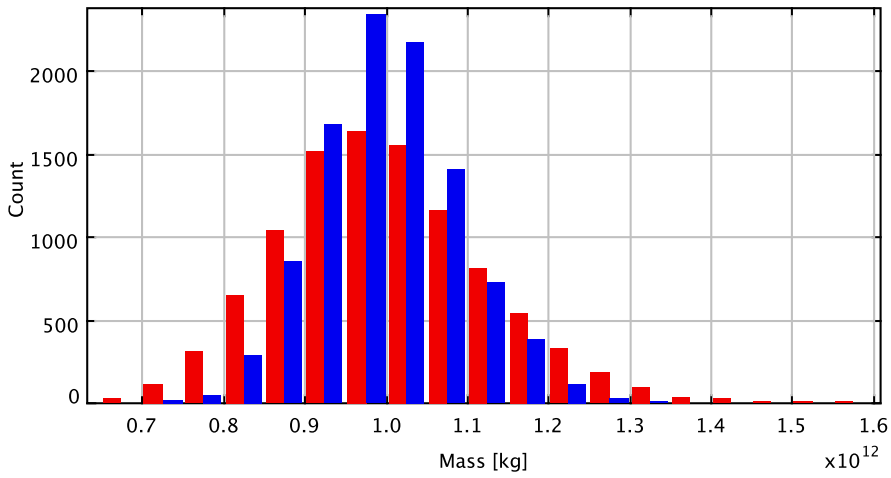

Figure 4.22: A Histogram of the shell mass when generated with separate Lorentzians affecting the shell mass and the Lorentz factors. Blue: Γ = 0.01 Hz, M = 0.1 Hz; red: Γ = 0.1 Hz, M = 0.01 Hz. The frequencies correspond to the Lorentzians frequencies used in the PDS modelling.

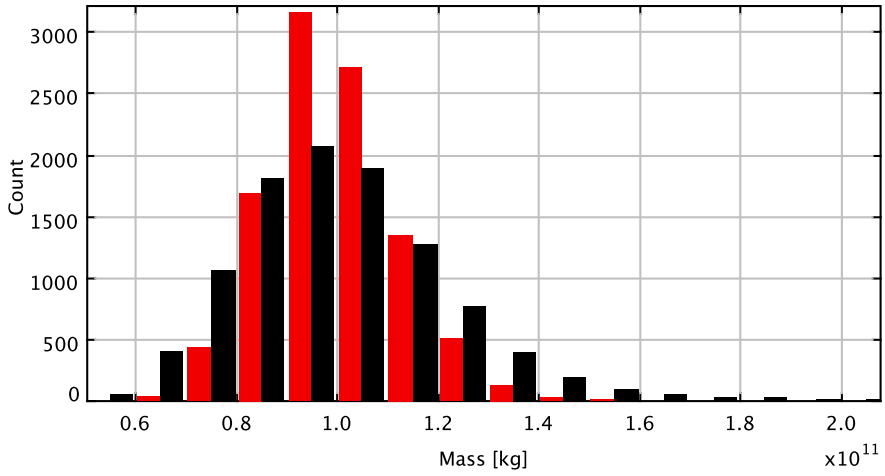

Figure 4.23: A Histogram of the shell masses for the simulations presented above. The histogram shows how the shell mass distribution changes with different power-spectral models. Black: M, Γ = broken power-law; red: M, Γ = 0.1 Hz + 0.01 Hz.

other.) If one considers the X-ray variability to be the direct analogy for the accretion rate (M_{sh} in our case), then this lag offers a simple explanation for the optical emission lagging the X-ray in the X-ray binaries observations. The optical/X-ray correlations, however, are very different from the ones seen in the case of no-collisions set-up. This therefore suggests more levels of complexity, hence the shell collisions were explored.

The optical-Γ_{sh} CCF, in which the shell bulk Lorentz factor is varying (modelled with 0.1 Hz and 0.01 Hz Lorentzians) whilst the shell mass is kept constant, shows that the shell collisions bring this added complexity to these correlations. The correlation also shows a relatively sharp positive-lag peak and then a sharp anti-correlation drop. The anti-correlation is caused by the added time-scales in the optical emission due to the large number of collisions taking place. This anti-correlation can also be seen when both the mass and the bulk Lorentz factors vary together. However, when the shell mass is also varying, the main bulk of the collisions are localized to the inner parts of the jet. This gives rise to the CCF being quite different whether one looks at the entire jet or only the inner radii. On the other hand, when only the Γ_{sh} is varying (shell mass kept constant) the average collision radius is larger, so the anti-correlation can be observed even when the light curve from the entire jet is used. This is good evidence for the shell collisions being responsible for the anti-correlation observed.

The picture unfortunately is not that straightforward. Even though we see glimpses of *the rate of change* of the X-ray (M_{sh} and Γ_{sh}) affecting the jet power (optical output), as observed in XTE J1118+480 (Malzac *et al.*, 2004), the shell parameters such as the longitudinal expansion rate also have a significant part to play: higher shell mass means a higher expansion rate, thus more collisions at smaller radii. Various parameters can be altered (for example, the bulk Lorentz factor), so that the collisions take place at larger radii, but this does not result in the

kind of correlations that are observed: the positive correlation lag would remain relatively fixed, but the anti-correlation lag times would increase.

When CCFs (in the two Lorentzian and the broken power-law case) are compared with the optical/X-ray CCF for XTE J1118+480, the most striking element missing is the pre-cognition dip. In fact the CCF obtained using *i*Shocks are a mirror image of the ones obtained from XTE J1118+480. This, however, is quite an exciting result — if one looks at the CCFs from the source GX 339-4. Although the *i*Shocks parameters used here are for XTE J1118+480, we can glimpse into the underlying physical processes by comparing the results with GX 339-4.

The cross-correlation functions from GX 339-4 also show a pre-cognition dip, plus another dip after the positive lag peak. The pre-cognition dip remains unreproducible here, but the slow rise and the sharp drop after the positive lag is reproduced almost perfectly. The question then is why are there different correlations from these two sources? One would expect the same processes to give rise to these data, no matter what X-ray binary source.

The answer may be that the pre-cognition dips, the slow rise/decay of the positive lag, and the presence/lack of the post positive lag dip are actually different components that combine to give the impression of a single highly complex relationship. Spruit and Kanbach (2002) conducted a principle component analysis of the X-ray and the optical variability in XTE J1118+480 and found a number of these very different underlying components giving rise to the overall relationship. They were unable to offer a physical interpretation of these components, however. It is therefore possible that the results here are pointing towards a picture where the shell parameters' influence gives rise to the different components of the overall correlations. For example, we have shown that the collisions can give rise to the anti-correlation, whilst the mass leads to a simple positive correlation: the simulation where M_{sh} and Γ_{sh} were modelled using different frequency Lorentzians, this kind of picture arose. The bulk Lorentz factor were showing a strong anti-correlation while the mass produced a strong positive correlation. The combination of these two, however, can produce a much more complex correlation. So the difference in these sources' correlations could simply be due to the slightly different combination of these parameters.

The separate Lorentzian modelling of M_{sh} and Γ_{sh} shown above is one of the first attempts in the physical modelling of the disc:power-law variability results. Wilkinson and Uttley (2009) have found that the disc component could in fact be the driving force behind the variability in the hard state. Although the simulations presented here were a rather naive interpretation of this kind of variability, our results have opened up a large avenue for exploration: the disc variability can be used to model the optical (from the jet) variability and then the comparisons made with the power-law components. The pre-cognition dip may be a by product of the X-ray power-law component lagging the soft X-ray component, whilst the optical is also driven by the soft X-ray component. Thus, any correlations between the power-law and the optical would give the illusion of the optical being "aware" of the X-ray changes *before* they are manifested.

In terms of the optical light curves presented here, they have gone a long way in explaining some of the optical/X-ray data. The optical power-spectra have generally been found to be

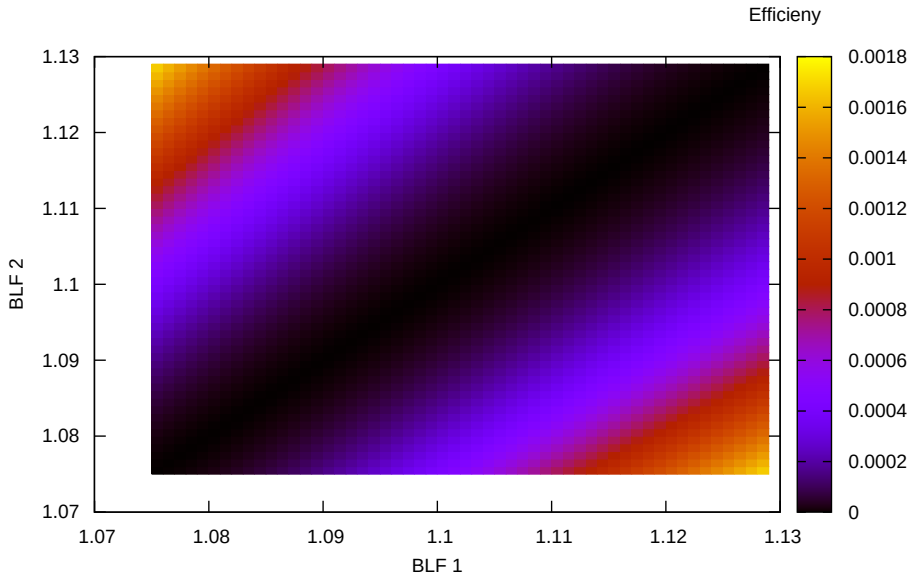

Figure 4.24: The map shows how the shell merger efficiency as a function of colliding shells BLFs. The BLF range is the kind of range used for investigating the jet timing properties.

flatter than the X-ray (M_{sh} and/or Γ_{sh}) power-spectra. This has been as a result of the additional time-scales brought in by the shell collisions. These data, plus the broad QPOs seen in the optical for both the two-Lorentzian case and the broken power-law case are in agreement with the observations of the XRBs (Gandhi, 2009). This has once again, re-enforced the case for further exploration of this field in the context of *i*Shocks set-up, which may ultimately help to explain the optical/X-ray correlations.

4.4.1 A note on merger efficiency

Figure 4.24 shows the merger efficiency as a function of the colliding shells BLF. It is clear that when the difference in Γ is small, the efficiency is also very low. So if the shells are injected with $\approx 1\%$ internal energy, that is a significant amount of energy when compared with the amount of energy generated in a collision. Therefore, as mentioned previous in the previous chapter, E_{frac} is a free parameter that requires further attention to minimize its impact on the results.

4.5 Conclusions

This chapter has been an investigation into understanding the optical/X-ray correlations in the X-ray binaries from a more physical point of view. An attempt has been made to connect the X-ray light curve properties with the jet parameters. The results obtained show that quite a complex combination of parameters would give rise to the kind of optical/X-ray correlations

observed in XTE J1118+480 and GX 339-4.

Some extremely exciting results were seen which, for the first time, hint at the physical origin of the variability observed. Even though not all the observed correlations could be reproduced, the results obtained offer quite a few possible routes for any future work. The outcomes have shown that there is an extremely good possibility to reproduce quantitatively the variability observations with a few modifications to the model and to the time series generation process. The results in this chapter have shown that even with an extensive research into how the X-ray light curve properties can be used to generate the shell properties, there are still numerous combinations possible when it comes to the shell mass and the bulk Lorentz factor generation. Some of the key results have hinted at the possibility of using the disc as the driving force for the variability rather than the generally assumed power-law component in the hard state.

Constraining the simulation parameters would make any resultant correlation much stronger. For example, the effects of the thermal longitudinal expansion on the collisions rate must be dis-entangled from the bulk Lorentz factor effects. This means that the "inherent" timing properties of the model (injection rate, thermal expansion influence on the collision times) must be subtracted from the results. Observationally constraining the simulation parameters would improve the results further. For example, using the accretion rate and efficiency (among other possibilities) to derive the shell mass and the shell bulk Lorentz factor may provide a more physical connection between the disc and the jet. Overall, *i*Shocks gives us a great springboard for the future work in this field by showing us that even the first order combination of the jet physics with its timing properties can reproduce some of the most enigmatic observations.

5

Electron-positron pair processes

The following chapter outlines the electron-positron pair annihilation implementation in the High Energy Astrophysical Radiative transfer (HEART) code. The HEART code functionality is also described to put the electron-positron related processes in context.

5.1 The corona

Thus far the focus of the present work has been on the jets emanating from BHXBs, plus the disc:jet connection. The optical/X-ray correlations, already mentioned, are influenced heavily by the power-law component of the spectrum, which has also necessitated the existence of a corona.

Although the geometry of the corona is unknown, its effects on the spectrum are well studied. It is a region where the high energy particles (chiefly assumed to be electrons/positrons), up-scatter the low energy photons from the disc via Compton scattering. A number of geometries have been suggested for the corona. These range from the Advection Dominated Accretion Flow (ADAF), where the inner optically-thick (geometrically thin) part of disc is replaced by this optically thin and geometrically thick flow (e.g. see Esin *et al.*, 1997), to the base of the jet giving rise to the high energy X-rays (e.g. see Markoff *et al.*, 2001. We adopt a slightly different configuration (see Liang and Price, 1977) in the following work: the corona is assumed to sandwich the accretion disc. The soft (low energy) photons have to therefore travel through the corona, thus getting up-scattered to give rise to high energy component of the spectrum.

Such a corona is generally assumed to contain an electron population that is responsible for

all the scattering processes. However, one would expect positrons to be present as well, if the pair production is active. The presence of both electrons and positrons would inevitably lead to certain amount of pair annihilation, which is the subject of the study here.

5.2 Electron-positron pair annihilation

For a long while, there has been evidence of an annihilation line from the Galactic Centre. It was first measured via balloon borne experiments using NaI scintillators (Johnson III *et al.*, 1972) and put the line at 476 ± 26 keV, making the interpretation difficult. However, another balloon borne experiment, this time using germanium detectors, put the line at 511 keV with only a few keV width (Leventhal *et al.*, 1978). Some of the initial experiments observed variations in the Galactic Centre annihilation line; hence, it was suggested that the annihilation line is time-variable (Riegler *et al.*, 1981; Paciesas *et al.*, 1982; Leventhal *et al.*, 1982, 1986). The more extensive measurements, however, showed no evidence of such variability (Share *et al.*, 1988; Gehrels *et al.*, 1991; Leventhal *et al.*, 1993; Mahoney *et al.*, 1994; Teegarden *et al.*, 1996; Purcell *et al.*, 1997; Harris *et al.*, 1998; Churazov *et al.*, 2005). This distinct and quite strong annihilation line from the Galactic Centre is shown in figure 5.1 (Churazov *et al.*, 2005). Even though there is a clear detection of the annihilation line from the Galactic Centre, its origin is still not clear. It is mainly the origin of the positrons, that could be annihilating with the interstellar electrons in the Galactic Centre, which is unknown. (Weidenspointner *et al.*, 2008).

A number of suggestions have been made as to the origin of the Galactic Centre positrons. These include (Cassé *et al.*, 2004; Teegarden and Watanabe, 2006; plus references therein):

Nucleosynthesis in massive stars: Wolf-Rayet (W-R) stars are massive stars with strong stellar winds. Various radioactive elements, created in the cores of the massive stars, can be convected to the surface and carried into the interstellar medium (ISM) via the stellar winds. These radioactive elements can subsequently undergo β^+ decay, thus producing positrons.

Novae (DNe): A "classical" nova is as a result of burning the built up accreted material on the surface of a white dwarf. These thermonuclear reactions result in the production of unstable isotopes that will emit positrons via β^+ decay. This will therefore result in an annihilation signature from the classical nova as well. However, such a signal will be short lived due to the nature and the density of the elements decaying.

Gamma-ray burst (GRB): Although the mechanism behind gamma-ray bursts is not fully understood, there have been suggestions that with the presence of high energy photons, photon-photon pair production could be taking place and adding to the galactic positron population.

Supernovae (SNe): During the explosive reaction of a supernova, a variety of radioactive elements are produced. The decay of these radioactive elements can produce positrons for annihilation with the ISM electrons.

Cosmic-ray interactions: Cosmic rays can undergo a number of interactions with the interstellar medium that can result in a radioactive nuclei. The subsequent radioactive decay of

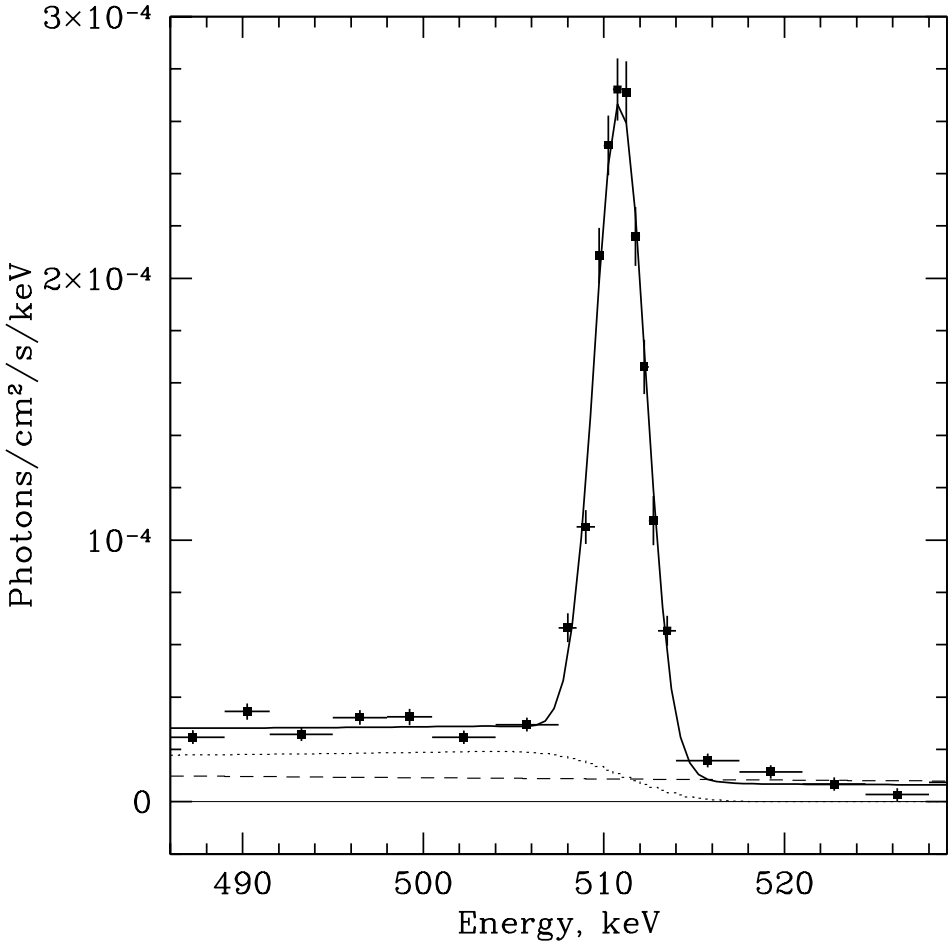

Figure 5.1: The annihilation line from the Galactic Centre detected using SPI onboard the INTEGRAL gamma ray observatory. The image is from Churazov *et al.* (2005).

these nuclei emits positrons.

Pulsars: Electron-positron pairs may be created by vacuum pair production in the strong magnetic fields in the pulsar magnetosphere. The produced high energy positrons can escape and travel far from the source.

Low mass X-ray binaries (LMXRBs): The jets emanating from LMXRBs are believed to be leptonic in nature, thus adding to the galactic positron population. It may also be possible to produce pairs in the corona of these systems. Also, there have been suggestions of an asymmetry in the annihilation line distribution from the galactic bulge which can be correlated with the asymmetry in the X-ray binary distribution(Weidenspointner *et al.*, 2008). To know whether this correlation is also causation, it is important to see if these LMXRBs have an individual annihilation signature.

There is, however, a paucity of evidence for such a signature from an X-ray binary. The two most well know examples of an annihilation signature from a compact source are the “Great

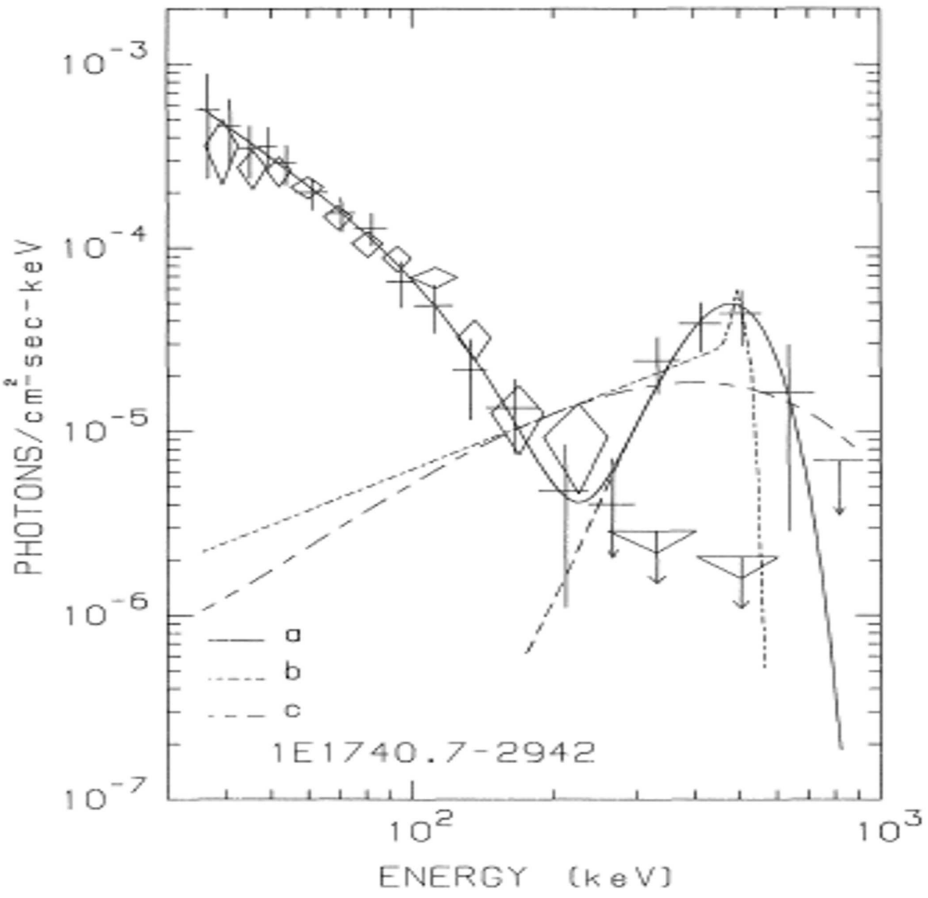

Figure 5.2: The annihilation line from the Great Annihilator, 1E1740.7–2942. The image is from Bouchet *et al.* (1991).

Annihilator" 1E1740.7–2942 (Gilfanov *et al.*, 1991)and the "Nova Muscae 1991" GRS 1124–684 (Bouchet *et al.*, 1991); the annihilation line observations are shown in figures 5.3 and 5.2. There also hints of an annihilation line from Cygnus X-1 (Ling and Wheaton, 1989).

With the focus of the present work on X-ray binaries, an effort shall be made to understand the physics behind the annihilation signature, or lack thereof, from these systems. There is a broad consensus on the black hole systems being very similar and simply scaled by mass. Therefore if the origins of the galactic annihilation line are linked to the central massive black hole, then it is even more important to understand why, thus far, there are no clear detections of such a line from the X-ray binaries. A number of processes, such as thermal line broadening (Svensson, 1982), can not only reduce the annihilation line strength, but also change its appearance, making it difficult to detect.

5.3 The HEART code

The HEART code (Collins, 2004) was designed to model the transfer of photons in what is commonly referred to as the 'corona' in an X-ray binary system. The exact nature of this corona is

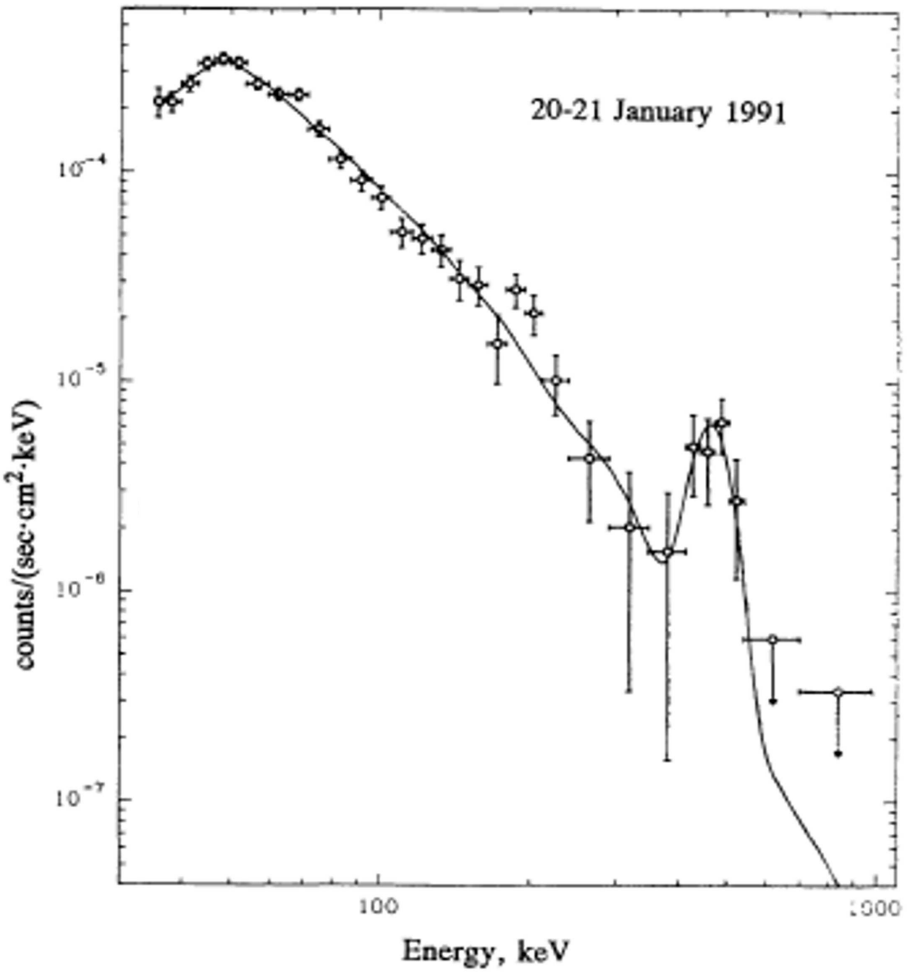

Figure 5.3: The annihilation line from nova muscae. The image is from Gilfanov *et al.* (1991).

hitherto unknown, but it is considered to be a Comptonizing region. The corona can be envisaged as a hot plasma, comprising electrons and positrons, sitting above a cooler accretion disc. The disc radiates the blackbody photons, which are injected into the hot coronal plasma. The corona then reprocesses these low energy, soft, photons into high energy, hard, photons. The corona not only reprocesses the soft photons from the disc, but it can also have intrinsic photon emission from processes such as bremsstrahlung radiation. In HEART the corona can have an arbitrary geometry . A number of photon-electron interactions are modelled: Compton scattering, inverse Compton scattering, bremsstrahlung, and Coulomb interactions. The HEART code originally did not model a positron distribution nor any process associated with the presence of both electrons and positrons. The following HEART code description is kept brief and only the points most salient to the electron-positron processes are covered. An in-depth discussion of the code's other functionalities can be found in Collins (2004) and Rogers (2008).

5.3.1 Corona structure in HEART

The HEART code models the corona using cubic cells; practically any 3D shape can be approximated using these cells. To save computation time only the shapes that have at least one plane of symmetry are modelled; with little known about its true nature, the corona is assumed to be spherical. With the symmetrical nature of this assumed sphere, only the hemisphere above the accretion disc need be modelled.

All the cells are linked such that a cell is able to transfer photons[1] to its neighbours. Once the desired 3D shape is achieved, using the cell structure, the electron distributions are added to each cell. The electron/positron[2] populations are confined to each cell, but they can 'evolve' within that volume.

The accretion disc injects blackbody photons into the base of the corona. The bottom face of the cells adjacent to the disc receives the photons and then scatter them into six directions . The "six directions" are the six faces of the cubic cell; the photons can travel only the directions perpendicular to a cell face. Each cell behaves the same way; i.e., the photons received from one face are scattered equally in six directions. Compton scattering is the main source of photon scattering in the cells. It was assumed that the dominant scattering direction is the direction of motion of the electron. Therefore an isotropic electron distribution will lead to an isotropic photon distribution (Collins, 2004). Strictly speaking, however, this is not correct: this is discussed further in section 5.3.4.

The photon and lepton energy distributions are discretized in the form of logarithmic energy bins. For the lepton energy distributions, each bin contains information regarding the number of particles so that we are able to model power-law, thermal or any arbitrary distribution. The photon energy distribution is also discretized similarly to the leptons, except in the case of photons, it is the intensity in each bin that represents the number of photons at that energy.

All the modelled radiative processes are calculated at each time step, where a time step is the light crossing time for one cell:

$$\text{time-step} = \frac{\text{width of cell}}{c} \, . \tag{5.1}$$

That is, a photon not interacting with the electrons will cross a single cell in exactly one time step. As a matter of design, photons can interact only once in a single cell. In order for this approximation to be valid, the optical depth of any one cell needs to be much less than unity. A high optical depth corona therefore needs to be modelled using multiple cells.

[1] In the HEART code only the photons move across the cells. The lepton populations are confined to individual cells.

[2] As we shall note later, the positron distributions added to the code are treated identically to the electron distributions.

5.3.2 Radiative processes

Some of the key radiative processes modelled in the HEART code are outlined below. These include bremsstrahlung radiation, and Compton scattering. The radiative transfer modelling is based on the principles of detailed balance for each process (Rybicki and Lightman, 1979) . We can start by looking at the general radiative transfer principles and develop them for specific processes. The radiative transfer is a combination of emission and absorption. So if we examine single particle emissivity first , we have:

$$j_\nu = \frac{\mathrm{d}E}{\mathrm{d}t\mathrm{d}\nu} = h\nu n_{ip} v \sigma_\nu \ , \tag{5.2}$$

where h is the Planck's constant; ν is the frequency; n_{ip} is the number of interacting particles; E is the energy; v is the speed of the particles; and σ_ν is the interaction cross-section. The emission coefficient , ε, is then given by:

$$\varepsilon = \frac{\mathrm{d}E}{\mathrm{d}\nu \mathrm{d}V \mathrm{d}\Omega} = \frac{1}{4\pi} \int j_\nu n_\gamma \mathrm{d}\gamma \ , \tag{5.3}$$

where n_γ is the number density of the particles with energy $\gamma m_e c^2$; V is the volume; and Ω is the solid angle. Now, the absorption coefficient can be expressed as:

$$\kappa_\nu = \int n_\gamma \sigma_\nu \mathrm{d}\gamma \ . \tag{5.4}$$

Using the above two coefficients the following relation for the intensity can be obtained:

$$I_\nu(\tau_\nu) = S_\nu (1 - e^{-\tau_\nu}) \ , \tag{5.5}$$

where $S_\nu = \varepsilon_\nu / \kappa_\nu$ is the source function , and τ_ν is the optical depth (=$\kappa_\nu \times$length); *length* refers to the distance photons travel in the absorbing medium. The absorption and the emission coefficients can therefore be calculated for each of the radiative processes. Equation 5.5 can then be used to calculate the changes to the photon distribution in each cell.

5.3.2.1 Bremsstrahlung

The bremsstrahlung radiation is emitted by the electrons (or positrons) due to acceleration in the presence of another charged particle. In HEART only the electron-electron and positron-positron bremsstrahlung are taken into account; no other charged particles are modelled in the corona. The electron-positron bremsstrahlung is omitted and its implications are discussed later. Using the techniques outlined in section 5.3.2 and equation 5.5 we can calculate the emission associated with the bremsstrahlung radiation in each cell and at every time step. In order to make the calculations easier, the bremsstrahlung cross sections, as with many radiative processes, are derived in various limiting cases. In HEART, the bremsstrahlung is calcu-

lated for the mildly relativistic ($\gamma < 2$) electrons/positrons and the ultra-relativistic [3] ($\gamma \geq 2$) electrons/positrons. The bremsstrahlung emissivity, $j_{\nu,mr}$, for the mildly relativistic electrons interacting with other mildly relativistic electrons is found to be:

$$j_{\nu,mr}(\gamma) = h\nu c n_{e,mr}\sigma_{\nu,mr}(\gamma) \ . \tag{5.6}$$

The emissivity for the ultra-relativistic electrons interacting with other ultra-relativistic electron, in addition to the mildly relativistic electrons, is given by:

$$j_{\nu,mr}(\gamma) = h\nu c(n_{e,mr} + 2n_{e,ur})\sigma_{\nu,mr}(\gamma) \ , \tag{5.7}$$

which shows that the emission from the ultra-relativistic electrons interacting with other ultra-relativistic electrons is twice as large as that from their interaction with the mildly relativistic electrons (Zdziarski *et al.* (1990)). Using equations 5.3 and 5.4 the emission and the absorption coefficients are:

$$\begin{aligned} \varepsilon_\nu &= \frac{h\nu c}{4\pi\sigma_T l}\left[\tau_{T,mr}\int_1^{\gamma_{ur}} n_\gamma \sigma_{\nu,mr}\mathrm{d}\gamma \right. \\ &\left. +(\tau_{T,mr}+2\tau_{T,ur})\int_{\gamma_{ur}}^{\gamma_{max}} n_\gamma\sigma_{\nu,ur}\mathrm{d}\gamma\right] \end{aligned} \tag{5.8}$$

and

$$\begin{aligned} \kappa_\nu &= \frac{hc}{8\pi m_e\sigma_T l\nu}\left[\tau_{T,mr}\int_1^{\gamma_{ur}} \frac{n_\gamma}{\gamma p}\frac{\mathrm{d}}{\mathrm{d}\gamma}(\gamma p\sigma_{\nu,mr})\mathrm{d}\gamma \right. \\ &\left. +(\tau_{T,mr}+2\tau_{T,ur})\int_{\gamma_{ur}}^{\gamma_{max}} \frac{n_\gamma}{\gamma p}\frac{\mathrm{d}}{\mathrm{d}\gamma}(\gamma p\sigma_{\nu,ur})\mathrm{d}\gamma\right] \ . \end{aligned} \tag{5.9}$$

The interaction cross-sections for the mildly relativistic regime, $\sigma_{\nu,mr}$, and for the ultra relativistic regime, $\sigma_{\nu,ur}$, can be found in Gould (1980) and Zdziarski *et al.* (1990) respectively.

$$\begin{aligned} \sigma_{\nu,mr}(\gamma) &= \frac{\alpha_f\sigma_T}{10\pi\nu}\left\{\zeta\left[20-6\frac{1+\zeta^4}{(1+\zeta^2)^2}\right]+\ln\left(\frac{1+\zeta}{1-\zeta}\right)\times \right. \\ &\left. \left[6(1+\zeta^2)-\frac{7(1-\zeta^4)^2+3(1-\zeta^2)^4}{2(1+\zeta^2)^3}\right]\right\} \ , \end{aligned} \tag{5.10}$$

$$\sigma_{\nu,ur}(\gamma) = \frac{3\alpha_f\sigma_T}{2\pi\nu}\zeta\left(\zeta+\frac{1}{\zeta}-\frac{2}{3}\right)\left(\ln\left(\frac{2\gamma^2\zeta}{1-\zeta}\right)-\frac{1}{2}\right) \ , \tag{5.11}$$

where α_f is the fine structure constant and $\zeta = 1-(h\nu)/(\gamma m_e c^2)$. The contributions from the non-relativistic electrons is negligible in the frequency range being modelled; thus, not taken into account here.

[3] when $\gamma = 2$ the kinetic energy of electron = rest mass energy; at $\gamma \geq 2$ the kinetic energy is dominant.

5.3.2.2 Compton scattering

In the HEART code the photons can also undergo Compton scatterings. As mentioned in section 5.3.1, any given cell's optical depth must remain much lower than unity. The cells therefore have to be modelled in such way that a single cell is optically thin ($\tau << 1$) and the following relation applies

$$I_\nu = l\varepsilon_\nu \ , \tag{5.12}$$

where l is the distance travelled by the photon. The above relation is true also because there is no absorption process associated with the Compton scattering. The optical depth requirements are put in place because the HEART code can model only a single photon scattering per time step per cell. This does put constraints on the overall optical depth for the corona that can be modelled. To model high optical depths, a large number of cells are required, increasing the computation times considerably (discussed in 5.3.4).

All the photons present in the cell at the start of the time-step (*seed photons*) are scattered from frequency ν_0 to frequency ν_1 in a cell of width w. The scattered photon distribution is given by:

$$I_{\nu_1} = w\int_{\nu_{0,min}}^{\nu_{0,max}}\int_{\gamma_{min}}^{\gamma_{max}} n_\gamma x F_C(x)\mathrm{d}\gamma I_{\nu_0}\frac{\mathrm{d}\nu_0}{\nu_0} \ . \tag{5.13}$$

The loss to the seed photons is taken into account by subtracting the integrated total contribution over all scattered frequencies, ν_1, from each seed frequency,ν_0:

$$I'_{\nu_0} = I_{\nu_0} - w\int_{\nu_{1,min}}^{\nu_{1,max}}\int_{\gamma_{min}}^{\gamma_{max}} n_\gamma x F_C(x)\mathrm{d}\gamma I_{\nu_0}\frac{\mathrm{d}\nu_1}{\nu_1} \ . \tag{5.14}$$

In the context of equation 5.5 and 5.12 the emission coefficient is:

$$\varepsilon_{\nu_1} = \int_{\nu_{0,min}}^{\nu_{0,max}}\int_{\gamma_{min}}^{\gamma_{max}} n_\gamma x F_C(x)\mathrm{d}\gamma I_{\nu_0}\frac{\mathrm{d}\nu_0}{\nu_0} \ , \tag{5.15}$$

where $x = \nu_1/(4\gamma^2\nu_0)$ and $xFc(x)$ is the photon redistribution function. $xFc(x)$ is calculated for three different cases:

1. $\gamma < 10$ electrons interacting with high energy photons ($k > 10^{-2}$).
2. $\gamma < 10$ electrons interacting with low energy photons ($k \leq 10^{-2}$)
3. electrons with $\gamma \geq 10$.

where $k = \gamma h\nu_0/(m_e c^2)$. The photon redistribution function can be found in appendix B. It should be noted that the photons are scattered evenly in six directions available for a cubic cell (further discussed in 5.3.4).

5.3.3 Electron/Positron distributions

In Collins (2004) version of HEART the plasma is assumed to be composed purely of electrons. One of my first additions to the code was to insert the capability to model the positron populations as well. The positrons are treated identically, in terms of the energy distributions, to the electrons in the code . This includes all the radiative processes, outlined already, that the electrons are involved in.

In HEART, with the energy distribution discretization, it is possible to model any arbitrary lepton energy distribution. Our main focus is on the thermal, the power-law, and a hybrid of these two energy distributions. The thermal distribution can be described by the following Maxwell-Boltzmann equation (in the relativistic form):

$$n_\gamma = \frac{n_e}{\Theta_e K_2(1/\Theta_e)} \gamma p e^{-\gamma/\Theta_e}, \tag{5.16}$$

where n_γ is the number density of the leptons at energy γ; K_2 is the modified Bessel function of order 2; $\Theta_e = kT_e/m_e c^2$ is a dimensionless relativistic temperature associated with the lepton distribution. The lepton energy is measured in terms of the Lorentz factors, γ - this is a measure of the particle energy energy as fraction of its rest mass energy $m_e c^2$. Integrating equation 5.16 over all the energies gives the total number density of e^-/e^+ , $n_e[\mathrm{m}^{-3}]$.

The power-law distribution, ranging from γ_{min} to γ_{max}, is modelled by:

$$n_\gamma = n_0 \gamma^{-q} \tag{5.17}$$

where $n_0 = n_e(q-1)[\mathrm{m}^{-3}]$ is the normalization factor and q is the power-law index. The power-law index is assumed to be in the range: 2 to 2.25.

5.3.4 Limitations of the HEART code

Rogers (2008) has already outlined in detail some of the limitations of the HEART code . I shall re-iterate some of the findings here and re-examine these limits in the context of the present work.

As mentioned earlier, a variety of radiative processes are implemented in the HEART code. The cell structure, however, puts certain constraints on some of the implementations. If we look at the Compton and the inverse Compton scattering, then the cubic cell structure requires the photons to travel in six directions only, using the assumption of isotropic photon scattering. An isotropic lepton distribution is assumed to scatter the photons isotropically (Collins, 2004). This approximation might be valid for a very limited case where the electron energy is much greater than the photon energy (the inverse Compton scattering angle is energy dependent); if, however, the photon energy becomes comparable to or greater than the typical electron energies, the photons scattering direction becomes a more complicated function of the lepton and photon energies, plus their direction of travel. It might be possible to have an initial isotropic scattering of the low energy disc photons by the high energy leptons, but with each

scattering the photons will gain energy and the isotropic scattering assumption becomes invalid very quickly. A more comprehensive implementation of Compton scattering should take these limitations into account .

Any single cell in HEART must be optically thin. This means that in order to model the high optical depth coronae, a large number of cells are required. With the increase in cell numbers, the computation time increases considerably. Rogers (2008) compared in great detail the HEART code performance against other available Comptonization codes. The HEARTcode was able to perform fairly well for the optically thin regimes, but lagged behind the competing simpler models when it came to the optically thick regimes.

The modelling of the lepton energy distributions in HEART also requires a brief discussion. In order to avoid all the leptons in the corona cooling down very rapidly, a heating mechanism is required to maintain a certain temperature. Currently in HEART, there is no direct mechanism for heating the leptons. Instead, the lowest energy leptons can be removed, to avoid a pile up at the lowest energy bin, from a cell and the high energy leptons are injected to replace them. The lepton energy distributions can therefore be allowed to *evolve* by cooling the high energy e^-/e^+. Of course, a balance of the number of leptons removed and replaced would be necessary to maintain a certain type of distribution. It is also essential that effort is made to conserve the lepton number under such *dynamic* scenario; however, this is prone to problems as the fluctuations in the lepton numbers are easily overlooked; changing the lepton density changes the optical depth. In fact, with such a set up the biggest cause for concern is the fact that energy conservation cannot be ensured if the leptons are being removed and added arbitrarily. .

In order to avoid such errors and further complications, a *steady-state* model is used for the purposes of the present work. With a steady-state scenario, the lepton distributions are kept constant. In effect, such a simulation assumes an infinite energy reservoir constantly replenishing the lepton distribution; however unrealistic, this assumption is necessary to have a "simple" model for demonstrating other physical processes.

5.4 Pair annihilation in HEART

In HEART, the Svensson (1982) treatment is followed to calculate the annihilation spectrum. The annihilation emissivity, $\dot{n}(k)dk$, for the isotropic lepton distributions is given by:

$$\begin{aligned}\dot{n}(k)\mathrm{d}k &= n_+ n_- \int \mathrm{d}\gamma_+ f_+(\gamma_+) \int \mathrm{d}\gamma_- f_-(\gamma_-) \\ &\quad \int \frac{\mathrm{d}\mu}{2} \frac{\gamma_{cm}^2}{\gamma_+\gamma_-} 2\beta_{cm} c \frac{\mathrm{d}\sigma}{\mathrm{d}k}(k,\gamma_+,\gamma_-,\mu)\mathrm{d}k \,, \end{aligned} \tag{5.18}$$

where

$$\gamma_{cm} = \sqrt{\frac{\gamma_+\gamma_-(1-\beta_+\beta_-\mu)+1}{2}} \,. \tag{5.19}$$

and $\mu = cos\theta$ and θ is the interaction angle between the electron and the positron; $f_{\pm}(\gamma_{\pm})$ are the positron and the electron distribution functions. As mentioned in section 5.3.3, the electron and positron energy distributions are discretized logarithmically according to the particle energy (γ). Each energy bin contains the information regarding the number of electrons/positrons at that energy. The discrete energy distribution simplifies matters and gives the emissivity per photon energy ($k = h\nu/mc^2$):

$$\dot{n}(k) = n(\gamma_+)n(\gamma_-)\int \frac{\mathrm{d}\mu}{2}\frac{\gamma_{cm}^2}{\gamma_+\gamma_-}2\beta_{cm}c\frac{\mathrm{d}\sigma}{\mathrm{d}k}(j,\gamma_+,\gamma_-,\mu)\mathrm{d}k\,, \tag{5.20}$$

where $n(\gamma_{-/+})$ is the number density of the electrons/positrons at energy γ. Equation 5.20 can be averaged over all interaction angles to give an angle averaged emissivity for the pair annihilation. The interaction cross section, $\mathrm{d}\sigma/\mathrm{d}k$, is given by:

$$\frac{\mathrm{d}\sigma}{\mathrm{d}k} = r_e^2\frac{1}{4\beta_{cm}\gamma_{cm}^3}\pi\left[\frac{-4\gamma_{cm}}{((\gamma_+ + \gamma_-)^2 - 4\gamma_c m^2)^{1/2}} + G_+ + G_-\right]\,, \tag{5.21}$$

where

$$G_{\pm} = \left(2\gamma_{cm}^2 + 2 - \frac{1}{\gamma_{cm}^2}\right)\frac{1}{u_{\pm}} + \frac{1}{2}\left(2\gamma_{cm}^2 - d_{\pm}\right)\frac{1}{u_{\pm}^3}\,, \tag{5.22}$$

$$d_{\pm} = \gamma \mp (\gamma_+ + \gamma_-) \pm k(\gamma_+ - \gamma_-)\,, \tag{5.23}$$

$$u_{\pm} = (c_{\pm}\gamma_{cm}^2 + \gamma_{cm}^{*2})^{1/2}\,, \tag{5.24}$$

$$c_{\pm} = (\gamma_{\mp} - k)^2 - 1\,, \tag{5.25}$$

$$\gamma_{cm}^* = k(\gamma_+ + \gamma_- - k)\,. \tag{5.26}$$

The total number of leptons annihilated is given by the number of photons emitted. This is illustrated by looking at the annihilation process itself.

$$e^- + e^+ \longrightarrow \nu_1 + \nu_2 \tag{5.27}$$

Where ν_1 and ν_2 represent the two resulting photons. We should note that this is a specific type of lepton annihilation where two photons are emitted. Other types, where more photons are emitted, also exist. However, they are not taken into account here, because the higher order annihilation typically have smaller interaction cross-sections when compared with the process shown in equation 5.27. Using the relation in equation 5.20 in this way is only valid if the electron and positron energy distributions i.e. the number of electrons at energy γ is identical to the number of positrons also at that energy. To take different electron and positron energy distributions into account, the electron and positron numbers are normalized to the total number of leptons. The photon emissivity thus becomes:

$$\dot{n}(k) = \frac{n(\gamma_+)n(\gamma_-)}{n(\gamma_+) + n(\gamma_-)}\int \frac{\mathrm{d}\mu}{2}\frac{\gamma_{cm}^2}{\gamma_+\gamma_-}2\beta_{cm}c\frac{\mathrm{d}\sigma}{\mathrm{d}k}(j,\gamma_+,\gamma_-,\mu)\mathrm{d}k\,, \tag{5.28}$$

which gives the total number of photons produced via annihilation. Because of the nature of the process (equation 5.27), $\dot{n}(k)/2$ gives the number of electrons or positrons annihilated. This kind of normalization is necessary to work with the discrete lepton energy distributions.

In effect, equation 5.28 is used to calculate the contribution from each electron and positron energy bin to each photon frequency bin. This also provides the number of electrons and positrons to be removed from their respective energy bins.

5.4.1 Results

The first part of the following section presents the pair annihilation spectra when purely thermal or purely power-law lepton energy distributions are modelled. The annihilation spectra are then further explored with other physical processes, such as Compton scattering and bremsstrahlung radiation, present. The model's geometry and set-up are kept essentially the same throughout all the simulations presented here. Only the parameters are varied. The model is set using a "cool" disc with a "hot" hemispheric plasma above it. The low energy photons from the disc are injected into the corona where the high energy electrons are able to scatter them. The annihilation process takes place in the corona only and any annihilation signature is added to the other flux emanating from the same region.

5.4.1.1 Annihilation from thermal distributions

Various parameters in the HEART code affect the annihilation line. The following section outlines how factors such as the lepton number density and the lepton temperature (for a thermal distribution) can affect the annihilation line. These parameters are explored not only to gain an understanding of the pair annihilation, but also to check that the process is modelled in a physically consistent manner.

Figure 5.4 illustrates the spectral energy distribution (SED) obtained from the HEART code that shows the blackbody spectrum and the annihilation line (511 keV corresponds to a frequency of $\sim 1.24 \times 10^{20}$Hz). No other process are being modelled and only the thermal lepton are present. The black-body photons are from the the accretion disc. The black-body photons are required by the model to "pick-up" the photons from any other processes. This is purely due to the way the code is constructed: the blackbody photon distribution is required in order to have an existing photon population to which the annihilation photons can be added. In this particular case, the black body photons travel through the corona, i.e. the cells, without interaction; the annihilation photons are added to the traversing photons in each cell.

Figure 5.5 shows how the annihilation line behaves with increasing the positron number density. The electron number density is kept constant at $5 \times 10^{22}\mathrm{m}^{-3}$.

It can be seen that the annihilation line strength increases as the number density of annihilating pairs is increased. Table 5.1 gives some of the key parameters used for the results shown in figure 5.5. For convenience, the black-body spectrum is not shown, but it is included and remains constant, because the black-body photons from the disc are not interacting in the

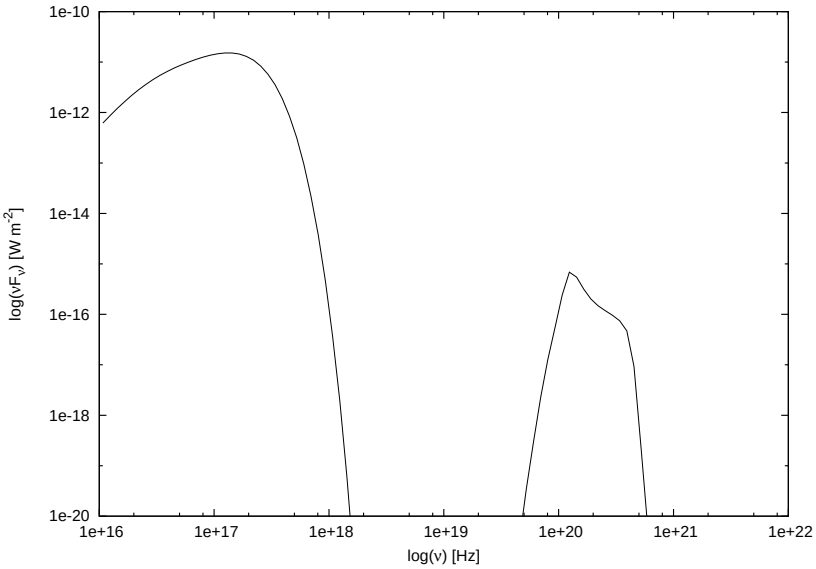

Figure 5.4: Spectral energy distribution obtained from pair annihilation in the HEART code. $n_{e^-} = 5 \times 10^{22}$ and $n_{e^+} = 5 \times 10^{14}$. The blackbody spectrum as well as the annihilation line can be seen. With the lepton temperature at 50 keV, thermal line broadening is also observed. The disc temperature is 0.2 keV.

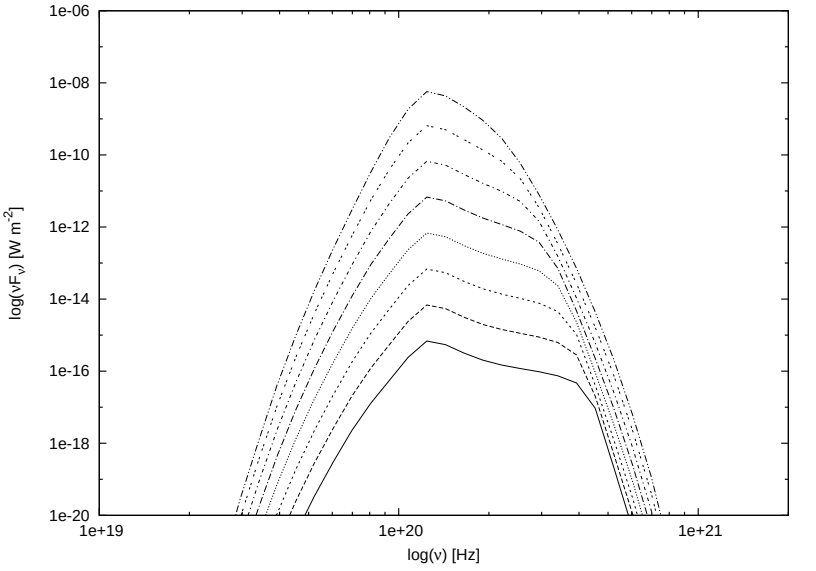

Figure 5.5: Annihilation line varying with positron number density for thermal distributions. Electron number, $n_{e^-}[\mathrm{m}^{-3}]$, kept constant at 5e22. With increasing line intensity, $n_{e^+}[\mathrm{m}^{-3}]$ is changing as $5\times10^{14}, 5\times10^{15}, 5\times10^{16}, 5\times10^{17}, 5\times10^{18}, 5\times10^{19}, 5\times10^{20}, 5\times10^{21}$ (bottom curve to top curve respectively).

Table 5.1: Key parameters for demonstrating annihilation line behaviour with increasing annihilating pairs number density.

Parameter	value
Disc temperature	0.2 keV
Electron temperature	50 keV
Positron temperature	50 keV
Electron number density	$5 \times 10^{22}[\mathrm{m}^{-3}]$

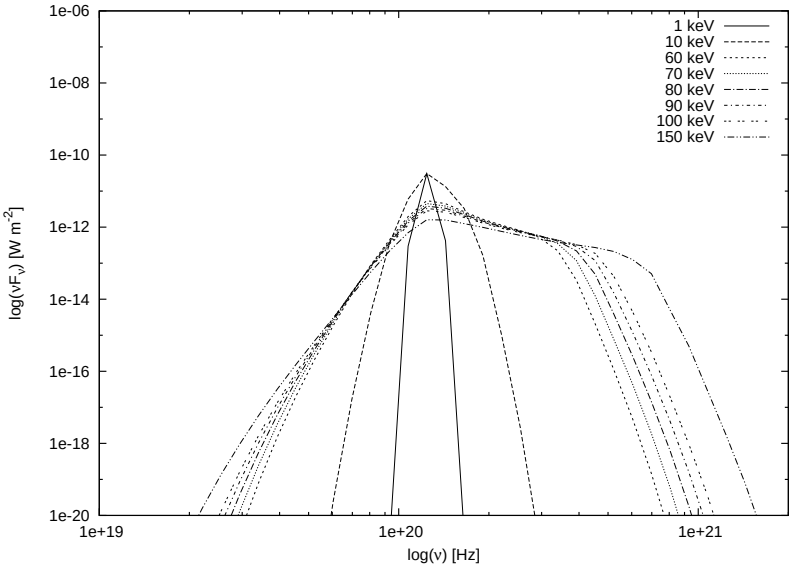

Figure 5.6: Annihilation line behaviour with changing the lepton temperature. $n_{e^-} = 5 \times 10^{22}[\mathrm{m}^{-3}]$ and $n_{e^+} = 5 \times 10^{18}[\mathrm{m}^{-3}]$

corona. Figure 5.5 also shows another interesting characteristic of the annihilation line; there is a certain amount of broadening and almost a bi-modal behaviour in the annihilation line for the lower positron number density. In order to explain this, it is convenient to first look at thermal line broadening.

Figure 5.6 shows how increasing the lepton temperature, a well defined, narrow annihilation line is broadened considerably. Svensson (1982) explores this. The annihilation line emissivity is shown in figure 5.7. Increasing the lepton energy, changes the annihilation emissivity considerably from the delta function behaviour associated with the cold annihilating leptons.

Figure 5.5 illustrates that, for fixed temperature, fewer cold pairs annihilate when the positron number density is reduced. The broadening effect therefore appears to be stronger, because the distinct narrow annihilation (from the colder leptons) line is weaker. As the number density of the annihilating pairs increases, the signal from the low-energy pair annihilation starts to dominate. Figure 5.6 is also a demonstration of how in HEART the annihilation emissivity behaves in a way that is a combination of the three cases shown in figure 5.7; not only is the thermal broadening seen, but the bi-modal behaviour (with an increase in the lepton energy) is seen as well. The net effect of increasing the thermal lepton temperature is to weaken and smear the

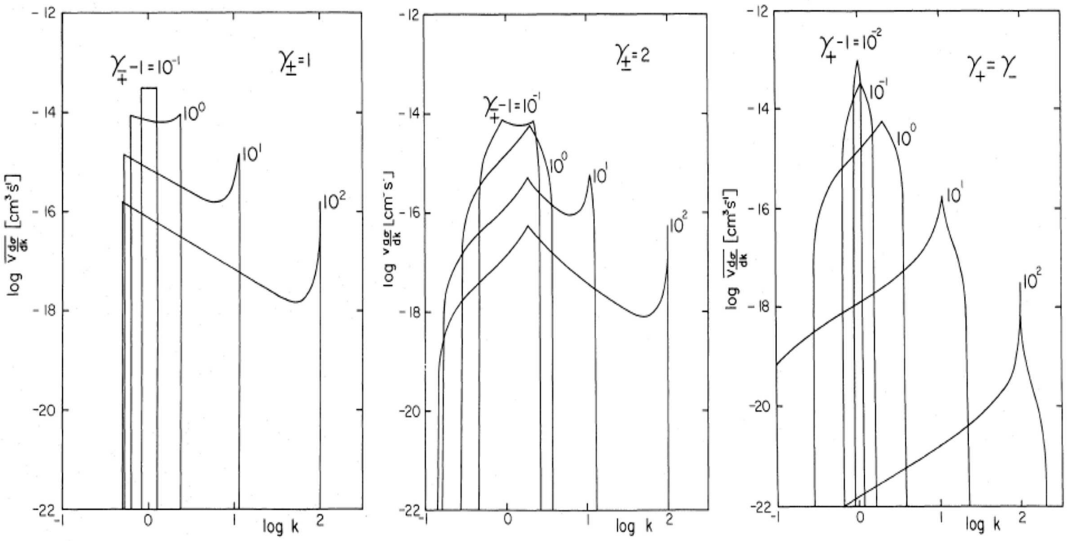

Figure 5.7: Angle averaged emissivity for mono-energetic particle distributions (Svensson (1982)) with varying combination of γ_+ and γ_-.

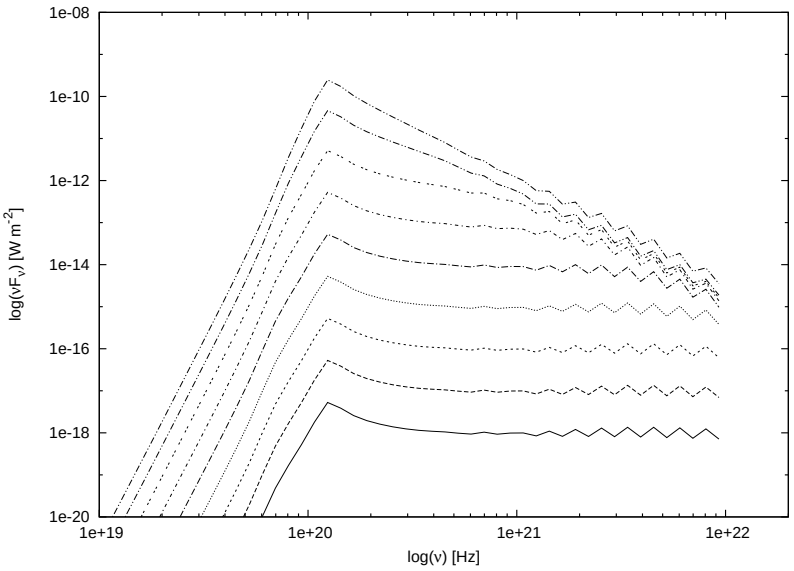

Figure 5.8: Annihilation spectrum with purely power-law e^-/e^+ distributions. The electron n_{e^-} is kept at $1\times10^{22}[\mathrm{m}^{-3}]$ while n_{e^+} is varying as $1\times10^{14}, 1\times10^{15}, 1\times10^{16}, 1\times10^{17}, 1\times10^{18}, 1\times10^{19}, 1\times10^{20}$and 1×10^{21} (bottom to top curve respectively).

annihilation line.

5.4.1.2 Annihilation from power-law distributions

The pair annihilation line masking and the spectra from a physical source, presented in later sections (5.4.1.3 and 5.4.2), are modelled using thermal lepton distributions only. For completeness the pair annihilation with the power-law energy distribution is also demonstrated here.

Figure 5.8 has the spectra from a purely power-law lepton energy distributions. The electron number density is kept constant while the positron number density is varied to change the annihilating pairs density. It is evident that the annihilation spectrum for a power-law distribution does not behave in the same way as that for the thermal e^-/e^+ distribution. Before further inspection of this difference, a look at the thermal and the power-law e^-/e^+ distributions can be useful.

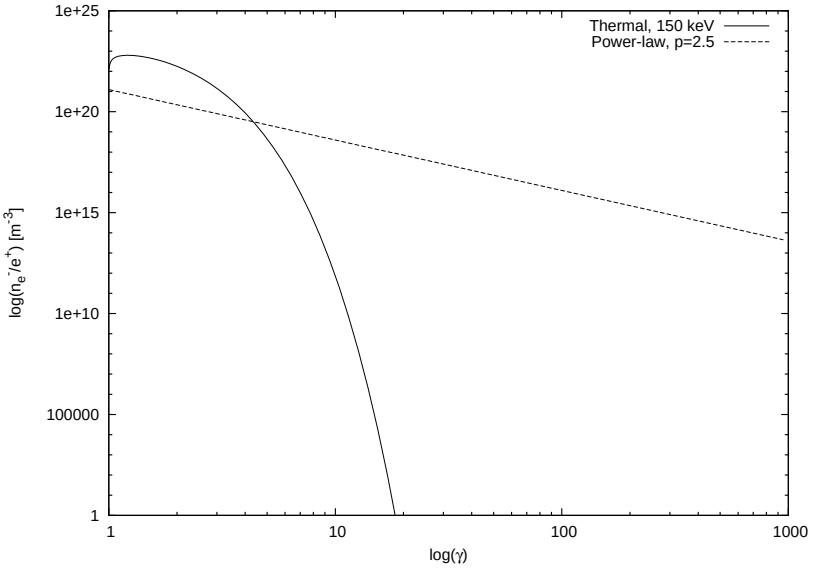

Figure 5.9: The thermal and the power-law lepton energy distribution with $\Theta = 150$ keV (thermal) and the power-law index, $p = 2.5$ (power-law)

Figure 5.9 shows the thermal and the power-law energy distribution for the electrons/positrons in the HEART code. A temperature of 150 keV would be considered very high for an X-ray binary corona. However, it is used to illustrate the differences between the power-law and the thermal energy distributions. The first main difference is the fact that the thermal distributions have a cut-off, while the power-law distributions do not. The power-law distribution therefore extends to much higher energies, thus contains many more high energy leptons. Of course, the power-law index can be changed to vary the number of high energy leptons available. This would require the power-law index to be much different from $\sim$2.5; the power-law index value of $\sim$2.5 is generally considered reasonable for a power-law lepton energy distributions in systems such as the black hole X-ray binaries (Liang and Narayan, 1997) .

Table 5.2: Key parameters for demonstrating annihilation line behaviour with Comptonization and bremsstrahlung.

Parameter	value
Disc temperature	0.2 keV
Electron temperature	50 keV
Positron temperature	50 keV
Electron number density	$5 \times 10^{22}[\mathrm{m}^{-3}]$
e^-/e^+ distribution	Thermal only

The differences between the two distributions have a significant impact on the annihilation spectra. The annihilation line from the power-law leptons (figure 5.8), shows many oscillations at high energies. The main reason for these oscillations is the logarithmic binning of the energy distribution. However, the super-position of the emissivity peaks illustrated in figure 5.7 (showing how the annihilation emissivity, with increasing γ_{e^-/e^+}, produces secondary peaks) can also play a role.

5.4.1.3 Masking the annihilation signature

The following section takes a brief look at inverse Compton scattering and bremsstrahlung radiation as means of masking the annihilation line. Figures 5.10 and 5.11 show how the annihilation line compares with the two radiative processes: Compton scattering and bremsstrahlung radiation respectively. Table 5.2 gives the key parameters used for both the Comptonization and the bremsstrahlung radiation with the pair annihilation.

When Compton scattering is active (fig 5.10), the system geometry has not been changed from the previous section. That is, a hot hemisphere of corona above a cool accretion disc. The corona almost completely covers the disc. The only changes are to the lepton density and the disc temperatures. With the inverse Compton scattering taking place, a fraction (which depends on the optical depth) of the photons are up scattered and then distributed evenly in the six cubic directions. The reprocessing is not taken account. Therefore any photons travelling back into the disc are "lost".

The figures show that with a low positron number density the annihilation line is almost completely hidden. Increasing the electron and the positron number density does lead to a stronger Comptonization component, but that also creates a strong and dominating annihilation line, with many cold pairs annihilating. Only the thermal e^-/e^+ energy distributions are modelled to simulate the "hard state" of an X-ray binary; thus, the presence of a Comptonizing corona is an inherent assumption. With an increasing lepton density, three humps can be seen to appear in the SED shown in figure 5.10: the first low energy hump is the blackbody photons, the second is the "Comptonization hump", and the third corresponds to the annihilation line.

For the bremsstrahlung, the blackbody photons are not scattered, but only added to by the bremsstrahlung photons (and the annihilation photons). We can see that the bremsstrahlung

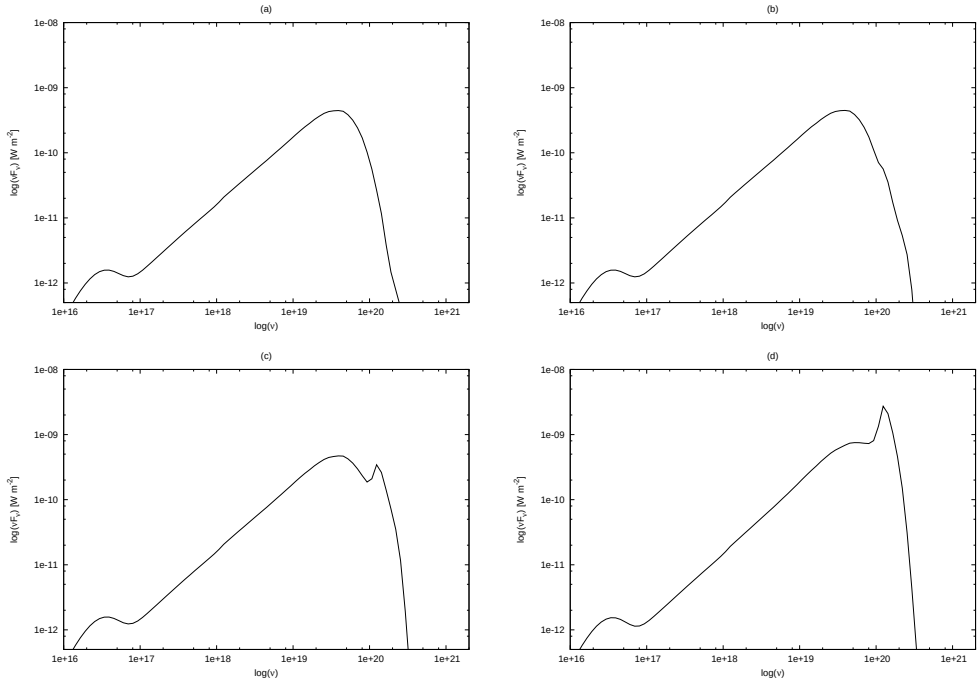

Figure 5.10: Annihilation spectrum with Comptonization. The electron number density is 5×10^{22}. The positron number density is varied (a) 5×10^{18} (b) 5×10^{19} (c) 5×10^{20} (d) 5×10^{21}.

emissivity (figure 5.11 and 5.12), with the parameters outlined in table 5.2, is not high enough, at relevant frequencies, to mask the annihilation line (figure 5.11). Increasing the lepton number density does not increase the bremsstrahlung emission sufficiently. Instead, the annihilation signature becomes extremely strong. Once again, three humps can be seen the spectra: these correspond to the blackbody spectrum, the bremsstrahlung and the annihilation line. The blackbody photons can be seen to be unaffected (not scattered) by the bremsstrahlung radiation.

Zdziarski (1984) show that the bremsstrahlung emissivity can compete with the annihilation line at plasma temperatures, $kT/m_e c^2$, ranging from 0.5 to 3.16. These temperatures correspond to an AGN environment. For completeness, figure 5.12 shows how the annihilation line is almost completely hidden by the bremsstrahlung emissivity at the high lepton temperatures. The high temperature, necessary for higher bremsstrahlung emissivity, would not be considered *realistic* for the X-ray binaries. It appears that unlike Comptonization, bremsstrahlung radiation is unable to obscure an annihilation signature in the X-ray binaries.

5.4.2 Simulating the pair annihilation signature from GRS 1915+105

The previous section outlined how the Comptonization can quite effectively mask an annihilation line signature. This is further explored in the following section by simulating an X-ray binary system GRS 1915+105. The simulated spectra are qualitatively compared to the data obtained from the high energy observatory *INTEGRAL*.

Figure 5.13 illustrates the Comptonization spectra with different annihilating pair densi-

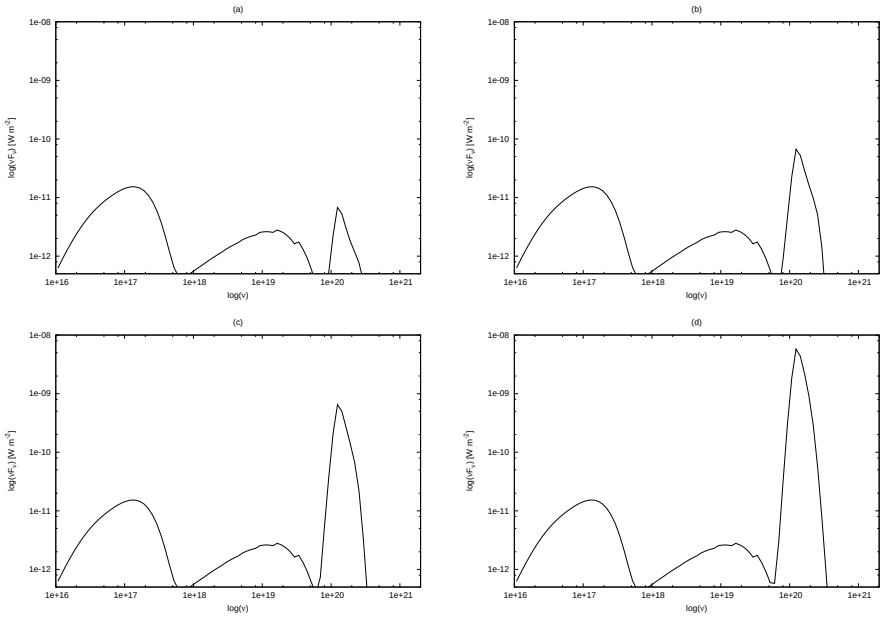

Figure 5.11: Annihilation spectrum with bremsstrahlung. The electron number density is 5×10^{22}. The positron number density is varied (a) 5×10^{18} (b) 5×10^{19} (c) 5×10^{20} (d) 5×10^{21}.

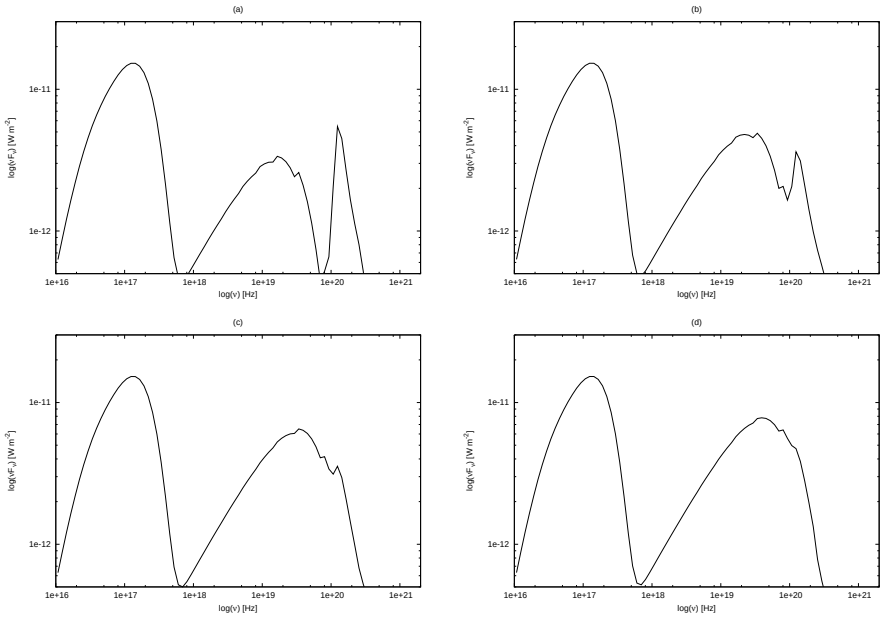

Figure 5.12: Annihilation spectrum with increasing plasma temperature bremsstrahlung. $n_{e^-} = 5 \times 10^{22}$, $n_{e^+} = 5 \times 10^{18}$. The lepton temperature, kT, is (a) 60 keV, (b) 90 keV, (c) 120 keV, (d) 150 keV .

ties. As the positron number density approaches the electron number density, the annihilation line starts to dominate the spectrum; similar behaviour was seen in section 5.4.1.3. Table 5.3 gives the key parameters used for the simulation. The high lepton density does mean a strong

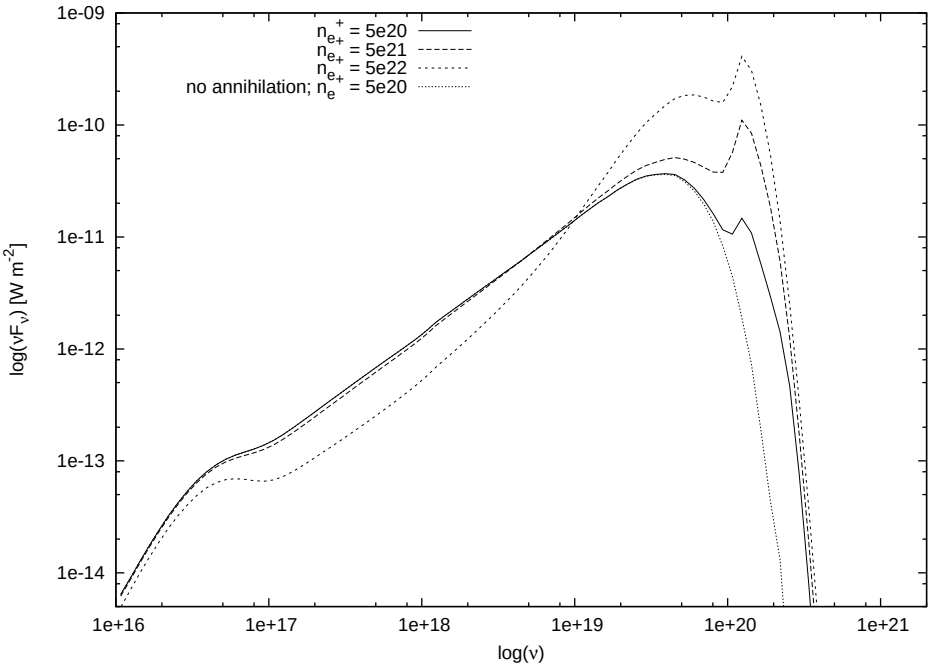

Figure 5.13: Annihilation spectrum simulated in GRS 1915+105. Comptonization is also modelled. The parameters used for the simulation are given in table 5.3. The curves show how the annihilation line gets stronger as the positron number density is increased.

Comptonization component is present, 5.13, but not sufficient to hide the annihilation line.

The question arises: why has no clear annihilation signature been detected from an individual binary systems? Figure 5.14 shows the *SPI* (the spectrometer on board *INTEGRAL*) composite spectra of the source GRS 1915+105. The authors (Droulans and Jourdain, 2009) fit a thermal and a power-law component to the results. There appears to be a high energy excess that has not been fitted. However, the statistics at the higher energies, $\geq$ 100 keV, are quite poor. The fits are therefore perfectly reasonable without having fitted this apparent high energy excess. Even with this in mind, if it is assumed that the data points above 100 keV are "real", then figure 5.13 illustrates an interesting alternative.

Figure 5.13 shows the simulated spectra for GRS 1915+105. In total, the figure shows four different set-ups: 1) Comptonization only; 2) 3) and 4) Comptonization + annihilation, with different positron number densities. When compared with the entire data-set shown in figure 5.14, it is clear that the simulated curve would not provide a good fit for the lower energy data. This is mainly due to the poorly simulated 20-100 keV energy band. There are number of reasons for the poor fit in this energy band: different Comptonization parameters, plus the omission of components such as the disc reflection. Detailed spectral fitting is not the focus of the present work, and the HEART code's ability to do spectral fitting has been discussed in detail by Rogers (2008). On the other hand, the high energy ($>$ 100 keV) behaviour of the simulated curve is remarkably similar to the data. One could interpret the high energy excess as an indication of an underlying, and high broadened, annihilation line. Unfortunately, poor statistics mean that we are unable to verify this hypothesis. With the aid of better resolution data, it

Table 5.3: Key parameters for demonstrating annihilation line in GRS 1915+105.

Parameter	value
Disc temperature	0.2 keV
Electron temperature	50 keV
Positron temperature	50 keV
Electron number density	$5 \times 10^{22} [\mathrm{m}^{-3}]$
BH mass	10 $\mathrm{M}_{\odot}$
Disc inner radius (Schwarzschild)	3
Disc outer radius (Schwarzschild)	50
Corona diameter	3×10^{6} m
Inclination angle	70^{o}
e^{-}/e^{+} distribution	Thermal only

may be possible to distinguish a highly broadened annihilation line from the Comptonization continuum.

There could be a number of reasons why the annihilation line remains elusive in the X-ray binaries. If there is a disparity in the number of leptons involved in the annihilation and the number responsible for other processes such as Comptonization, then the annihilation line can be broadened to such an extent that it behaves almost like continuum itself. This can make the annihilation line indistinguishable from the Comptonization continuum, making annihilation line observation extremely difficult in the X-ray binaries. Also the instrument limitations can have a role to play. Comparing the simulated spectra with the *INTEGRAL* sensitivity shows that vast observation times are required to observe a highly broadened annihilation line. This is just an indication of how few a high energy photons are detected, hence the poor statistics.

5.5 Conclusions

Electron-positron pair annihilation is an important process when it comes to modelling the high energy emission from the X-ray binaries. It has been shown that if an equal number of electrons and positrons are present in the corona, the annihilation signature is very distinctive. The fact, however, remains: no clear annihilation signature has been detected from an X-ray binary. A case was discussed where one possible interpretation of the data involved a broadened annihilation line. The poor statistics for the high energy data meant that no definitive conclusions could be drawn.

On the other hand, if the lepton numbers are not equal or the annihilating pairs number density is limited by some mechanism, then it is possible to mask the annihilation line. The masking is even easier due to the thermal broadening of the line. Bremsstrahlung radiation has been suggested as a process that may be able to hide the annihilation line, but it requires very high coronal temperatures. It should, however, be pointed out that only the electron/positron - electron/positron bremsstrahlung is taken into account. Haug (1985) gives a comparison of the electron-proton, the electron-electron and the electron-positron bremsstrahlung. The

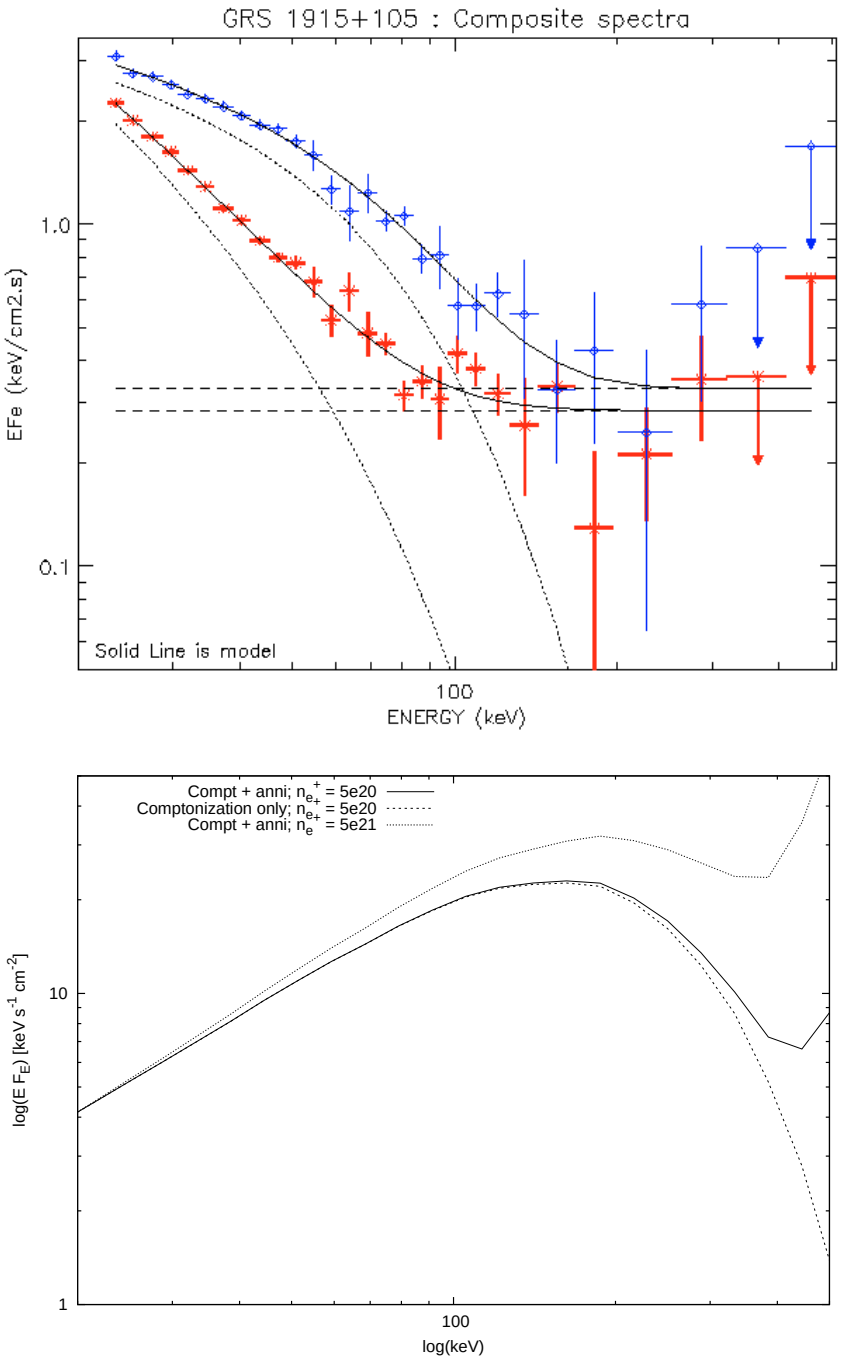

Figure 5.14: Top: The spectrum, Droulans and Jourdain (2009), shows composite spectrum from *SPI/INTEGRAL* for GRS 1915+105. The energy ranges is from 20-500 keV. The data points in blue are composite of two observations with 'hard' photon index; data points in red correspond to the 'soft' sample, also composed of two observations. Bottom: Simulated annihilation and Comptonization spectra for GRS 1915+105. The curves show one simulation without any annihilation taking place and two with annihilation, but with differing lepton number densities. Electron number density in all the cases is 5×10^{22}.

electron-proton bremsstrahlung can be hugely important at the low electron (and photon) energies. Electron-positron bremsstrahlung appears to be an even stronger process at similar

energies . Neglecting these two processes makes it difficult to make a true comparison between the annihilation and the bremsstrahlung emissivities. Any future work must take these additional processes into account to better understand the annihilation signature obscuration by the bremsstrahlung radiation.

Based on the simulations shown, inverse Compton scattering is the best candidate for masking the annihilation signature. Even with the limitations of the inverse Compton scattering implementation in the HEART code (outlined in section 5.3.4) it is possible to appreciate how the Comptonization can be effective in making the annihilation indistinguishable from the continuum - this is facilitated by the highly broadened annihilation line. A more accurate Compton scattering implementation should, in theory, enhance the Comptonization effects; thus, any future work that incorporates both the annihilation and the Comptonization should support the present results.

In short, any future analysis in this field must take the issues outlined above into consideration. Future high energy observatories may also be able to shed more light on this puzzle. Further research is therefore necessary to rule out the instrumentation being the only reason for not observing the annihilation lines from the X-ray binaries.

6
Conclusions

Thus far I have presented an assortment of results related to the disc:jet environment. Much like this field, the research and the subsequent results have involved quite an array of areas. The following chapter re-iterates various findings and conclusions, plus presents the future directions for this exciting field.

6.1 *i*Shocks and the flat spectrum

An internal shocks model, *i*Shocks has been presented to address the re-acceleration problem in the conical geometry jets. The re-acceleration problem arose out of the explanation for the flat/inverted spectrum from the compact radio sources. The existing models were able to explain how such a spectrum would result from the super-position of multiple self-absorbed synchrotron spectra from different parts of the jet. However, none of the models could reproduce the flat/inverted spectrum whilst taking the adiabatic losses, associated with a conical jet, into account. The *i*Shocks model has been used to demonstrate successfully how the use of relativistic shocks all along the jet can be used to reproduce the canonical flat/inverted spectrum; the jet is discretized in the form of shells and the shell collisions give rise to the shocks that are responsible for the re-energization. The shell collisions are a result of variation in the shell velocities (the faster shells catch up with the slower ones) and the expansion of the shell walls inside the jet volume.

It was shown that with an essentially random distribution of the shell properties, it is possible to achieve sufficient re-energization from the relativistic shocks. However, injecting the shells with some internal energy at the point of ejection also has an important role to play.

Interestingly, we also found that the high frequency turnover/break in the flat spectrum is correlated with the jet power by: $\nu_b \sim L_{\rm W}^{0.6}$. (The low frequency turnover did not show any obvious correlation, as a longer jet leads to a lower frequency turnover.) While the flat-spectrum synchrotron flux is correlated with the total jet power by: $F_\nu \sim L_{\rm W}^{1.4}$. Both these relations are in remarkable agreement with the previous analytical predictions.

Although the focus of the present work was on the flat/inverted spectra from the X-ray binaries, the model is scale independent and can easily be adapted to model the AGN jets. The *i*Shocks reproduction of a flat/inverted spectrum, with the adiabatic losses active, has been the first of its kind and a successful application to larger scale jets would simply strengthen its standing.

6.2 X-ray binary flaring

Flaring behaviour is another interesting property of the X-ray binaries. This can include a single massive ejection or repeated ejections. These ejection events have been observed in the X-ray, the IR, the mm, and the radio simultaneously, but without a sound understanding of the underlying physics. The most curious aspect of these events is the almost flat spectrum (ranging from IR to radio) and the similar rise times for both the IR and the radio.

The *i*Shocks model was used to model the repeated ejection events in the source GRS 1915+105. The observational data give the impression of "blobs" being ejected. Various models, including ours, are unable to replicate the observations with such a setup. The equivalent IR and radio rise times are not possible from a single emitting electron population. The *i*Shocks results do show an alternative picture: varying the mass almost continuously can give the impression of a massive "blob" becoming optically thin at the observed frequency. This scenario can reproduce the almost identical rise times for the different observed frequencies, but the flux normalization does not match the observations. The flat spectrum, as in the case of the steady jet, requires some kind of acceleration (if the adiabatic energy losses are present). Unfortunately, in the *i*Shocks construct, the periodicity of the flaring observations is not replicable with the mergers taking place. Based on the results presented, we can conclude that the flaring events are not well modelled by a simple blob ejection picture. It looks like that the flaring events are a result of strong variability of the mass present in the jet, plus some form of re-acceleration that preserves the timing information whilst giving rise to a flat spectrum. The complex nature of the flaring state is also seen in the X-rays, in the form of the hardness-rms diagrams. An attempt at correlating the X-rays with the radio in this state may elaborate on the underlying physics.

6.3 Optical/X-ray correlations

The optical/X-ray correlation is another enigmatic behaviour by the X-ray binaries. The cross-correlation function for the optical and the X-ray show that the optical flux drops before the

rise in the X-rays, in addition to showing a rise after the X-rays rise. In other words, the optical varies ahead of the X-ray behaviour. This correlation has ruled out the X-ray re-processing scenario.

The observations have shown the rate of change in X-rays was also correlated with the optical. The *i*Shocks model was therefore an ideal candidate for this study. The X-ray light curves were modelled and *translated* into the shell properties: the shell mass and the shell bulk Lorentz factor. The optical emission from the jet could then be correlated with the mass and the bulk Lorentz factor time-series (or the simulated X-ray light curves).

A number of interesting results were found from the *i*Shocks simulations. The positive lag could be explained quite simply if one considers the X-rays to be indicative of the accretion rate (hence the ejection rate in the jet) and the optical lag being the time the plasma takes to become optically thin at the observed frequencies. While one particular set-up showed a precognition dip, a clear explanation of the dip remains elusive. The simulations do show that it is possible to get an anti-correlation between the optical and the X-ray due to the shell mergers taking place, but the optical emission shows only a positive lag to the X-rays. The *i*Shocks model, however, successfully demonstrated the optical power-spectrum flattening, when compared to the X-ray power-spectrum. This is as a result of shocks re-acceleration adding more time-scales.

Although the *i*Shocks modelling of the optical/X-ray correlations was not able to explain and demonstrate all of the observed phenomena, it has pointed us in a new direction that may be able to explain these behaviours from a more physical point of view.

6.4 Electron-positron annihilation in the corona

The electron-positron annihilation implementation was an investigation into the lack of the 511 keV annihilation line signature from the X-ray binaries. It is clear that the X-ray binaries have high energy processes taking place to give rise to the hard X-rays and even γ-rays. These high energy processes are generally considered to happen in the so-called corona. By analogy to the Galactic Centre, from where a strong annihilation signature has been detected, one would expect the lepton populations in the XRBs to give rise to such a signature as well.

The e^-/e^+ annihilation was implemented in the HEART code that models various other high energy processes, for example, the Compton scattering and the bremsstrahlung. The annihilation signature was then compared with the masking effects of these processes. In case of the bremsstrahlung emissivity masking the annihilation line, we found that this was only possible for AGN like temperatures in the corona: in the X-ray binary environment the bremsstrahlung would not be able to disguise the annihilation signature. This, however, is only true of the electron-electron and the positron-positron bremsstrahlung. Various authors have found that the electron-positron and electron-proton bremsstrahlung are much more effective. Therefore to truly understand the bremsstrahlung role here, a more wide ranging bremsstrahlung implementation is required.

Inverse Compton scattering on the other hand was more promising for masking such a

signature. Our results showed that the annihilation, when already thermally broadened, can almost completely disappear into the Compton hump or continuum. Even though the Compton scattering implementation is far from ideal in the HEART code, these comparative results are insightful nonetheless. Suggestions of an annihilation line, for GRS 1915+105 with *INTEGRAL*, were also shown.

Overall, the results may even be suggesting that the region where the e^-/e^+ annihilation takes place is different in the X-ray binaries when compared to the Galactic Centre. It is possible that the pair annihilation in the XRBs takes place in the same (or inside) region as where the Compton scattering occurs, thus masking the annihilation signature; whereas, in the Galactic Centre the annihilation takes place in a cooler outer region, resulting in a strong signature. Higher resolution high-energy observations (plus, further in-depth modelling) of the XRBs may solve this mystery.

6.5 Future work

The *i*Shocks simulations show that more physical interpretations of the optical/X-ray correlations are not straightforward. A further exploration of how the X-rays can be translated into the jet properties is necessary. This, however, may need to be in a slightly different framework. One of the key results that was left unanswered is the pre-cognition dip in the optical/X-ray CCFs. The problem may be how we are viewing the situation itself: traditionally the power-law component or the high energy (of the X-ray spectrum) variability has been correlated with the optical data. Wilkinson and Uttley (2009) have shown that the disc component varies more, on longer times scales, in the hard state. This suggests that the disc component is the real driving force behind the variability, and not the power-law component. Therefore it makes sense to correlate the jet properties with the disc variability instead. In fact, the pre-cognition dip conundrum maybe solved by this connection.

The *i*Shocks model has been a great springboard for increasing our understanding of theses correlations. It offers a great starting point for further enhancement. These include: the way synchrotron spectrum, plus the relativistic shocks physics, is calculated can be implemented in more detail. This could be necessary to understand the dynamics of still quite poorly understood flaring behaviour in the X-ray binaries. Currently, unrealistic energy densities would be required to model the large ejections. The energy dynamics therefore require attention. The radiative losses implementation is also quite important, and relatively straightforward to implement, to have a more comprehensive model.

The *i*Shocks model's ability to explain the flat/inverted spectrum with the aide of the relativistic shocks re-acceleration, plus the results of shell mass and the bulk Lorentz variability, also point at how the future jet models may be constructed. The Ohsuga *et al.* (2009) simulations have shown us how different XRB states can be linked with the disc:jet configuration. In an ideal world we would be able to model the synchrotron spectrum from such a GRMHD simulation. This may also allow the exploration of the collision-less shocks as a means of re-

energization. The future therefore my lie in the MHD disc-jet simulations with the radiative transfer modelling, but tempered with explaining the plethora of XRB and AGN data.

APPENDICES

A

Synchrotron emission

The numerical solutions for calculating the synchrotron emission are stated below (Longair, 1994).

When the synchrotron monochromatic intensity is given by:

$$I_\nu = \frac{J_\nu}{4\pi\chi_\nu}(1-e^{-\chi_\nu r}) \,, \tag{A.1}$$

the numerical solution for the emission and the absorption coefficients are as follows:

$$J(\nu) = 2.344\times10^{-25}a(p)B^{(p+1)/2}\kappa\left(\frac{1.253\times10^{37}}{\nu}\right)^{\frac{(p-1)}{2}} \ \mathrm{Wm^{-3}Hz^{-1}} \tag{A.2}$$

and

$$\chi(\nu) = 3.354\times10^{-9}b(p)B^{(p+2)/2}\kappa(3.54\times10^{18})^p\nu^{-(p+4)/2} \ \mathrm{m^{-1}}. \tag{A.3}$$

The energy spectrum $N(E)$ represents the number density of electrons per joule. The constants $a(p)$ and $b(p)$ are given by:

$$a(p) = \frac{\sqrt{\pi}}{2}\frac{\Gamma(\frac{p}{4}+\frac{19}{12})\Gamma(\frac{p}{4}-\frac{1}{12})\Gamma(\frac{p}{4}+\frac{5}{4})}{(p+1)\Gamma(\frac{p}{4}+\frac{7}{4})}, \tag{A.4}$$

and

$$b(p) = \frac{\sqrt{\pi}}{8}\frac{\Gamma(\frac{3p+12}{12})\Gamma(\frac{3p+2}{12})\Gamma(\frac{p+6}{4})}{\Gamma(\frac{p+8}{4})}. \tag{A.5}$$

The Γ-function is given by (Abramowitz and Stegun, 1972):

$$\Gamma(n) = \int_0^\infty x^{n-1} e^{-x} dx, \tag{A.6}$$

and the numerical calculation can be found in the numerical recipes (Press, 2002).

B

Compton scattering

The photon redistribution functions for the three cases defined in section 5.3.2.2 are detailed below.

The solution for case 1 can be found in Coppi and Blandford (1990). This is the case of mildly relativistic electrons ($\gamma < 10$) interacting with high-energy photons ($k > 10^{-2}$),

$$xF_C(x) = 3\sigma_T x^2 \int \frac{\mathrm{d}P}{\mathrm{d}z}\mathrm{d}z \tag{B.1}$$

where $\frac{\mathrm{d}P}{\mathrm{d}z}$ is given by:

$$\frac{\mathrm{d}P}{\mathrm{d}x} = \frac{1}{(1-\beta z)\sqrt{\beta^2+\varepsilon^2+2\beta\varepsilon z}} \times \left\{ 2y_0 k - ak^2 + \frac{1+y_0^2-2ay_0k+a^2k^2}{\sqrt{a^2-b^2}} + \right.$$
$$\left. \frac{1}{k^2(1-\beta z)}\left[k^2 + \frac{ak^2(2b-a)}{(a-b)\sqrt{a^2-b^2}} + \frac{a(1-y_0)^2+2kb^2(1-y_0)-ba^2k^2}{(a^2-b^2)^{\frac{3}{2}}} \right] \right\} \tag{B.2}$$

where $\varepsilon = h\nu_0/(\gamma m_e c^2)$, $k = \gamma m_e c^2/(h\nu_1)$, $a = 1-\beta z-(1-\gamma_0)/k$, $b = \delta/k$ and

$$y_0 = \frac{(\varepsilon+\beta z)(\rho+\varepsilon\rho-1+\beta z)}{\rho(\beta^2+\varepsilon^2+2\beta\varepsilon z)}, \tag{B.3}$$

$$\delta = \frac{\beta\sqrt{(a-z^2)[\rho^2\beta^2+2\rho\varepsilon(1-p)(1-\beta z)-(\rho-1+\beta z)^2]}}{\rho(\beta^2+\varepsilon^2+2\beta\varepsilon z)} \tag{B.4}$$

and $\rho = \nu_1/\nu_0$. ν_0 and ν_1 are the photon frequency before and after scattering respectively. The integration limits are given by:

$$z_{\pm} = max[\pm 1, \frac{1-\rho(d \mp \sqrt{d^2 - 1/\gamma^2})}{\beta}], \tag{B.5}$$

where $d = 1 + \varepsilon - \varepsilon\rho$.

Enßlin and Kaiser (2000) treatment is used for Case 2: mildly relativistic electrons ($\gamma < 10$) interacting with low energy photons ($k \leq 10^{-2}$),

$$\begin{aligned} xF_C(x) &= \frac{3\sigma_T}{8p^5}\left\{-\frac{|1-\rho|}{4p}\left[1+\rho(10+8p^2+4p^4)+\rho^2\right]+\right. \\ &\left.\rho(1+\rho)\left[\frac{3+3p^2+p^4}{\gamma} - \frac{3+2p^2}{2p}(2\ln(p+\gamma) - |\ln(\rho)|)\right]\right\} \end{aligned} \tag{B.6}$$

where ρ is as in case 1 and $p = \sqrt{\gamma^2 - 1}$.

Case 3 is for ultra-relativistic electrons ($\gamma \geq 10$) (Jones, 1968),

$$xF_C(x) = 3\sigma_T x\left\{2q\ln(q) + (1-q)\left[(1+2q) + \frac{\left(4\gamma q\frac{h\nu_0}{m_e c^2}\right)^2}{2\left(1+4\gamma q\frac{h\nu_0}{m_e c^2}\right)}\right]\right\} \tag{B.7}$$

where $q = x/\left(1 - \frac{h\nu_1}{\gamma m_e c^2}\right)$, the frequency gain $\rho = \nu_1/\nu_0$ and p is the electron momentum.

C

*i*Shocks Parameters

The following section outlines all the customizable parameters in our model. With efficiency and expandability in mind, the model is coded in C++. Effort has been made to minimize dependencies and use GNU software only. Once compiled, the code can read in all the parameters from a simulation parameters file and a shell parameters file; for any subsequent changes to the parameters, the code does not require re-compilation.

The customizable parameters for the code are as follows:

Jet Luminosity: Used when shell properties are *pseudo*-random. This determines the shell mass based on how many shells need to be injected. [J/s]

BLF_max: Used when shell properties are *pseudo*-random. This sets the mean of a Gaussian distribution to be sampled from. [Γ_{max}]

BLF_min: Used when shell properties are *pseudo*-random. This sets the mean of a Gaussian distribution to be sampled from. [Γ_{min}]

shell_width_factor: Sets the initial shell size, along the jet axis using the relation outlined in equation 2.53. [no units]

jet_opening_angle: The full opening angle of the jet. [degrees]

source_distance: Distance to the source being modelled. [kpc]

EThermal_frac: The fraction of the shell internal energy to be given to the thermal energy; causes the longitudinal expansion. [no units]

EelecKin_frac: The fraction of the shell internal energy to be given to the total electron kinetic energy; determines the power-law distribution parameters. [no units]

EMagnet_frac: The fraction of the shell internal energy to be given to the magnetic energy; affects the magnetic field strength. [no units]

powerlaw_index: The power-law index, p, of the electron power-law distribution. [no units]

e_gamma_min: γ_{min} of the power-law electrons. [γ]

e_gamma_max: γ_{max} of the power-law electrons. [γ]

nu_min: ν_{min} for the frequencies being modelled; used when logarithmically spaced frequency range is used. [Hz]

nu_max: ν_{max} for the frequencies being modelled; used when logarithmically spaced frequency range is used. [Hz]

nu_points: Determines the number of points for the logarithmic frequency grid. [no units]

individual_frequencies Switch to turn on logarithmically spaced frequency range; takes min. and max from above. [take integer values: n=off (then uses two frequencies below; y=on]

nu_1 Used if only two frequencies being sampled. [Hz]

nu_2 Used if only two frequencies being sampled. [Hz]

increase_time_resolution A switch for increasing sampling, for radiative emission, of the jet at the time interval given below. [takes integer values: n=off (in this case the jet is sampled only at “events”; y=on]

step_resolution If the above switch is on, this determines the sampling time interval. [s]

total_run_duration Total run time of the simulation. [s]

shell_inj_duration The length of time for the shells injection. [s]

avg_ejection_gap Sets the mean of the Gaussian distribution for sampling the time interval between shell injections. [s]

use_shell_file A switch for reading a file with shell properties: injection time, shell mass, shell Lorentz factor, shell width. [takes integer values: n=off; y=on (when on, jet_luminosity, BLF_max, shell_width, shell_inj_duration, and avg_ejection_gap are all deactivated)]

shell_file Name of the file with shell parameters. [should contain 4 columns with the corresponding shell properties:injection time, shell mass, shell Lorentz factor, shell width.]

write_results_file A switch to activate writing every time step to a file. [takes integer values: n=off; y=on]

results_file Name of the file for the above switch.

final_time_step A switch to activate writing final time step of the simulation. [takes integer values: n=off; y=on]

lightcurve_file Name of the file for writing the light curve data. [Always written by default]

in_vacuum_expansion A switch to deactivate adiabatic losses.

inj_int_energy A switch to inject the shells with internal energy, after they have passed the "shock location".

rel_mass_frac Scale the amount of internal energy given to the shell by a fraction of the of the shell's relativistic energy.

shock_location The shock location. Used when injecting with internal energy. [light seconds]

slow_energization A switch to activate slow energization; the shells are not energized instantly, but given the energy over a length of time determined by the shock crossing time. [takes integer values: n=off, y=on]

BIBLIOGRAPHY

Abramowitz M., Stegun I. A., 1972, *Handbook of Mathematical Functions*

Balbus S. A., Hawley J. F., 1991, The Astrophysical Journal, 376, 214

Balbus S. A., Hawley J. F., 1998, Reviews of Modern Physics, 70, 1

Bell A. R., 1978, Mon. Not. R. Astron. Soc., 182, 147

Belloni T. M., 2009, ArXiv e-prints

Blandford R., Eichler D., 1987, Physical Reports, 154, 1

Blandford R. D., Königl A., 1979, The Astrophysical Journal, 232, 34

Blandford R. D., Ostriker J. P., 1978, Astrophys. J. Lett., 221, L29

Blandford R. D., Payne D. G., 1982, Mon. Not. R. Astron. Soc., 199, 883

Blandford R. D., Znajek R. L., 1977, Mon. Not. R. Astron. Soc., 179, 433

Bouchet L., Mandrou P., Roques J. P., Vedrenne G., Cordier B., Goldwurm A., Lebrun F., Paul J., Sunyaev R., Churazov E., Gilfanov M., Pavlinsky M., Grebenev S., Babalyan G., Dekhanov I., Khavenson N., 1991, The Astrophysical Journal Letters, 383, L45

Casella P., Belloni T., Stella L., 2005, The Astrophysical Journal, 629, 403

Cassé M., Cordier B., Paul J., Schanne S., 2004, Astrophys. J. Lett., 602, L17

Chaty S., Haswell C. A., Malzac J., Hynes R. I., Shrader C. R., Cui W., 2003, Mon. Not. R. Astron. Soc., 346, 689

Churazov E., Sunyaev R., Sazonov S., Revnivtsev M., Varshalovich D., 2005, Mon. Not. R. Astron. Soc., 357, 1377

Collins R. S., 2004, *Modelling Radiative Transfer in High-Energy Astrophysical Plasmas*, Ph.D. thesis, School of Engineering Sciences, Faculty of Engineering, University of Southampton

Coppi P. S., Blandford R. D., 1990, Mon. Not. R. Astron. Soc., 245, 453

Curtis H. D., 1918, Publications of Lick Observatory, 13, 31

Done C., Gierliński M., Kubota A., 2007, The Astronomy and Astrophysics Review, 15, 1

Droulans R., Jourdain E., 2009, Astronomy and Astrophysics, 494, 229

Durant M., Gandhi P., Shahbaz T., Fabian A. P., Miller J., Dhillon V. S., Marsh T. R., 2008, Astrophys. J. Lett., 682, L45

Eikenberry S. S., Matthews K., Morgan E. H., Remillard R. A., Nelson R. W., 1998, The Astrophysical Journal Letters, 494, L61+

Enßlin T. A., Kaiser C. R., 2000, Astron. Astrophys., 360, 417

Esin A. A., McClintock J. E., Narayan R., 1997, The Astrophysical Journal, 489, 865

Fabian A. C., Rees M. J., 1979, Mon. Not. R. Astron. Soc., 187, 13P

Falcke H., 1996, The Astrophysical Journal Letters, 464, L67+

Falcke H., Biermann P. L., 1995, Astronomy and Astrophysics, 293, 665

Falcke H., Biermann P. L., 1999, Astronomy and Astrophysics, 342, 49

Falcke H., Körding E., Markoff S., 2004, Astronomy and Astrophysics, 414, 895

Falcke H., Markoff S., 2000, Astronomy and Astrophysics, 362, 113

Fender R. P., Belloni T. M., Gallo E., 2004, Mon. Not. R. Astron. Soc., 355, 1105

Fender R. P., Garrington S. T., McKay D. J., Muxlow T. W. B., Pooley G. G., Spencer R. E., Stirling A. M., Waltman E. B., 1999, Mon. Not. R. Astron. Soc., 304, 865

Fender R. P., Hjellming R. M., Tilanus R. P. J., Pooley G. G., Deane J. R., Ogley R. N., Spencer R. E., 2001, Mon. Not. R. Astron. Soc., 322, L23

Fender R. P., Homan J., Belloni T. M., 2009, ArXiv e-prints 0903.5166

Fender R. P., Pooley G. G., 2000, Mon. Not. R. Astron. Soc., 318, L1

Fender R. P., Pooley G. G., Durouchoux P., Tilanus R. P. J., Brocksopp C., 2000, Mon. Not. R. Astron. Soc., 312, 853

Fermi E., 1949, Physical Review, 75, 1169

Fragile P. C., 2008, in *Proceedings of the VII Microquasar Workshop: Microquasars and Beyond. September 1 - 5, 2008. Foca, Izmir, Turkey. Published online at http://pos.sissa.it/cgi-bin/reader/conf.cgi?confid=62, p.39*, pp. 39–+

Frank J., King A., Raine D. J., 2002, *Accretion Power in Astrophysics: Third Edition*

Gandhi P., 2009, Astrophys. J. Lett., 697, L167

Gandhi P., Makishima K., Durant M., Fabian A. C., Dhillon V. S., Marsh T. R., Miller J. M., Shahbaz T., Spruit H. C., 2008, Mon. Not. R. Astron. Soc., 390, L29

Gehrels N., Barthelmy S. D., Teegarden B. J., Tueller J., Leventhal M., MacCallum C. J., 1991, The Astrophysical Journal Letters, 375, L13

Geldzahler B. J., Johnston K. J., Spencer J. H., Klepczynski W. J., Josties F. J., Angerhofer P. E., Florkowski D. R., McCarthy D. D., Matsakis D. N., Hjellming R. M., 1983, The Astrophysical Journal Letters, 273, L65

Gilfanov M., Syunyaev R., Churazov E., Pavlinskii M., Grebenev S., Kremnev R., Sukhanov K., Kuleshova N., Goldwurm A., Ballet J., Cordier B., Paul J., Denis M., Bouchet L., Barret D., Roques J. P., 1991, Soviet Astronomy Letters, 17, 437

Gould R. J., 1980, The Astrophysical Journal, 238, 1026

Greiner J., Cuby J. G., McCaughrean M. J., 2001, Nature, 414, 522

Gültekin K., Cackett E. M., Miller J. M., Di Matteo T., Markoff S., Richstone D. O., 2009, The Astrophysical Journal, 706, 404

Harris M. J., Teegarden B. J., Cline T. L., Gehrels N., Palmer D. M., Ramaty R., Seifert H., 1998, The Astrophysical Journal Letters, 501, L55+

Haug E., 1985, Astronomy and Astrophysics, 148, 386

Hawley J. F., Balbus S. A., 1991, Astrophys. J., 376, 223

Heinz S., Begelman M. C., 2000, The Astrophysical Journal, 535, 104

Heinz S., Sunyaev R. A., 2003, Mon. Not. R. Astron. Soc., 343, L59

Hjellming R. M., Johnston K. J., 1988, The Astrophysical Journal, 328, 600

Hjellming R. M., Rupen M. P., 1995, Nature, 375, 464

Hjellming R. M., Rupen M. P., Mioduszewski A. J., Kuulkers E., McCollough M., Harmon B. A., Buxton M., Sood R., Tzioumis A., Rayner D., Dieters S., Durouchoux P., 1999, The Astrophysical Journal, 514, 383

Hynes R. I., 2002, in Gänsicke B. T., Beuermann K., Reinsch K. (eds.), *The Physics of Cataclysmic Variables and Related Objects*, vol. 261 of *Astronomical Society of the Pacific Conference Series*, pp. 676–+

Hynes R. I., Robinson E. L., Pearson K. J., Gelino D. M., Cui W., Xue Y. Q., Wood M. A., Watson T. K., Winget D. E., Silver I. M., 2006, Astrophys. J., 651, 401

Johnson III W. N., Harnden Jr. F. R., Haymes R. C., 1972, The Astrophysical Journal Letters, 172, L1+

Jones F. C., 1968, Phys. Rev., 167 (5), 1159

Kaiser C. R., 2006, Mon. Not. R. Astron. Soc., 367, 1083

Kalemci E., Tomsick J. A., Buxton M. M., Rothschild R. E., Pottschmidt K., Corbel S., Brocksopp C., Kaaret P., 2005, The Astrophysical Journal, 622, 508

Kanbach G., Straubmeier C., Spruit H. C., Belloni T., 2001, Nature, 414, 180

Kobayashi S., Piran T., Sari R., 1997, The Astrophysical Journal, 490, 92

Körding E., Falcke H., Corbel S., 2006a, Astronomy and Astrophysics, 456, 439

Körding E. G., Jester S., Fender R., 2006b, Mon. Not. R. Astron. Soc., 372, 1366

Körding E. G., Migliari S., Fender R., Belloni T., Knigge C., McHardy I., 2007, Mon. Not. R. Astron. Soc., 380, 301

Leventhal M., Barthelmy S. D., Gehrels N., Teegarden B. J., Tueller J., Bartlett L. M., 1993, The Astrophysical Journal Letters, 405, L25

Leventhal M., MacCallum C. J., Huters A. F., Stang P. D., 1982, The Astrophysical Journal Letters, 260, L1

Leventhal M., MacCallum C. J., Huters A. F., Stang P. D., 1986, The Astrophysical Journal, 302, 459

Leventhal M., MacCallum C. J., Stang P. D., 1978, The Astrophysical Journal Letters, 225, L11

Lewin W. H. G., van Paradijs J., van den Heuvel E. P. J., 1997, *X-ray Binaries*

Liang E., Narayan R., 1997, in Dermer C. D., Strickman M. S., Kurfess J. D. (eds.), *Proceedings of the Fourth Compton Symposium*, vol. 410 of *American Institute of Physics Conference Series*, pp. 461–476

Liang E. P. T., Price R. H., 1977, Astrophys. J., 218, 247

Ling J. C., Wheaton W. A., 1989, The Astrophysical Journal Letters, 343, L57

Longair M. S., 1994, *High energy astrophysics. Vol.2: Stars, the galaxy and the interstellar medium*, Cambridge: Cambridge University Press, —c1994, 2nd ed.

Mahoney W. A., Ling J. C., Wheaton W. A., 1994, Astrophysical Journal Supplement Series, 92, 387

Malzac J., Belloni T., Spruit H. C., Kanbach G., 2003, Astronomy and Astrophysics, 407, 335

Malzac J., Belmont R., Fabian A. C., 2009, ArXiv e-prints

Malzac J., Merloni A., Fabian A. C., 2004, Mon. Not. R. Astron. Soc., 351, 253

Markoff S., Falcke H., Fender R., 2001, Astronomy and Astrophysics, 372, L25

Markoff S., Nowak M., Corbel S., Fender R., Falcke H., 2003, Astronomy and Astrophysics,

397, 645

Marscher A. P., 1980, The Astrophysical Journal, 235, 386

McClintock J. E., Remillard R. A., 2006, *Black hole binaries*, pp. 157–213

McHardy I. M., Koerding E., Knigge C., Uttley P., Fender R. P., 2006, Nature, 444, 730

McKinney J. C., Blandford R. D., 2009, Mon. Not. R. Astron. Soc., 394, L126

Merloni A., Heinz S., di Matteo T., 2003, Mon. Not. R. Astron. Soc., 345, 1057

Migliari S., Tomsick J. A., Markoff S., Kalemci E., Bailyn C. D., Buxton M., Corbel S., Fender R. P., Kaaret P., 2007, The Astrophysical Journal, 670, 610

Mirabel I. F., Dhawan V., Chaty S., Rodriguez L. F., Marti J., Robinson C. R., Swank J., Geballe T., 1998, Astronomy and Astrophysics, 330, L9

Mirabel I. F., Rodríguez L. F., 1994, Nature, 371, 46

Ohsuga K., Mineshige S., Mori M., Kato Y., 2009, Publ. Astron. Soc. Jpn., 61, L7+

Paciesas W. S., Tueller J., Cline T. L., Teegarden B. J., Durouchoux P., Hameury J. M., 1982, The Astrophysical Journal Letters, 260, L7

Panaitescu A., Mészáros P., 1999, The Astrophysical Journal, 526, 707

Pe'er A., Casella P., 2009, ArXiv e-prints 0902.2892

Pooley G. G., Fender R. P., 1997, Mon. Not. R. Astron. Soc., 292, 925

Press W. H., 2002, *Numerical recipes in C++ : the art of scientific computing*

Purcell W. R., Cheng L.-X., Dixon D. D., Kinzer R. L., Kurfess J. D., Leventhal M., Saunders M. A., Skibo J. G., Smith D. M., Tueller J., 1997, The Astrophysical Journal, 491, 725

Riegler G. R., Ling J. C., Mahoney W. A., Wheaton W. A., Willett J. B., Jacobson A. S., Prince T. A., 1981, The Astrophysical Journal Letters, 248, L13

Rodriguez L. F., Gerard E., Mirabel I. F., Gomez Y., Velazquez A., 1995, Astrophysical Journal Supplement Series, 101, 173

Rogers K. S., 2008, *A Numerical Study in Spectra and Variability of X-ray Binaries and AGN*, Ph.D. thesis, School of Physics and Astronomy, Faculty of Engineering, University of Southampton

Rybicki G. B., Lightman A. P., 1979, *Radiative Processes in Astrophysics*, Wiley-Interscience

Shakura N. I., Sunyaev R. A., 1973, Astronomy and Astrophysics, 24, 337

Share G. H., Kinzer R. L., Kurfess J. D., Messina D. C., Purcell W. R., Chupp E. L., Forrest D. J., Reppin C., 1988, The Astrophysical Journal, 326, 717

Spada M., Ghisellini G., Lazzati D., Celotti A., 2001, Mon. Not. R. Astron. Soc., 325, 1559

Spruit H. C., Kanbach G., 2002, Astronomy and Astrophysics, 391, 225

Svensson R., 1982, The Astrophysical Journal, 258, 335

Teegarden B. J., Cline T. L., Gehrels N., Palmer D., Ramaty R., Seifert H., Hurley K. H., Landis D. A., Madden N. W., Malone D., Pehl R., Owens A., 1996, Astrophys. J. Lett., 463, L75+

Teegarden B. J., Watanabe K., 2006, The Astrophysical Journal, 646, 965

Timmer J., Koenig M., 1995, Astronomy and Astrophysics, 300, 707

Uttley P., 2009, private communication

Weidenspointner G., Skinner G., Jean P., Knödlseder J., von Ballmoos P., Bignami G., Diehl R., Strong A. W., Cordier B., Schanne S., Winkler C., 2008, Nature, 451, 159

Wilkinson T., Uttley P., 2009, Mon. Not. R. Astron. Soc., 397, 666

Zdziarski A. A., 1984, The Astrophysical Journal, 283, 842

Zdziarski A. A., Coppi P. S., Lamb D. Q., 1990, The Astrophysical Journal, 357, 149

Zdziarski A. A., Gierliński M., Rao A. R., Vadawale S. V., Mikołajewska J., 2005, Mon. Not. R. Astron. Soc., 360, 825